AGH UNIVERSITY OF SCIENCE AND TECHNOLOGY

FIELD OF SCIENCE: NATURAL SCIENCE

SCIENTIFIC DISCIPLINE: PHYSICAL SCIENCE

DOCTORAL THESIS

Biomolecular and elemental micro-analysis of the skeletal muscle in the quest of new tissue markers of neuromuscular diseases.

Author: Paula Kasprzyk

First supervisor: prof. dr hab. inż. Marek Lankosz

Assisting supervisor: prof. dr hab. med. Dariusz Adamek

Completed in: AGH-University of Science and Technology, Faculty of Physics and Applied Computer Sciences, Department of Medical Physics and Biophysics
Jagiellonian University Medical College in Krakow, Department of Neuropathology

Krakow, February 2023

Declaration of the author of this dissertation:
Aware of legal responsibility for making untrue statements I hereby declare that I have written this dissertation myself and all the contents of the dissertation have been obtained by legal means.

…….
(date, signature)

Declaration of the thesis Supervisor:
This dissertation is ready to be reviewed.

…….
(date, signature)

Declaration of the thesis Supervisor:
This dissertation is ready to be reviewed.

…….
(date, signature)

We acknowledge Diamond Light Source for time on Beamline I18 under proposal SP20436 and for time on Beamline B22 under proposal SM2037.

We acknowledge DESY (Hamburg, Germany), a member of the Helmholtz Association HGF, for the provision of experimental facilities. Parts of this research were carried out at PETRA III and we would like to thank Matthias Alfeld for assistance in using P06 beamline. Beamtime was allocated for proposal I-20180090EC.

This PhD thesis has been completed in the framework of the Program POWER, project No. POWR.03.02.00-00-I004/16, co-financed by the European Union.

I would like to express my sincere thanks:

to the supervisors: prof. dr hab. inż. Marek Lankosz and prof. dr hab. med. Dariusz Adamek for their scientific supervision, time and assistance with the realisation of the dissertation.

to the Biomedical and Environmental Research Group for their kind support during my PhD studies.

to dr inż. Joanna Dudała for her help during the research phase and for her substantive assistance.

to dr hab. inż. Magdalena Szczerbowska-Boruchowska for her kindness, patience and substantial assistance in writing the thesis.

My greatest thanks go to dr inż. Paweł Wróbel for his invaluable assistance during the research, valuable advice during the writing of the thesis and for motivating me to continue my scientific work.

Thanks to the family for their support and consideration.

Abstract

Muscle diseases, in which the dysfunction in the tissue is due to pathology in the muscle cell itself rather than damage of the nervous system, are collectively known as myopathies. Thus, the most general statement is that myopathy is a condition involving muscle tissue with different etiopathogenesis, different distribution scheme of muscle disfunction and diverse clinical course, and the consequences for the affected person. As muscle tissue also undergoes age-related processes - 'sarcopenia' - this tissue can also become an indicator of health status. It is therefore not out of the question that a biopsy of muscle, a tissue that is relatively easy to access, may have broad indications. Consequently, it is advisable to gain much more knowledge about the observable even tiniest elemental and biomolecular changes in muscle tissue. One of the aims of this thesis was to provide a basis for such input.

In order to study the differences resulting from the elemental composition of muscle fibres, the synchrotron radiation X-ray fluorescence (SR-XRF) technique was used, which is a type of qualitative and quantitative method for imaging the spatial distributions of elements in biological samples. It is a multi-element analysis method, the great advantage of which is the possibility of determining not only the elements necessary for muscle function, but also those whose importance is less well known and whose content in muscle fibres is lower. Fourier transform infrared spectroscopy (FTIR) was used to investigate the differences resulting from the biomolecular composition of muscle fibres. This is a method that allows one to visualise the distribution of biomolecules in muscle tissue, as well as to characterise and compare their content in individual samples. Since elemental as well as biomolecular changes can reflect biochemical processes in muscle fibres, studying them at different stages can lead to an understanding of disease development at an early stage.

The obtained results showed that there is a difference in both the elemental and biomolecular compositions between the tissue defined as the reference group and the tissues diagnosed as having changes through pathological processes - the group of dystrophies and myopathies. The greatest differences for fibers can be observed for

elements such as: P, K, Ca and Cr, however, for all analyzed elements, a decrease in their content can be seen for the dystrophy group. For measurements of the biomolecular composition using FTIR, it can be seen that the value of net area under the analyzed peak was highest for the dystrophy group compared to the other two groups. A higher protein content can be observed in hypertrophic fibres, while atrophic fibres show a conversion of muscle tissue into fat tissue.

Streszczenie

Choroby mięśni, w których dysfunkcja w tkance wynika z patologii samej komórki mięśniowej, nie zaś uszkodzenia układu nerwowego, zbiorczo nazywane są miopatiami. Najogólniej można więc stwierdzić, że miopatia to schorzenie dotyczące tkanki mięśniowej o różnej etiopatogenezie, różnym schemacie dystrybucji dysfunkcji mięśniowej i zróżnicowanym przebiegu klinicznym oraz konsekwencjach dla osoby dotkniętej chorobą. Ze względu na fakt, że tkanka mięśniowa również ulega procesom związanym z wiekiem - "sarkopenia", tkanka ta może również stać się wskaźnikiem stanu zdrowia. Nie wykluczone więc, że biopsja mięśni, tkanki stosunkowo łatwo dostępnej, może mieć szerokie wskazania. W związku z tym wskazane jest zdobycie znacznie większej wiedzy na temat obserwowalnych nawet najdrobniejszych zmian pierwiastkowych i biomolekularnych w tkance mięśniowej. Jednym z najbardziej pożądanych celów prezentowanej pracy dyplomowej jest wniesienie wkładu w taki wgląd.

W celu zbadania różnic wynikających ze składu pierwiastkowego włókien mięśniowych zastosowano technikę fluorescencji rentgenowskiej promieniowania synchrotronowego (SR-XRF), która jest rodzajem jakościowej i ilościowej metody obrazowania rozkładów przestrzennych pierwiastków w próbkach biologicznych. Jest to metoda analizy wieloelementowej, której wielką zaletą jest możliwość określenia nie tylko pierwiastków niezbędnych do funkcjonowania mięśnia, ale także tych, których znaczenie jest mniej znane, a ich zawartość we włóknach mięśniowych mniejsza. Do zbadania różnic wynikających ze składu biomolekularnego włókien mięśniowych wykorzystano spektroskopię w podczerwieni z transformacją Fouriera (FTIR). Jest to metoda, która pozwala zobrazować rozkład biomolekuł w tkance mięśniowej, jak również scharakteryzować i porównać ich zawartości w poszczególnych próbkach. Ponieważ zmiany pierwiastkowe jak i biomolekularne mogą odzwierciedlać procesy biochemiczne zachodzące we włóknach mięśniowych, badanie ich na różnych etapach może prowadzić do zrozumienia rozwoju choroby na jej wczesnym etapie.

Uzyskane rezultaty pokazały, że istnieje różnica zarówno w składzie pierwiastkowym jak i biomolekularnych pomiędzy tkanką zdefiniowaną jako grupa referencyjna, a tkankami zdiagnozowanymi jako posiadające zmiany poprzez procesy patologiczne - grupę dystrofii oraz miopatii. Największe różnice dla włókien można zaobserwować dla pierwiastków takich jak: P, K, Ca oraz Cr, jednak dla wszystkich analizowanych pierwiastków można zauważyć zmniejszenie ich zawartości dla grupy dystrofii. Pierwiastkowy skład endomysium - tkanki łącznej pomiędzy włóknami, dla próbek pochodzących z grup objętych zmianami patologicznymi. W przypadku pomiarów składu biomolekularnego z wykorzystaniem FTIR można zauważyć, że wartość pola powierzchni netto pod analizowanym pikiem była najwyższa dla grupy dystroficznej w porównaniu z pozostałymi dwoma grupami. We włóknach hipertroficznych można zaobserwować wyższą zawartość białka, natomiast we włóknach atroficznych widać zamianę tkanki mięśniowej w tkankę tłuszczową.

Contents

1. Introduction

Muscle diseases are often collectively described as 'myopathies', which refers to the fact that the dysfunction occurring in the tissue is due to pathology in the muscle cells rather than damage to the nervous system. Thus, the most general statement is that myopathy is a condition involving muscle tissue with different etiopathogenesis, different distribution scheme of muscle disfunction and diverse clinical course, and the consequences for the affected person. As a result, in its simplest intuitive grasp, "myopathy" denotes any condition or disorder that involves muscle tissue. The most general classification is based on the etiological criterion covering primary and secondary muscle diseases. Primary diseases include a whole range of genetic disorders collectively known as dystrophies, or various and special forms of inherited myopathies while secondary myopathies can be specifically distinguished by tissue damage of toxic, metabolic, immunological or endocrine origin, or else their cause lies in malfunction of the nervous system [1][2][3].

The symptoms of "myopathies", even "primary" ones, whether it be inherited or acquired, are frequently not limited to the muscles. For example, in myotonic dystrophias one observes different disturbances affecting heart, eyes (cataracts), endocrine system, in some inflammatory myopathies (also called "myositides"), especially dermatomyositis (DM) not only skin is involved (though supposedly not always) but there might be sometimes severe pulmonary changes (so called "interstitial lung disease"), critical for the life perspectives of the patient. Another group of myopathies – named "mitochondrial myopathies" – typically involves also tissue of the central nervous system, hence the term "encephalomyopathies". Still another "inflammatory" myopathy – the "Inclusion body myositis" (IBM) conspicuously shares many molecular derangements (pathological deposits of different proteins) with degenerative brain diseases like Alzheimer disease, and in fact counting this disease to "idiopathic inflammatory myopathies" is a disputable issue since "inflammation" is rather a sort of epiphenomenon whereas it is a kind of (myo)degeneration of muscle tissue that underlies muscle destruction and malfunction in this condition. We are gradually more and more aware that with the

advanced age not only brain is subjected to ineluctable degeneration especially epitomized by Alzheimer-type pathology, but also muscle tissue succumbs to age-related processes which are covered by the general term of “sarcopenia”. This condition very probably of multicausative nature of which up to now is little known supposedly contributes enormously to the age-related decline of health. Could someday the muscle tissue become a reliable indicator of the health status, and/or a crucial element in prognosis in various diseases related to different organs or even in cancers? One cannot exclude such possibility and consequently muscle biopsy i.e. the biopsy of a tissue relatively easy accessed, could have extremely broad indications. Of course, there is one and quite obvious condition. We have to gain much more knowledge into observable even tiniest biomolecular changes in muscle tissue. One of the most desirable aims of presented thesis is to make a contribution to such insight.

Most common feature of myopathy is weakness and decline of muscle tissue. Though obviously the main role of skeletal muscles is to exert mechanical force, they participate on whole body physiological as well as pathological processes and occupying roughly 1/3 of whole body mass [4] their impact on health status must be enormous not only by movement disturbances (if they occur), but contributing to malfunction of the whole organism causing or reflecting pathological conditions. Due to the excessive variety of diseases that fall under the term "myopathy," it seems important to know at least the minimal differences arising from their simplest divisions, such as the division into primary and secondary myopathies. Due to the lack of specificity in the differentiation of tissue affected by pathological change, from healthy tissue - the most typical symptom is muscle atrophy, which on microscopic imaging can be observed as a change in fibre diameter. Structural changes observed in muscle diseases may be derivatives of biomolecular changes as well as changes in the elemental composition of individual fibres. Exploring these differences can lead to an understanding of disease development at its early stages.

In order to study the differences resulting from the elemental composition of muscle fibres affected by the disease and apparently healthy fibres - which do not show pathological changes in the pathomorphological diagnosis, the synchrotron

radiation X-ray fluorescence (SR-XRF) technique was used, which is a type of a qualitative and quantitative method of imaging spatial distributions of elements in biological samples [5][6]. This is a well-known method of multi-elemental analysis, whose great advantage, besides the ability to image tissues due to the elements present in them and their distribution, is the possibility of determining not only the elements that are essential for the functioning of the muscle, but also those whose importance is less known and their content in muscle fibres is lower.

Fourier-transform infrared spectroscopy (FTIR) was used to examine differences arising from the biomolecular composition of muscle fibres diagnosed as diseased tissue and those assigned to the reference group. This is a method that has been used to measure both biological tissues [7][8] and muscle tissue of animal [9][10][11][12] or human origin itself [13].

Thus, there is a need for research on possibly occurring differences in both biomolecular and elemental composition directly on material of human origin. Since these changes may reflect biochemical processes that occur in muscle fibres, studying them at different stages may lead to an understanding of disease development at its early stages.

2. Motivation

The aim of this study was to investigate the chemical and biomolecular changes occurring in the muscle tissue affected by the pathological process i.e. myopathy and dystrophy in comparison to reference tissue that do not show microscopic pathological features and can be considered as healthy. Myopathies is a group of diseases leading to their structural changes and decline of muscle fibres, what can be reflected in their elemental and biomolecular composition. influencing the biochemical processes in the fibre. Therefore, studying them may contribute to a better understanding of the disease and its development, especially at its initial stages. In particular, the research conducted in this work aimed at comparing the molecular and elemental composition occurring in tissue using, as it was earlier mentions, Fourier-Transform Infrared Spectroscopy (FTIR) and synchrotron radiation X-ray Fluorescence (SR-XRF). Using both techniques, efforts were made to understand the changes of distribution of elements and molecules in the muscle fibres both in tissue affected by disease and the reference one. The difference in the elemental composition of the connective tissue surrounding the fibres formally referred as endomysium was also investigated.

Due to the use of a destructive technique as SR-XRF, and the subsequent use of FTIR on the same samples, the effect of radiation damage was also analysed. For this purpose, measurements were carried out in the same areas of the samples in the following order: FTIR measurements, SR-XRF measurements, then once again by FTIR method. The analysed spectra before and after possibly resulting damage will be presented later in the work.

3. Biological background

Skeletal muscles forming a substantial compartment of so called soft tissues of the body are one of the most metabolically dynamic tissues in the human body. This tissue accounts for approximately 40% of the total body weight and contains between 50 to 75% of all proteins in the body. Skeletal muscles are a system that allows free movement, as they are innervated somatically and under the conscious control of the nervous system except for the heart muscle which is innervated autonomically. They form the body's musculature, occurring not only in extremities but also in soft parts of head including mouths cavity, orbits or larynx [14][15].

3.1. Structure of skeletal muscle

Cross-striated muscle tissue consists of long, cylindrical cells that can be up to several tens of centimetres in length and vary in diameter from 10 to even 100 μm. These cells are specialised in changing their length and tension. A muscle cell, also known as a muscle fibre, is multinucleated - Figure 1. It has about 70 nuclei per 1mm of length, which are located in the peripheral part of the cytoplasm of the muscle cell (so called sarcoplasm) i.e. under sarcolemma which marks the other border of the cell. The main component of the cytoplasm are myofibrils consisting of protein chains that have the ability to move relative to each other what's results in decreasing the longitudinal dimension of the cell (contraction) or increasing, known as relaxation. Microfibrils have diameters of 1-2 nm and form bundles with a regular, parallel arrangement and are composed of specific proteins mostly myosin and actine whose interaction are responsible for exertion of force. The protein structure of myofibers not only allows for the complex spatial arrangement of the individual sarcomere components and the fibre as a whole in relation to each other, but also for the performance of essential functions in this highly specialised cell [1][14][16]. Individual muscle fibres, surrounded by the delicate connective tissue called endomysium which contains numerous capillaries, form fascicles surrounded by a structure called perimysium which is also a derivative of connective tissue. The entire skeletal muscle

is made up of parallel fascicles separated by connective tissue, within which run blood vessels and nerve bundles [16].

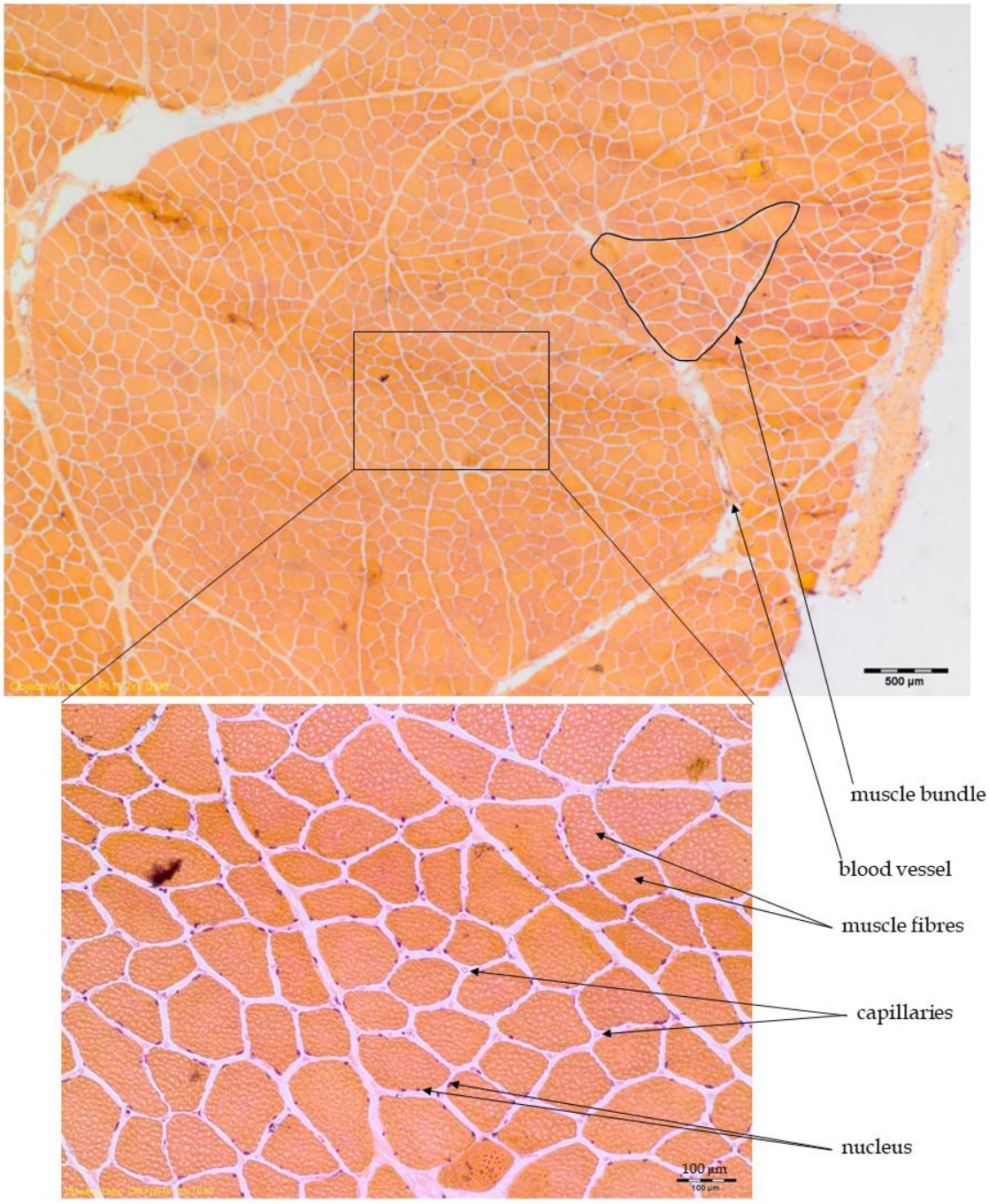

Figure 1. Optical microscope image of a sample of muscle tissue placed on a microscope slide and stained with haematoxylin and eosin (H&E) showing the structure of skeletal muscle with the most important structures highlighted.

The division of muscle fibres into types can be made according to functional, histochemical and biochemical criteria. According to the functional criterion, skeletal muscle fibres can be divided into "slow twitch" – type 1 and "fast twitch" – type 2. They are differentiated by their contraction time - for fast ones it is shorter. Slow fibres are more resistant to fatigue. Considering the differences in histochemical reactions, it can be seen that some fibres stain weaker in reaction to myofibrillar ATP-ase at a pH of 9.4 (Figure 2) - these fibres are called type 1 fibres, those showing a strong reaction are type 2 fibres. The main differences reside in the metabolism of the different muscle types. Type 1 fibres contain a lot of mitochondria and primarily use energy generated by oxidative phosphorylation. This cell type is characterised by a high content of myoglobin, which gives the fibres their characteristic deep red colour. Type 2 fibres can be subdivided into type 2A and 2B fibres. Type 2A fibres benefit from both oxidative phosphorylation energy and glycolysis energy, while type 2B fibres benefit mainly from glycolysis energy in the cytoplasm. In haematoxylin staining there show weaker red colouration. The distinction between mentioned above muscle fibre types is important in pathological diagnosis of muscle diseases since in some conditions particular types may be selectively affected and also is crucial for the diagnosis of denervation changes of muscle.

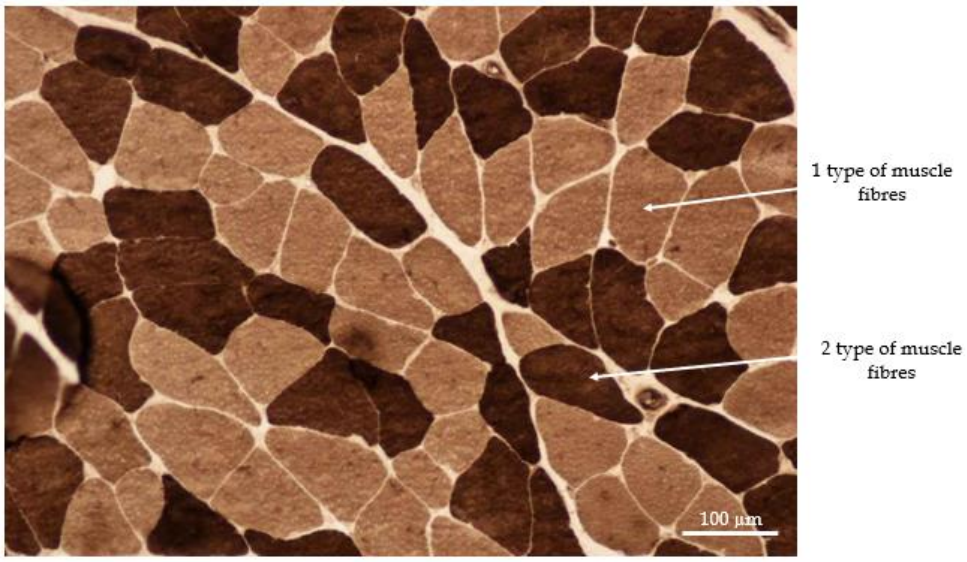

Figure 2. Optical microscope image of a sample of muscle tissue placed on a microscope slide and stained with 9.4 ATP-ase showing the differences in colouration between type 1 (lighter colouring) and type 2 fibres (darker colouring).

3.2. Skeletal muscle diseases

Due to the similar symptoms of all disorders that have different origins, the most general classification divides myopathies into primary and secondary diseases. Thus, primary myopathies include those conditions that have typically genetic background and their essential clinical symptoms and pathological changes are mainly due to involvement of muscle tissue by pathological processes. Secondary myopathies include pathological changes of toxic, endocrine, immunological, neurogenic atrophy, mitochondrial disease, diseases caused by pathology of neuromuscular junction or metabolic origin [17].

Out of many types of muscle diseases which generally can be referred to as "myopathies" special position occupy so called dystrophies, which are muscle diseases with genetic background and show progressive course, manifesting features of cell and tissues destruction.

Classification is sort of problematic with inflammatory myopathies where the muscle inflammatory process can be only a part of much broader, sometimes multisystem pathology concerning not only muscle but also other connective tissues derivatives what frequently lead to the use of term "connective tissues diseases".

The most typical pathological changes in muscles reflecting cellular and tissue destruction as well as response to the destructive process include:

- atrophy/hypertrophy of fibres,
- necrosis of myofibres,
- inclusions,
- regeneration of fibres (basophilia due to high RNA content),
- internalization of nuclei,
- fibrosis of endomysium, lipomatosis,
- inflammatory infiltrates,
- elevation of enzymes in serum (creatine kinase).

Myopathies therefore encompass several disease entities causing weakness of muscle and impairment of their structure. The morphological changes involve the cells having an increased number of nuclei that form chains and are transferred from subsarcolemmal region in to the deeper area of muscle fibre. There is fragmentation and 'dissolution' of myofilaments, resulting in a view of swelling and indistinct striations and so call "combing", which denotes separation of singular boundless of myofilaments. Some fibres may be hypertrophic. Except of so called denervation atrophy (typically "grouping atrophy") and atrophy seen in some particular myositides like dermatomyositis and anti-synthetase syndrome (so called perifasicular atrophy) typically atrophic muscle fibres are randomly distributed without a clear pattern. The beginning face of muscle fibre atrophy may be difficult to identify and discern where the objective assessment can be possible by microscopic measurement. Unequivocal features of atrophy can be seen only when the size of the cell (muscle fibres) is evidently small or adopts multangular shape (so called angulated fibres). The level of muscle fibre atrophy may be different when the end-stage is represented by clusters of "naked nuclei" almost devoid of sarcoplasm. As a result muscle tissue being replaced by fat and connective tissue - Figure 3. One has to be aware that inconsiderable part of muscle biopsies no evident token of pathologies is found. That doesn't mean that the muscle is truly healthy.

For the purpose of this study there was decided to investigate muscle biopsy material with regard to three categories: dystrophias, "myopathies" and biopsies which did not show signs of pathology (on the grounds of microscopic investigation using standard histological, histochemical and immunohistochemical methods). To this end it was used formal neuropathological diagnoses (pathological reports which obviously were anonymized).

To the group od "dystrophias" were included cases in which muscle dystrophy was explicitly stated in the histopathological diagnosis or at least diagnosis of dystrophy was suggested as a most probable option of differentiate diagnosis. Of note, in some types of dystrophias an inflammatory reaction may be also observed and this was not regarded as the reason to disqualify the case from "dystrophy group".

Group termed as "myopathies" was defined essentially by exclusion, i.e. it refers to biopsies which in histopathological examination showed any form of pathology except that they were not suggestive of dystrophy. In this category there were inflammatory myopathies and cases of unspecific changes.

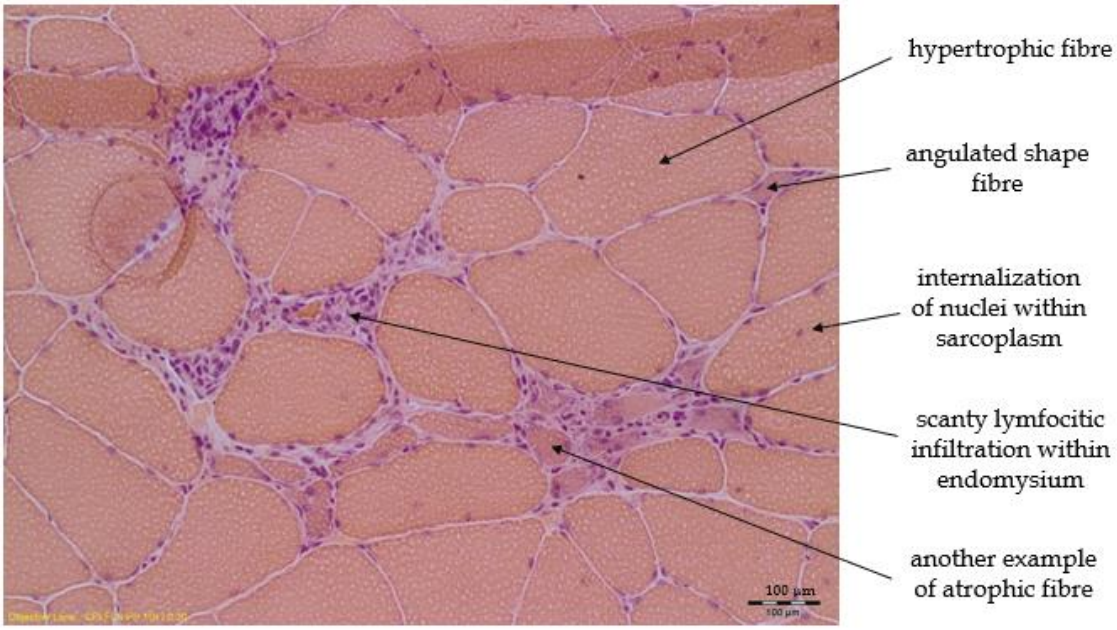

Figure 3. Optical microscope image of a sample of muscle tissue placed on a microscope slide and stained with haematoxylin and eosin (H&E) showing some of the typical pathological changes occurring in muscle tissue.

The biopsies which did not show any pathology in histopathological examination were qualified to "reference group". Of course one has to be aware that such "negative" diagnosis does not exclude the disease of muscle, though even if, the patient suffers from muscle disease it is justifiable to think that his or her ailment has mild or at most moderate severity. Moreover, one has to bear in mind, that the distribution of pathological changes even in best characterized genetic disorders may be different (what is frequently addressed by the term "heterogeneity") what means that the biopsy material may not be truly representative. Therefore it indicates another rationale for the biomolecular investigations of muscle tissue which (hopefully) may show discrete pathological changes of muscles which might go undetected in routine histopathology even with use of many histo-techniques.

In general, it seems reasonable to envision "dystrophias" or "dystrophic pathology" (since ultimate diagnosis of particular type of muscular dystrophy in many cases requires definite genetic confirmation) as representing more prolong destructive and essentially irreversible process affecting muscle, in contrary to cases collectively grouped as "myopathies" which most probably represent more dynamic and in many cases reversible forms of muscle pathology (of course not all since some of them like Inclusion-Body Myositis represent rather progressive and almost unmodifiable by treatment process).

In elucidation of pathological processes in the muscle one has to remember that the muscle tissue makes an important, but a part of the body and with complicated relationship between its other components. It is very difficult, if at all possible to tell what is truly an essential process of muscle or only a reflection of something that primary happened in whole body.

4. Physical background of methods

4.1. X-ray Fluorescence Spectroscopy (XRF)

4.1.1. Interaction of X-rays with matter

The interaction of photons with matter can be classified according to the type of target - electrons, atoms or nuclei with which the photon interacts; or the type of event that takes place - absorption, scattering or pair creation. The probability of any kind of interaction (collision) can be described by the probability of removal of photon from the narrow, monochromatic and parallel beam that passes through the homogenous layer of the absorber with the given atom density $\rho\frac{N_A}{A}$ ($1/\mathrm{cm}^3$) and thickness t (cm):

$$p = \frac{I}{I_0} = e^{-\sigma_{tot}\rho\frac{N_A}{A}t} \quad (1)$$

Where: σ_{tot} – collision cross section per atom (cm^2), ρ – absorber density ($\mathrm{g/cm}^3$), N_A – Avogadro number, A – atomic mass, I and I_0 – transmitted and incident photon fluxes, respectively. Since the interaction of photons with nuclei or their electric field occurs only for very high energies (above 1 MeV) which is far beyond the range of interest of XRF the σ_{tot} can be expressed as a sum of collision cross sections of three main processes:

$$\sigma_{tot} = \tau + \sigma_R + \sigma_C \quad (2)$$

where: τ – total photoelectric absorption cross section per atom, σ_R , σ_C – Rayleight and Compton collision per section [18].

Incoherent scattering or Compton effect, is a collision between a photon and an almost free electron (with negligible binding energy). According to the principle of conservation of momentum and energy, as a result of this collision, part of the photon's energy is given up to the electron, which thus gains some kinetic energy - the recoil energy - while the photon loses this energy by changing its direction. The energy hv of the scattered photon can be calculated using the formula:

$$hv = \frac{hv_0}{1+\frac{hv_0}{m_0c^2}(1-cos\varphi)} \quad (3)$$

where: hv_0 - primary energy of the photon, m_0 - rest mass of the electron and c - speed of light in a vacuum.

The probability of incoherent scattering is proportional to the number of electrons in atom thus the scattering cross section is proportional to the atomic number Z. The probability of Compton scattering on a single free electron depends either on photon energy or the scattering angle and is described by Klein-Nishina formula for differential cross section [19]. The detailed description of the phenomenon requires to account for the binding of the electrons in atoms by applying so called incoherent scattering functions [18]. The effect is also sensitive for the photon polarisation.

The coherent or Rayleigh scattering takes place when photon is scattered by the electrons that are bonded in the atoms. In this case, the photon scatters without any change of its energy. The phenomenon can be described on the basis of the theory of classical electromagnetism. The free electron exposed on the oscillating electric field of the primary photon oscillates and thus becomes a source of the secondary radiation. The probability of the scattering on a single free electron is described by the Thomson formula for the differential cross section. The full description of the Rayleigh scattering cross section per atom requires the introduction of so-called atomic form factor (proportional to Z^2) that takes into account the fact that there are many electrons in the atom and that those electrons are bonded [18].

Photoelectric absorption is the transfer of the energy of a photon hv_0 to an electron bound on the inner shell of an atom. As a result, the photon disappears, while an electron - a photoelectron - is ejected from the atom, with a kinetic energy defined by the equation:

$$E_k = hv_0 - E_w \quad (4)$$

where: E_w is electron binding energy at a certain level in the atom - photoelectric absorption boundary.

The probability of such a phenomenon occurring is expressed by the cross section per atom and is given by the formula (valid between the absorption edges):

$$\tau_a = \tau_0 \frac{Z^5}{(h\nu_0)^3} \quad (5)$$

where: τ_0 - proportion coefficient.

This phenomenon occurs with high probability in heavy atoms for photons of low energies [18][20].

4.1.2. Deexcitation of atoms

When the electron is removed from the atomic shell (by photoelectric effect or by collision with ionised particle) the atom is ionised and its total energy is increased. The electron vacancy is filled by the transition of electron from higher atomic shell. The excess energy accompanied with the electron transition between the shells can be removed in a radiative or radiationless manner. In the first process each transition is accompanied with the emission of photon of the characteristic radiation with energy equal to the difference of the electron binding energies between shells. According to the Moseley law the wavelength λ of the photon of given emission line is attributed to the given element:

$$\frac{1}{\lambda} \approx (Z - \sigma)^2 \quad (6)$$

Where σ is a screening constant correcting the repulsion force of other electrons in the atom. In the second process the excess energy is removed by ejection of electron (Auger effect). The probability of this process increases with decreasing of the atomic number making the analysis of light elements by XRF difficult.

4.1.3. Intensity of the characteristic X-rays

The intensity of the characteristic radiation emerging from the sample irradiated by X-rays depends on multiple factors like the amount of element, measurement geometry and detector as well as the intensity of primary radiation. Furthermore, the proper analytical description of the phenomenon has to take into

account the absorption of the primary and secondary radiation inside the irradiated material. When the excitation beam of radiation is monochromatic, the intensity of the characteristic radiation line of energy E_i can be determined by the equation [18]:

$$I_i(E_i) = \frac{G\varepsilon(E_i)a_i(E_0)I_0(E_0)}{\sin(\alpha)} \cdot \frac{1-\exp[-\rho d(\mu(E_0)\csc(\alpha)+\mu(E_i)\csc(\beta)]}{\mu(E_0)\csc(\alpha)+\mu(E_i)\csc(\beta)} \quad (7)$$

$$a_i = W_i\tau_i(E_0)\omega_i p_i(1-\frac{1}{j_i}) \quad (8)$$

where: $I_i(E_i)$ is the intensity of the fluorescence radiation of i-th element, G – the geometry factor, $\varepsilon(E_i)$ – the intrinsic detector efficiency, $I_0(E_0)$ – the number of incidence photons of energy E_0 per second, α – the incidence angle, β the take-off angels, ρ – the density of the sample in g/cm^3, d – the sample thickness in cm, $\mu(E_0)$ and $\mu(E_i)$ – the total mass attenuation coefficients in cm^2/g at energies E_0 and E_i, W_i – the weight fraction of i-th element, $\tau_i(E_0)$ – the total photoelectric mass absorption coefficient for the i-th element at the energy E_0 in cm^2/g, ω_i – the fluorescence yield of the element i, p_i – the transition probability of the K-th line of the element i, j_i – the absorption jump at the K-edge of photoelectric absorption in i-th element.

Typically, the elemental composition of the investigated samples is complex. This is accounted for by expressing the mass attenuation coefficients μ as a weighted arithmetic mean of the respective mass attenuation coefficients μ_i, where the weights w_i represent the contribution of the individual elements in the sample:

$$\mu = \sum_{i=1}^{n} w_i\mu_i \quad (9)$$

From the point of view of the absorption effects the samples can be divided into three groups: thin, intermediate and thick samples. For the first group the thickness of the sample is small enough to neglect the absorption effects. Then the equation (7) can be written as:

$$I_i^{thick}(E_i) = \frac{G\varepsilon(E_i)a_i(E_0)I_0(E_0)\rho d}{\sin(\alpha)} \quad (10)$$

From the equation (10) shows that the characteristic radiation is linearly dependent on the element concentration [21][22]. This approximation can be used when the following condition for the mass per unit area ($M = \rho d$) is achieved:

$$M_{thin} \leq 0{,}1/(\mu(E_0)\csc(\alpha) + \mu(E_i)\csc(\beta) \quad (11)$$

For thick samples with large M the following simplification can be used:

$$\frac{1-\exp\left[-\rho d(\mu(E_0)\csc(\alpha)+\mu(E_i)\csc(\beta)\right]}{\mu(E_0)\csc(\alpha)+\mu(E_i)\csc(\beta)} \approx \frac{1}{\mu(E_0)\csc(\alpha)+\mu(E_i)\csc(\beta)} \quad (12)$$

This simplification can be used when the following condition is fulfilled:

$$M_{thick} \geq 4.61/(\mu(E_0)\csc(\alpha) + \mu(E_i)\csc(\beta) \quad (13)$$

The samples for which $M_{thin} \leq M \leq M_{thick}$ are called intermediate samples.

4.1.4. X-ray optics

In both quantitative and qualitative studies, X-ray analysis is a well-established method for investigating elemental composition. However, modern demands for the determination of trace elements with low weight content in samples as well as investigation of the very local information on elemental composition have resulted in the fact that the measurements can only be carried out with high spatial resolution - focusing the incident beam and increasing its intensity, which determines the sensitivity and time of the analysis. To achieve the requirements of a monochromatic and focused beam, suitable optical elements must be placed between the radiation source and the sample.

Under the name of X-ray optics, there is a wide range of elements using the phenomena of refraction and diffraction, on artificial structures and natural crystals, and the phenomena of total external reflection. All these elements are designed to focus a beam, monochromatize it or reflect it [23].

Total External Reflection

The most important phenomenon used for focusing of X-rays is the total reflection. When the beam of X-rays impinges the polished surface at certain angle two processes occurs: reflection and refraction (followed by Snell law). Since the refractive index for X-rays is very close to unity those processes are very inefficient. However, due to the fact that the refractive index is smaller than unity when the impinging angle is smaller than the critical angle θ_C the total reflection occurs. The critical angle depends on the energy of the reflected radiation and the properties of the reflector and can be approximated as:

$$\theta_C \approx \frac{1}{E}\sqrt{\frac{Z}{A}\rho} \qquad (14)$$

Where: E – energy of X-rays, Z, A, ρ – atomic number, atomic mass and density of the reflector, respectively. Typically the critical angles are below 0.5^o.

In practice this phenomenon is used for shaping and focusing of the X-ray beam with use of mirrors of different curvatures. The most common focusing devices based on total reflection are Kirkpatrick-Baez mirrors, consisting of two elliptically curved mirror surfaces placed perpendicular to each other.

Diffraction

As an electromagnetic wave, X-rays undergo not only reflection but also diffraction. Crystals or multilayer structures are commonly used optical components. Radiation that incident at a certain angle on these elements can diffract according to Bragg's law:

$$n\lambda = 2dsin\theta \qquad (15)$$

Where: n – diffraction order, λ – wavelength, d – diffracting planes spacing, θ – incident angle. Since the reflected wavelength depends on the angle the monochromatization of polychromatic X-ray beam and capability of tuning of the X-ray beam energy is achievable.

4.1.5. Considerations on sample thickness in XRF

The use of biological samples in spectroscopic studies is associated with the possibility of distorted results caused by the sample itself and its possible preparation, not by apparatus errors. The main problem arising during the examination of the thin tissue slices is homogeneity of sample slices in terms of their density and thickness. Also, the preparation of the sample can affect its structural change. Furthermore, from a measurement perspective, it also seems important to determine whether the sample is thin, intermediate thickness or thick with respect to the elements analysed. For biological samples, the most important elements are the organic chemistry elements, i.e., H, C, N and O. All these elements can have a significant effect on the intensity of the characteristic radiation of the measured elements through the absorption of primary and secondary X-rays.

In order to check the relationship between the intensity of the characteristic radiation and the thickness of the sample, the relative intensity was calculated using equation (5):

$$R_i = \frac{I_i}{I_i^{thick}} = \frac{1-\exp\left[-\rho d(\mu(E_0)\csc(\alpha)+\mu(E_i)\csc(\beta)\right]}{\rho d[\mu(E_0)\csc(\alpha)+\mu(E_i)]} \quad (16)$$

Using the equation (16) and (9), as well as the theoretical composition of muscle tissue (information taken from [21]) the relative intensity was calculated for the measured samples at beam energies of 16.5 keV - experiment carried out on the Deutsches Elektronen-Synchrotron DESY synchrotron and 13.95 keV - experiment carried out on the DIAMOND Light Source synchrotron. The results of the calculations carried out are shown in Figure 4. According to the results obtained for all analysed elements in the DIAMOND synchrotron experiment, the sample could be considered thin, while for the DESY synchrotron experiment, the sample only became thin for elements with an atomic number above or equal to 26. The results obtained may have been particularly influenced by the unusual measurement geometry in the second experiment.

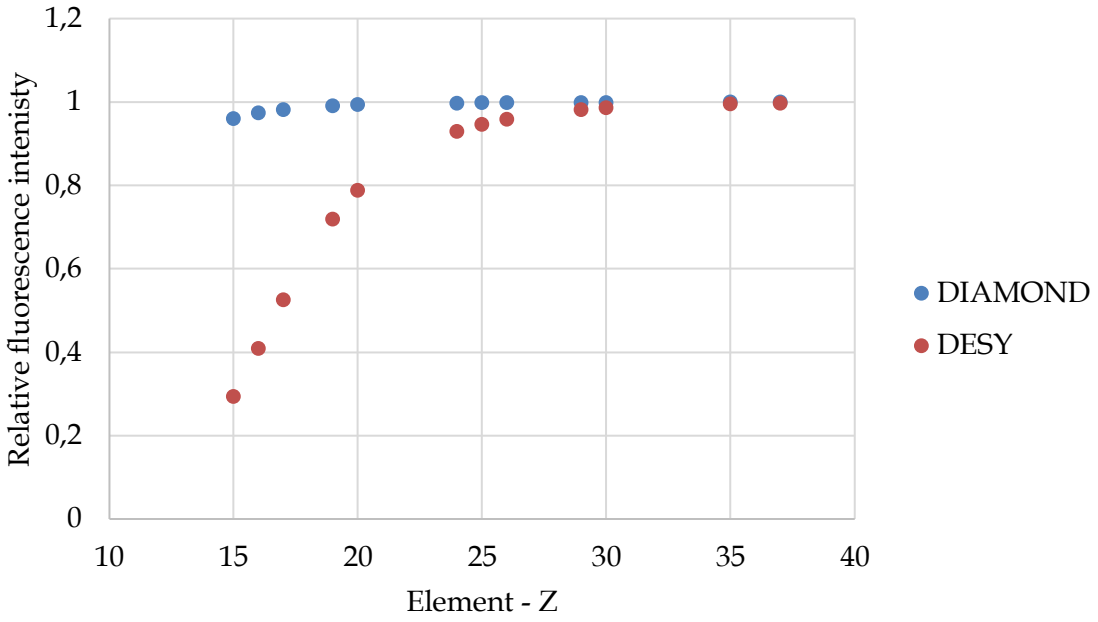

Figure 4. Graph showing the relative intensity of characteristic radiation for selected elements analysed.

4.2. Fourier-transform infrared spectroscopy (FTIR)

The Fourier transform infrared microspectroscopy technique was developed by combining two techniques - optical microscopy and infrared spectroscopy. Nowadays, this method allows to obtain micrometre spatial resolution, which permits to collect biochemical information from micro-areas of the studied sample. In the spectra obtained using it, characteristic absorption bands can be distinguished, originating from the active infrared vibrations of chemical bonds present in tissues of macromolecules such as lipids, proteins or nucleic acids.

4.2.1. Interaction of infrared radiation with the matter

Infrared spectroscopy is a technique that bases on the vibrations of the molecules of atoms. Obtaining a spectrum is possible by passing the radiation through a sample and determining which portion of that radiation has been absorbed. The energy for which a peak is observed represents the frequency of vibration of the molecule in the sample. Quantitatively, this phenomenon is described by the Bouger-Lambert-Beer law, according to which the absorbance A of a given material medium (sample) is proportional to the absorption coefficient (ε), molar concentration of the sample (C_{mol}) and its thickness (l).

$$A = \varepsilon \cdot C_{mol} \cdot l \tag{17}$$

The absorbance can be determined by recording the intensity of infrared radiation coming out of the absorbing medium - the sample (I), comparing it with the intensity of radiation incident on the sample (I_0). The ratio I / I_0 is called the transmittance T. Accordingly, the absorbance can also be determined as the decimal logarithm of the inverse of the transmittance.

$$A = \log_{10}\left(\frac{I_0}{I}\right) = \log_{10}\left(\frac{1}{T}\right) \tag{18}$$

Infrared spectra are most often presented as the dependence of absorbance or transmittance as a function of wave number [24][25][26]

4.2.2. Normal modes of vibrations

The interaction of infrared radiation with matter can also be understood in categories of changes in molecular dipole moments, which are associated with motion: rotation, oscillation and translation. Molecules, which are atoms connected by bonds, are systems that have a certain energy. The description of this energy is complex because it considers the kinetic and potential energy of the molecule. The kinetic energy results from the translational and oscillatory motion and rotation of atoms, while the potential energy comes from the interaction of electrons and nuclei that build the molecule.

The degrees of freedom of a molecule are equal to the sum of the degrees of freedom of the atoms of that molecule. Each atom has three degrees of freedom, which correspond to Cartesian coordinates (x,y,z). These are used to describe the position of an atom relative to other atoms in the molecule.

A molecule that consists of N atoms have $3N$ degrees of freedom. For nonlinear molecules, rotation and translation are described by three degrees. The number of degrees of freedom of oscillation or normal oscillation for nonlinear molecules is $3n - 6$ (rotation and translation are described by three degrees of freedom), while in linear molecules it is $3n - 5$ (rotation is described by two degrees of freedom - the axis of rotation around which the molecule rotates aligns with the line on which the atoms of this molecule belong). The natural oscillations do not cause displacement of the molecule's centre of mass or rotation, and their number is equal to the number of degrees of freedom of the oscillations. These oscillations are also defined as normal oscillations, in which all atoms of the molecule oscillate with equal frequency and pass through the equilibrium state in equal phase.

This oscillation is divided into stretching (valence) during which there is a change in the length of bonds and bending (deformation) when a change in bond angles occurs. In the case of plane molecules, deformational oscillations can be further divided into those taking place taking place in the plane of the molecule (in-plane), which consist of pendulum (rocking) and scissor twitches, and oscillations outside the

plane of the molecule (out-of-plane), which include fanning and twisting vibrations. Depending on the symmetry of the excursions, the oscillations are divided into symmetric - in-phase compatible, and asymmetric - out-of-phase incompatible. [24][27][28].

4.2.3. Construction of a FTIR spectrometer

FTIR microspectroscopy is based on the idea of interference of infrared radiation between two beams to obtain spectral information in the form of a so-called interferogram. The basic structure of a spectrometer consists of a radiation source, an interferometer, a sample chamber and a detector.

4.2.3.1. Radiation Source

The infrared radiation used in FTIR spectroscopy should be characterized by stability, continuity and high intensity over the entire spectral range. In a laboratory setting, it is used IR spectrometers with a globar, which is a thin rod made of SiC, or Nernst rod source (ZrO_2 + Y_2O_3). In studies requiring high spectral and spatial resolution, synchrotron radiation is used as an IR source.

In this study, the main research tools were spectrometers using a globar source and a synchrotron IR source. A globar is a ceramic rod made of silicon carbide that emits a collimated beam of IR radiation. With its use, a spectral resolution of between 4-8 cm^{-1} can be achieved. Its glow temperature is between 1200-1400 ^{o}C and the emitted radiation is highly stable. The radiation also has a higher intensity in the range of higher wave numbers.

Synchrotron radiation is generated during the movement of charged particles along curved trajectories. In order to curve the tracks of motion, a magnetic field generated by curving magnets or insertion devices - wigglers and undulators - is used. The main features of synchrotron radiation include high collimation, high beam intensity, polarisation and the possibility of obtaining radiation over a wide range. The power of IR radiation obtained in a synchrotron is no higher than the radiation from

conventional sources. However, the smaller size of the source and the narrow angle of emission makes the brightness of synchrotron radiation much higher.

4.2.3.2. Interferometer

In Fourier transform spectrometers, the spectral information is obtained in the form of an interferogram, which presents the relationship of a signal to time. To receive a spectrum in the frequency domain, the interferogram is transformed using the Fourier transform. The advantage of using an interferometer is undoubtedly the short spectrum collection time, since all wavelengths are collected simultaneously, which also results in an improved signal-to-noise ratio (Felgett's advantage). Another example is the obtaining of a high-precision scale of wave numbers in the spectrum due to optical control of the moving mirror (Connes' advantage). The radiation path is not limited by any slits (Jacquinot's advantage), as well as the spectral resolution is easily to changed.

The most common interferometer used in Fourier spectrometers is the Michelson interferometer, the structure of which is shown in Figure 5. A polychromatic beam of infrared radiation is directed at a special semi-permeable mirror (beamsplitter), which splits it into two equally perpendicular beams. One of the beams is reflected by the beamsplitter and hits a stationary mirror, while the other passes through a light distribution plate and hits a monotonously moving mirror. The movement of the mirror changes the optical path of the beam. Both beams reflect off the mirrors and hit the beamsplitter again, where they interference. The beam shaped in this way is directed to the sample and from there to the detector. When the waves of the beam are in phase with each other, they are amplified, whereas when the phase of a wave changes, by changing its optical path, interference results in mutual extinction. Due to the presence of waves of different wavelengths in the beam, changing the optical path has the effect of making some waves phase-shifted. On this basis, after performing a Fourier transform, information about the intensity of a wave at a given frequency is obtained [29].

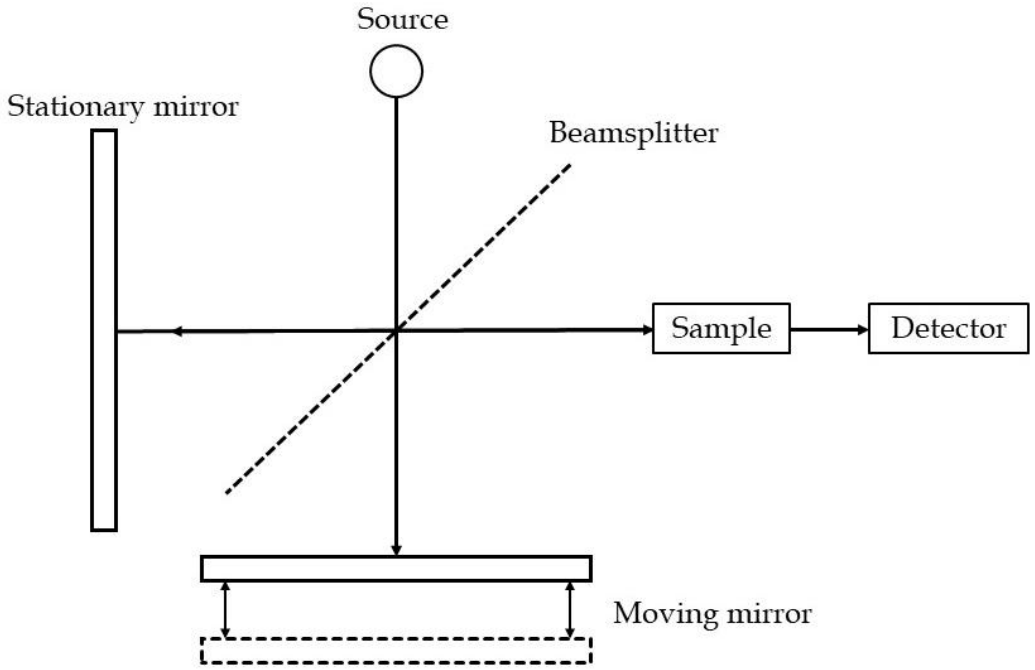

Figure 5. Michelson interferometer construction scheme. Based on [24][27].

4.2.3.3. Detector

After the radiation passes through the sample, the obtained signal is analysed by the detector. One of the detectors used in this method are detectors made of deuterated triglycine sulphate (DTGS). These detectors operate at room temperature and are used for routine measurements that do not require high sensitivity. Their advantage is their short response time.

Infrared microspectroscopy commonly uses detectors made of mercury-cadmium telluride called MCT detectors. Their advantage is the exceptionally good signal-to-noise ratio of the obtained spectra, while their disadvantage is the low operating temperature and the resulting necessity of cooling with liquid nitrogen.

4.2.4. Characteristic biomolecules and bands for animal tissues.

FTIR spectroscopy is used to analyse the frequencies of normal oscillation. On their basis, there are identified compounds in whose structure characteristic functional groups can be distinguished. In the normal oscillation participate all atomic cores of the molecule, which means that the oscillation of one atom affects the oscillation of the

other atoms of the molecule. The oscillations of characteristic functional groups are independent of the oscillations of individual atoms adjacent to them. A series of functional groups can be distinguished in the structure of organic compounds. The IR spectrum provides information on the biological macromolecules such as proteins, nucleic acids, lipids and carbohydrates present in a certain sample.

Proteins are polypeptides containing more than 100 amino acids that lead to the formation of polypeptide bonds. In the organism, they play a structural, transport, enzymatic, immunological or storage role. The structure of proteins can be divided into four levels. The primary level is the primary structure, which defines the sequence of amino acids that make up the protein chain. Its arrangement in space is determined by the secondary structure. The tertiary structure determines how the molecule is three-dimensionally folded. And the last structure, the quaternary structure, depends on the relative positioning of the oligomers - protein molecules with high mass. Of the bands analysed in the oscillatory spectrum, the band coming from amide I (1600-1690 cm^{-1}), which defines the secondary structure present in the protein chain, is the most significant [24][30][28].

Nucleic acids are biopolymers consisting of monophosphate nucleotides. Two types of nucleic acids can be distinguished, which are deoxyribonucleic acid (DNA) and ribonucleic acid (RNA), which act as carriers of genetic information. In the IR spectrum, the abortion bands characteristic of this group of molecules covers the wavenumber range 1080-1240 cm^{-1} [24][28][30].

Lipids are a group of hydrophobic compounds, most of which form the building blocks of biological membranes and adipose tissue cells. Their characteristic feature is the possession of a carbonyl group -COOH. They are most commonly found in the form of fatty acids, cholesterol, sphingolipids or phospholipids. In analytical studies, absorption bands in the range 2800-3050 cm^{-1}, which include both saturated and unsaturated bands, are used to detect changes in lipid content and their structures [24][28][30].

Carbohydrates are some of the most common compounds found in nature, which in the body function as a building material and as an energy substrate. The spectral range that covers carbohydrate detection is 900-1200 cm^{-1} wave numbers, which partly overlap with nucleic acids [24][28][30].

The Table 1 shows the characteristic absorption bands that can be observed in tissues of animal origin.

Table 1. Characteristic absorption bands observed in animal tissues. Based on [24][28][30].

Wavelenght (cm^{-1})	**Assignment**	
~3290	Proteins – Amide A	N-H stretching
~3060	Proteins – Amide B	N-H stretching
~2954-2962	Lipids	CH_3 asymmetric stretching
~2915-2924	Lipids	CH_2 asymmetric stretching
~2870	Lipids	CH_3 symmetric stretching
~2847-2855	Lipids	CH_2 symmetric stretching
~1740-1730	Ester	C=O stretching
~1600-1690	Proteins – Amide I	C=O stretching
~1480-1580	Proteins – Amide II	N-H bend, C-N stretching
~1473-1462	Lipids	CH_2 bending
~1400	Fatty acids	COO^- symmetric stretching
~1240-1340	Protein – Amide III	C-OH bending vibration
~1238	Nucleic acids	PO_2^- symmetric stretching
~1171	Cholesterol	CO-O-C asymmetric stretching
~1120	Nucleic acids	C-O stretching
~1080	Nucleic acids and Phospholipids	PO_2^- symmetric stretching
~1030	Nucleic acids	COH deformation

5. Experiments

5.1. Sample preparation and classification

The tissue samples used in the experiments described below were obtained from patients with suspected muscle disease during surgical biopsy by appropriate skin incision and attaining full surgical access to the muscle. All the samples were diagnosed by the Department of Neuropathology at Jagiellonian University Medical College in Krakow (DN JUMC). The research was approved by the Jagiellonian University Medical College Ethics Committee (approval number: 1072.6120.249.2020). The biopsy samples were shock-frozen in liquid isopentane. For the purpose of the study the frozen archival material were cut in a plane perpendicular and parallel to the long axis of the muscle fibres into 8 µm thick slices using a cryomicrotrome (Leica Biosystems, CM 1860) at −20 °C. Sections for elemental and molecular measurements were placed onto silicon nitride (Si_3N_4) membrane windows (membrane thickness: 200 nm; window size: 2 × 2 mm^2 or 2,5 x 2,5 mm^2) from Norcada, Canada (see Figure 6). This substrate was chosen due to its suitability for both FTIR and SR-XRF techniques, as well as its previous studied and defined suitability [31]. The membranes were previously fixed to the dedicated PMMA holders. Further, the tissues were freeze-dried at -80 °C (without any further chemical treatment) and then stored in Petri dishes to avoid environmental impact contamination and destruction of the sample (see Figure 6). To classify the type of tissue and to select appropriate tissue areas for analyses, tissue slices directly adjacent to the slice attached to membrane were applied onto microscope slides and then stained with haematoxylin and eosin (H&E) for histopathological evaluation.

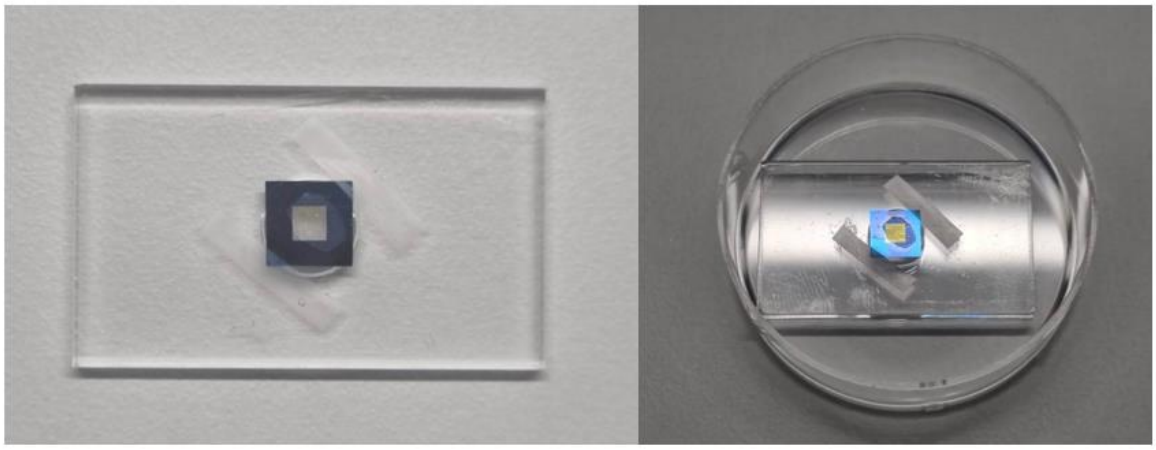

Figure 6. Silicon nitride window mounted on PMMA holder (left) and its storage container (right).

A schematic diagram of sample preparation is provided in Figure 7.

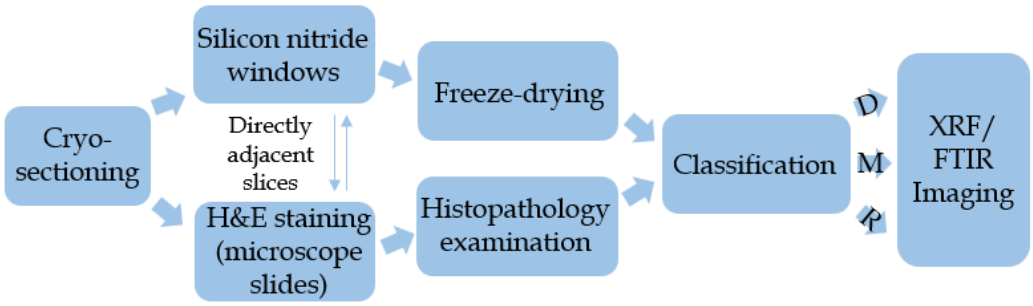

Figure 7. A diagram of sample preparation. Abbreviations: D—dystrophies group; M—myopathy group; R—reference group.

In the initial phase of the procedure the samples were classified into three main groups: the dystrophy - D, the myopathy - M, and the reference group - R. Cases showing signs of congenital muscle pathology were assigned to the dystrophy group, while all other cases that have muscle changes were assigned to the myopathy group. The reference group consisted of cases that did not show any muscle changes during the histopathological examination. However, one has to have in mind that it does not exclude illness.

Samples were collected from patients of both genders (13 for males and 11 for females), however the gender has not been taken into account in further analysis. The average age of patients was equal to 44 years (minimum 22 years, maximum 75 years). The total number of samples analysed in all the experiments was 24: 8 classified as

dystrophies, 9 classified as myopathies and 7 assigned to the reference group. Some of the samples were measured twice due to their different cutting methods - along and across the muscle fibres. A Table 2 shows the characteristics of all the samples.

Table 2. Overview of samples with diagnoses, age and gender of patients. *Numeration of samples was anonymized. (Abbreviations: f – female, m - male).

Sample*	Assignment	Patient's age [year]	Patient's Gender
D1	Dystrophy	29	m
D2	Dystrophy	69	f
D3	Dystrophy	58	m
D4	Dystrophy	23	m
D5	Dystrophy	27	m
D6	Dystrophy	56	f
D7	Dystrophy	46	m
D8	Dystrophy	27	m
M1	Myopathy	30	m
M2	Myopathy	48	f
M3	Myopathy	32	f
M4	Myopathy	32	f
M5	Myopathy	71	m
M6	Myopathy	75	f
M7	Myopathy	54	m
M8	Myopathy	58	f
M9	Myopathy	32	m
R1	Reference Group	22	f
R2	Reference Group	66	f
R3	Reference Group	44	m
R4	Reference Group	42	m
R5	Reference Group	33	f
R6	Reference Group	50	m
R7	Reference Group	35	f

The Figure 8 shows example microscopic images of silicon nitride membranes together with haematoxylin and eosin (H&E) staining images of a sample from the reference group – R4 sample and from the group affected by pathological changes – M4 sample.

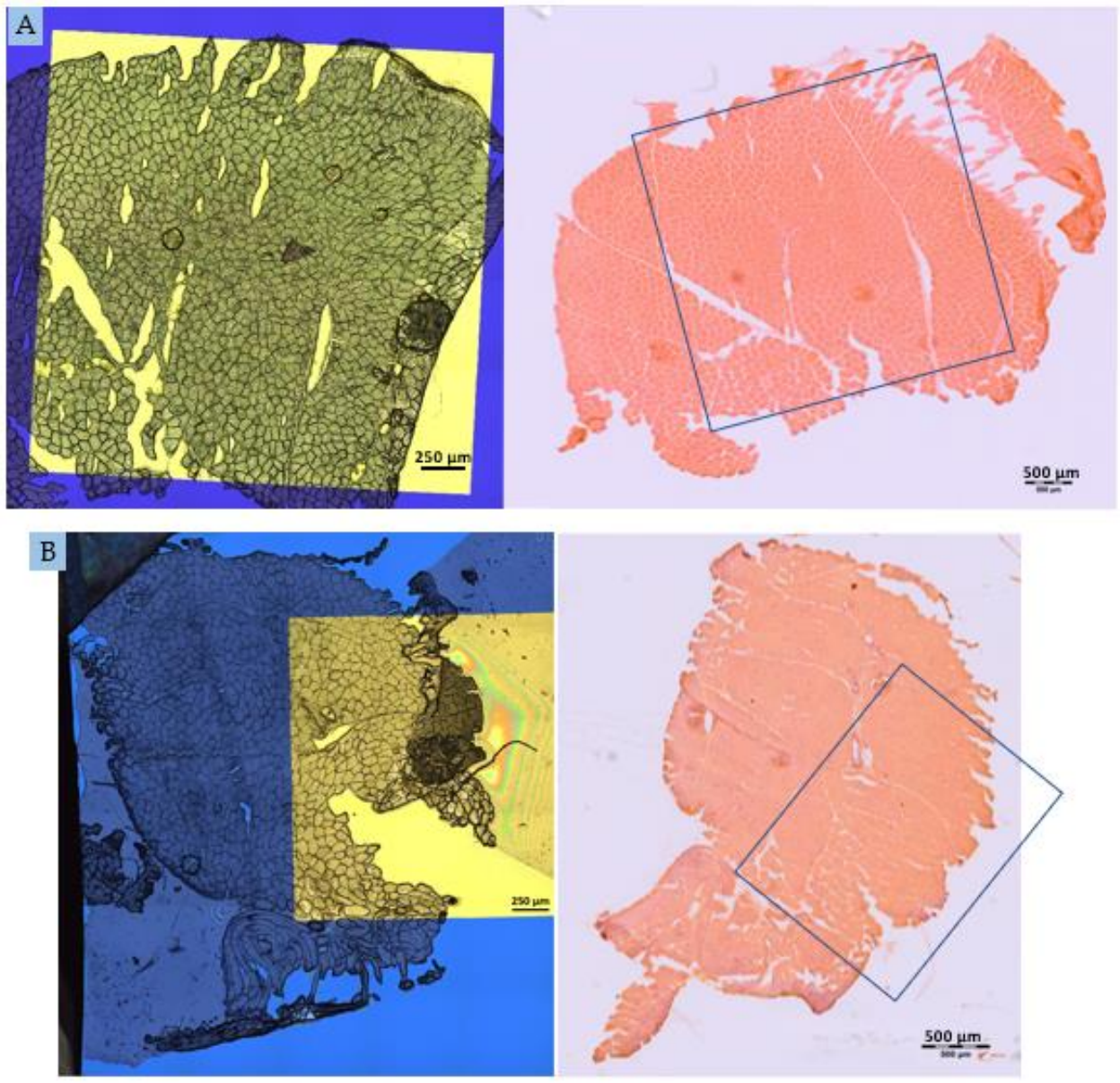

Figure 8. Microscopic images of silicon nitride membranes together with haematoxylin and eosin (H&E) staining images of an example sample from the reference group – R4 sample (A) and from the group affected by pathological changes – M4 sample (B).

5.2. Methodology

5.2.1. Synchrotron Radiation X-ray Fluorescence (SR-XRF) study

To determine the content as well as the distribution of the elemental composition of human muscle fibres as well as the endomysium, the SR-XRF method has been used. Due to limitations of the SR-XRF technique (time constraints for the high-resolution analysis of large sample areas) and limited access to the synchrotron facilities, two different experiments have been conducted with different spatial resolution. Synchrotron radiation was also used because of the size of the components under study - muscle fibre has a diameter of 10-100 μm. In most laboratory spectrometers, the resolution is no higher than 20 μm, which would significantly reduce the possibility to observe changes in the distribution of elements inside the muscle cell. By using a range of optics on the synchrotron, the beam is monochromatic and its intensity is much higher than in an X-ray tube spectrometer, which significantly reduces measurement time. The lower resolution – 5 μm at the DIAMOND Light Source Synchrotron, has been used for the imaging of the large sample areas as whole muscle fibres, whereas the higher, submicron resolution – 300 nm at the DESY Synchrotron, was utilised for detailed imaging of the border areas between muscle fibres and endomysium.

5.2.1.1. Experiment at I18 beamline at DIAMOND Light Source

The experiment, which used a lower resolution with the SR-XRF methods was carried out at the I18 beamline at the DIAMOND Light Source in Didcot, UK. This beamline uses 27 mm period undulator as a source of radiation. The beam focusing optics design is composed of four components. The first is a toroidal mirror located 25 meters from the source – it collimates the beam in the vertical plane and focuses the beam on the horizontal plane. The monochromator located at 27.7 meters from the source is composed of two Si (111) or Si (311) crystals, allowing the beam to cover energies between 2 and 20 keV. The third component is a pair of flat mirrors for harmonic rejection 38 meters away from the source; its task is to reject lower energies (<4 keV) using Rh or Ni strips, respectively, which are accessible by vertical offset.

Final focus of the beam is achieved using the fourth element – the pair of the Kirkpatrick-Baez mirrors located at the end of the beamline (about 42 meters from the source). Directly in front of each mirror are slits to remove scattered radiation, reduce the beam size, and optimize the beam [32]. During the experiment conducted for this research the beam was shaped to a size of 5 x 5 μm^2, and the radiation excitation energy was set to 13.95 keV.

Characteristic radiation detection was performed using two four-segment Vortex ME-4 SSD detectors by Hitachi, USA (total active area of 120 mm^2, crystal thickness of 1 mm, Be window thickness 12.5 µm, energy resolution at 5.9 keV <145 eV) coupled with Xpress3 readout system by Quantum Detectors, UK. The time of acquisition was 4 s for each pixel. The surface of the sample was positioned at 45° to the beam, and at 45° and 60° to the first and second detectors, respectively. The geometry of the measurement is shown in Figure 9.

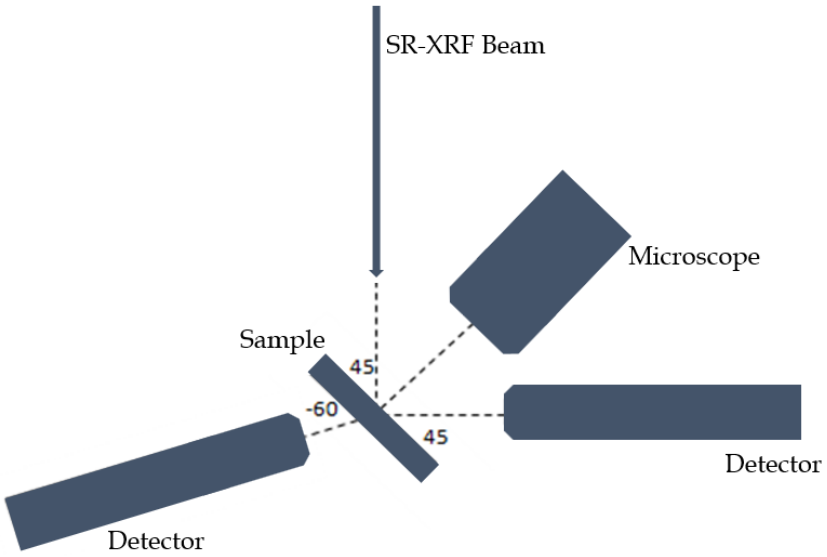

Figure 9. The scheme of the set-up used during the SR-XRF experiment on DIAMOND at I18 beamline.

Both detectors were placed approx. 5 cm from the sample. Measurements for all samples were carried out in a helium atmosphere due to the large sample – detector distances (in order to eliminate the absorption of characteristic photons in air), at room temperature under atmospheric pressure allowing detection of the elements with

Z higher or equal than 15 (Si[1], P, S, Cl, K, Ca, Cr, Mn, Fe, Cu, Zn and Br). As the detector contained a beryllium window, lighter elements could not be observed. For this experiment, the sample was considered thin for all analysed elements.

During the experiment, 24 maps from 13 samples were measured. Fully measured fibres were selected from each map, resulting in a total of 135 fibres. Of these, 17 were from samples diagnosed as dystrophy, 64 from samples classified as myopathy, and the remaining 54 constituted the reference group.

5.2.1.2. Experiment at P06 beamline at PETRA III

In order to check for differences in the elemental composition of the connective tissue surrounding the fibres in muscle tissue - the endomysium, measurements were carried out using the SR-XRF method at the P06 beamline at PETRA III facility of the Deutsches Elektronen-Synchrotron DESY in Hamburg, Germany. The beamline operates with 31.4 mm period undulator. The first optical element of the beamline, located at 38.5 m from the source is the cryogenically-cooled double-crystal Si (111) or Si (311) monochromator on this beamline can cover energies between 2.4 and 100 keV. Behind the monochromator there are the pair of flat mirrors coated with Cr, Si or Pt, which are used to suppress the higher harmonics of the radiation. They enable the radiation to be cut off in range from 4 to 30 keV. The next optical element located 43.3 m from the source are prefocusing X-ray refractive lenses. The beam achieves its final focus using Kirkpatrick-Baez mirrors (5-23 keV energy range) or compound refractive lenses (15-35 keV energy range) placed in the experimental hutch around 90 meters from the source [33].

During the experiment, the beam size was shaped into a 300 x 300 nm^2 with Kirkpatrick-Baez mirrors and the scan step was set to 1 μm. The acquisition per was set to 4 s. The energy of excitation used in this experiment was 16.5 keV. The characteristic radiation was detected using a Vortex EM SDD detector by Hitachi, USA (active area of 50 mm^2, crystal thickness of 1 mm, Be window thickness 12.5 μm, energy resolution at 5.9 keV <145 eV). The surface of the sample was positioned at 90° to the

[1] Si was not taken into account for analyse due to a fact that is present into a support

beam and at 1° to the detector (Figure 10). Detector was placed approx. 2 cm from the sample. All measurements were carried out in an air atmosphere allowing detection of elements with Z higher or equal than 16. Due to the use of grazing-exit geometry which enhances the self-absorption effects in the sample it could be considered as thin for elements with atomic number greater than or equal to 26. Therefore, only elements such as Fe, Cu, Zn, Br and Rb were considered in the analysis.

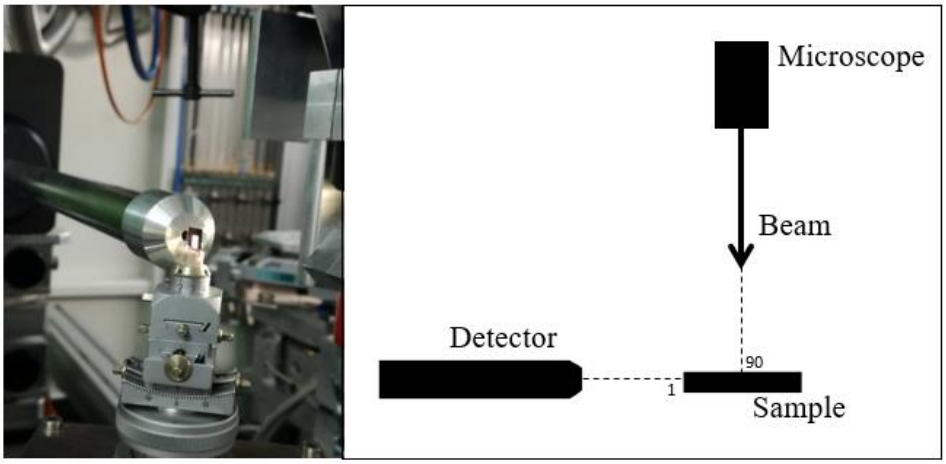

Figure 10. The image and scheme of the set-up used during SR-XRF experiment on DESY at P06 PETRA III beamline.

Due to the exceedingly small beam size and the relatively long measurement time per pixel, during the experiment 8 maps from 7 samples were measured. It is reasonable to assume that the composition of the endomysium may be correlated with the composition of the fibres that surround it, especially in the case of fibres that have visible pathological changes. Due to this fact, the connective tissue measured in the areas in question was divided into fragments between the individual muscle cells. The method of dividing the endomysium is shown in Figure 11. 15 connective tissue fragments were used in the analysis - 4 from samples diagnosed as dystrophy, 3 from a sample classified as myopathy, and 8 representing the reference group. The study group consisted of connective tissues surrounding the fibres with the division to the endomysium located between the individual fibres, if possible.

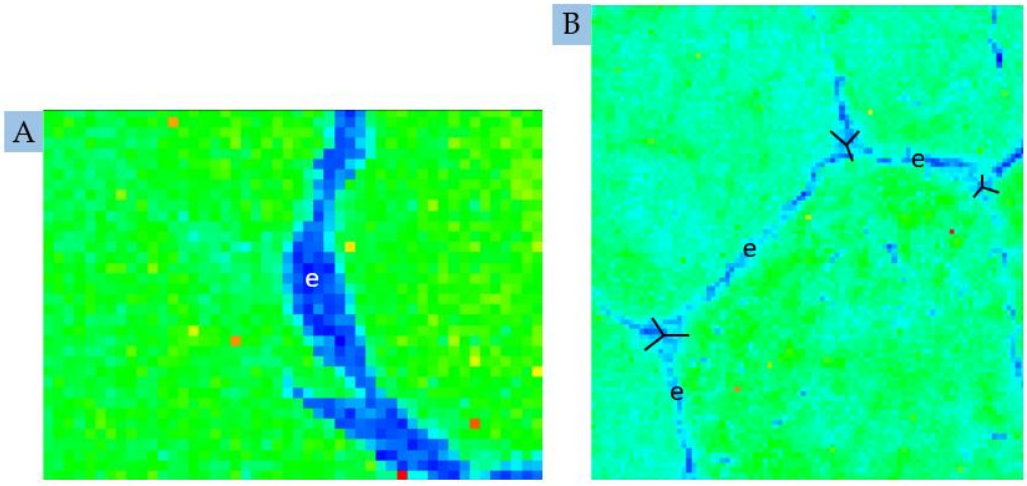

Figure 11. Diagram showing the division of connective tissue into fragments based on ROI images of sum spectrum. A - all pixels from the endomysium have been portrayed as a whole fragment, B - the connective tissue has been divided into fragments between the fibres that border it. Abbreviations: e – endomysium.

5.2.1.3. SR-XRF data processing

The data acquired during both experiments were pre-evaluated with use of in-house developed script created in the Python environment. Using PyMCA software (ESRF, version 5.8.0, [34]), ROI images of sum spectrum were obtained for all measured samples, from which a binary image was created. A diagram of the binarization process is shown in Figure 12.

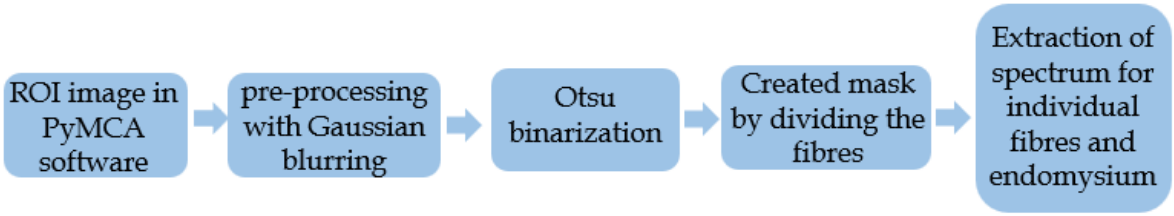

Figure 12. Diagram of the binarization process.

Image binarization was done using the Python environment by pre-processing with Gaussian blurring and then applying the Otsu binarization method [35]. As the result, black-and-white image served as a mask to better separate on the maps the irregular area of fibres from those of connective tissue between the cells - the

endomysium. A graphic illustration of obtaining the mask is presented in Figure 13 for DIAMOND Light Source Experiment and in Figure 14 for DESY Experiment. Using the created mask and the data cube[2] files obtained during the measurements, the script was able to easily extract the spectra assigned to the pixels of a particular fibre or endomysium, sum them, and save in an ASCII file. The thus obtained spectra were fitted in the PyMCA software to obtain information about net peak areas for each element. Normalization of the data was done in two steps: to the value of the area under the Compton scatter peak [36] to minimize the effect of the variation of thickness and density of the sample, and to the size of give fibre (expressed in the number of pixels). The obtained data were subjected to statistical analysis using STATISTICA software (TIBCO Software Inc., StatSoft Polska, version 13.3, [37], [38]).

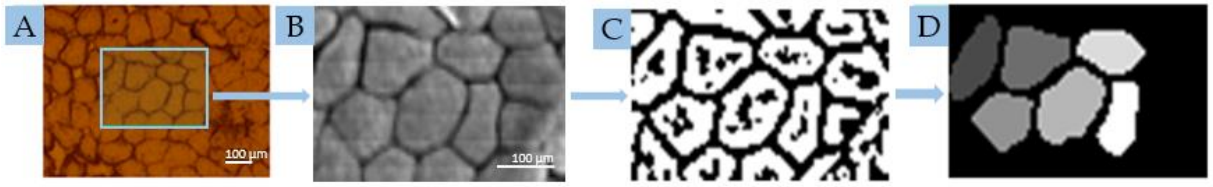

Figure 13. Graphic illustration of obtaining the mask by binarization for DIAMOND Light Source Experiment: (A) image of the R6 sample from an optical microscope with the highlighted area of measurement; (B) ROI image; (C) ROI image binarization; (D) created mask.

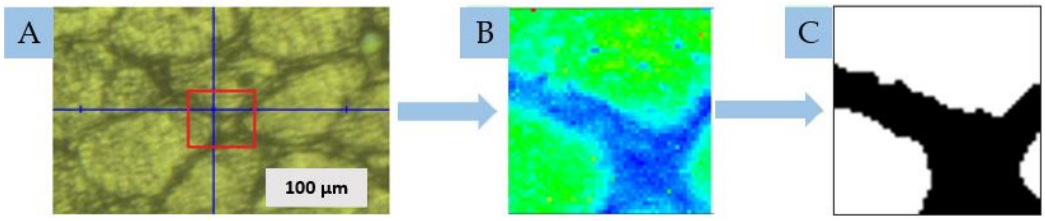

Figure 14. Graphic illustration of obtaining the mask by binarization for DESY Experiment: (A) image of the M3 sample from an optical microscope with the highlighted area of measurement; (B) ROI image; (C) created mask.

[2] N x M x Ch where N x M is the size of map in pixels, and Ch is the number of spectra channels

5.2.2. Fourier-transform infrared microspectroscopy (FTIR) study

In order to study the biomolecular composition of the muscle samples, the Fourier-transform infrared microspectroscopy (FTIR) method was used with laboratory setup as well as with the use of synchrotron radiation. Measurements using the synchrotron source were made on the B22 beamline at the DIAMOND Light Source in Didcot, UK. As with the use of the SR-XRF technique, the greatest impact on the measurements made was due to the limitations of the technique - time constraints for high-resolution analysis of large sample areas as well as access to the instrument for synchrotron measurements. Thus, using a laboratory instrument with a globar source, a large sample area was analysed at low spatial resolution, while using a synchrotron source instrument, smaller areas were measured for endomysium analysis. Laboratory conditions were used to check for possible radiation damage after hard energy XRF measurements.

Globar source measurements were carried out at the Department of Physics and Applied Computer Science, AGH University of Science and Technology using a commercial Thermo Scientific Nicolet iN10 spectrometer (Nicolet iN10 experiment), while measurements made on the Thermo Scientific Nicolet 8700 (Nicolet 8700 experiment) spectrometer were used to determine possibly occurring radiation damage in the samples.

5.2.2.1. Experiment at AGH FTIR Laboratory

In order to check whether there were differences in biomolecular composition between the samples categorised into the different groups, measurements were made covering the entire specimen area using a Thermo Scientific Nicolet iN10 spectrometer, equipped with a ceramic radiation source and a liquid nitrogen cooled MCT detector (Figure 15).

Figure 15. Measurement instruments - Thermo Scientific Nicolet iN10 spectrometer, on which the experiments were carried out.

During this experiment, the entire muscle tissue located on a 2 x 2 mm^2 silicon nitride membrane was mapped (Figure 16). Measurements took place in transmission mode with the spectral resolution set at 8 cm^{-1}. Before each sample measurement, a background measurement took place with the number of scans of 16 and 64 for the sample and background, respectively. Sample mapping was made using an aperture limited to 150 x150 μm^2 in the mid-IR range (3800-900 cm^{-1}). Data collection was carried out using Picta OMNIC software (Thermo Scientific, version 8.1), while QUASAR software (version 1.7.0, [39], [40]) was used for further spectral analysis.

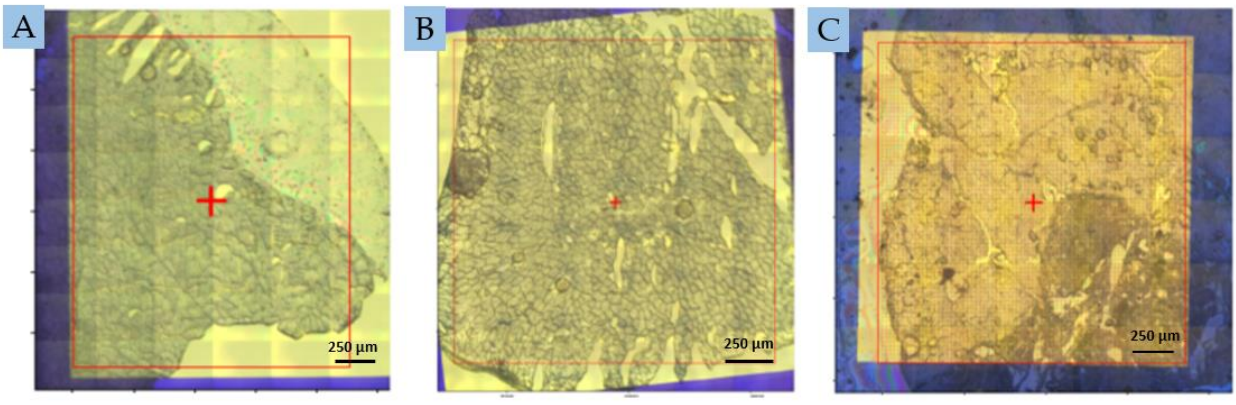

Figure 16. Example samples A – D1, B – R4 and C – M5 measured during the experiment, along with the mapping area marked with a red rectangle.

During the measurements, 23 samples were measured - 8 dystrophies, 10 myopathies and 5 reference groups. From the measured samples, 129 areas were extracted for further analysis - 50, 55 and 24 for the dystrophy group, myopathy group and reference group, respectively. These were the areas with a constant size of 10 x 10 um^2 or 9 x9 um^2, were selected in areas that have no holes and cracks - spreading the sample on the membrane substrate and have no visible defects - Figure 16. For such selected areas, absorption spectra from individual measurement points were extracted utilizing OMNIC software and then used in further analyses.

5.2.2.2. Experiment at B22 beamline at DIAMOND Light Source

To check whether there is a difference between the biomolecular composition in the endomysium of the samples studied, measurements were made using synchrotron radiation on the B22 beamline at the DIAMOND Light Source in Didcot, UK (SR-FTIR experiment). The beamline system consists of a vacuum tank that contains two periscope systems - each with two mirrors. The first flat mirror is designed to reject the X-rays in the beam. The infrared beam light is then reflected onto the ellipsoidal mirrors, which redirects it to one of the two end stations. Both stations consist of Bruker Vertex Fourier transform interferometers and also Hyperion 3000 IR microscopes using a high-sensitivity MCT detector [41]. Measurements were made in transmission mode with a spectral resolution of 4 cm^{-1}. A knife-edge aperture limited to a size of 5 x 5 μm^2 in the mid-infrared (4000-600 cm^{-1}) was used to record maps. The number of scans per measurement of the sample and background are 128 and 256, respectively. The use of IR generated by the synchrotron allows high spatial resolution and a high signal-to-noise ratio, making it achievable to study micrometre-sized areas of samples. This made it possible to visualise areas of connective tissue between muscle fibres.

During the experiment, areas from 7 samples - 3 dystrophies, 2 myopathies and 2 samples from the reference group - were measured. From the regions in question that were measured, connective tissue-derived spectra were selected for further analysis - Figure 17. The measurements were made using OPUS software (version 8.7), their further analysis was performed using QUASAR software.

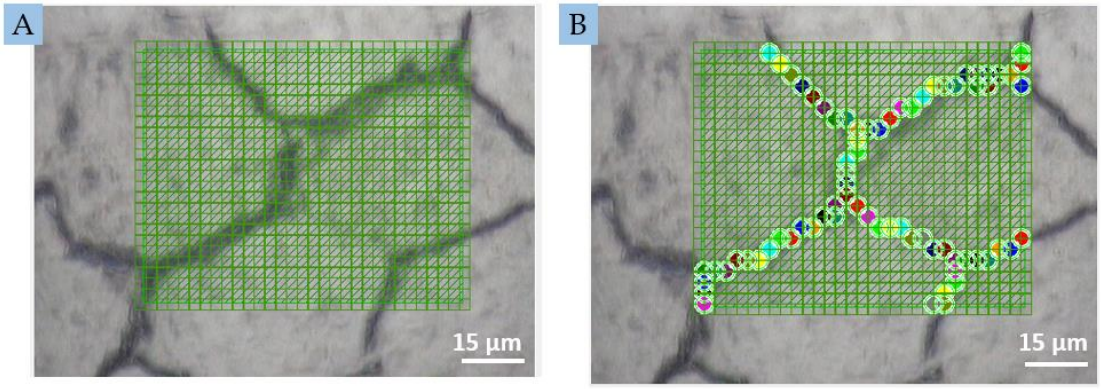

Figure 17. An example of a microscopic photograph of a sample – R5, together with A - the area of measurement - green grid and B - highlighting the area of the endomysium that was further analysed in this experiment.

5.2.2.3. Radiation Damage assessment experiment

The overall measurements of the sample using the FTIR method carried out before the SR-XRF measurements to avoid potential macromolecular changes induced by synchrotron radiation. However, the SR-XRF experiment was followed by an assessment of radiation damage in the tissue areas studied with the use of the FTIR microspectroscopy. For this purpose Thermo Scientific Nicolet 8700 spectrometer (Figure 18) coupled with Continuum IR microscope available at the Department of Physics and Applied Computer Science, at the AGH University of Science and Technology was used.

Figure 18. Measurement instruments - Thermo Scientific Nicolet 8700 spectrometer with the Thermo Nicolet Continuum microscope, on which the experiments were carried out.

Again, areas that had previously been measured by both FTIR and SR-XRF methods were remeasured here. Spectra acquisition was made in transmission mode with a spectral resolution of 8 cm^{-1}. The number of scans of the sample spectrum and the background spectrum were 100 and 400, respectively. The size of the aperture used for map collection was 20 x 20 μm^2 with a mid-infrared range of 3800-900 cm^{-1}.

In order to investigate whether there were differences in biomolecular composition based on possible radiation damage, 5 samples were re-measured. Specifically, eight separate areas were measured from the following samples: one case of dystrophy (1 area), 2 cases of myopathy (4 areas) and 2 cases of reference groups (3 areas). Figure 19 shows an optical microscope image of the sample, on which the areas measured by the SR-XRF method - the blue area, and by the FTIR method - the red box - have been marked. The measured areas from both globar FTIR measurements - carried out before and after the SR-XRF measurements, were divided into spectra, which were further analysed.

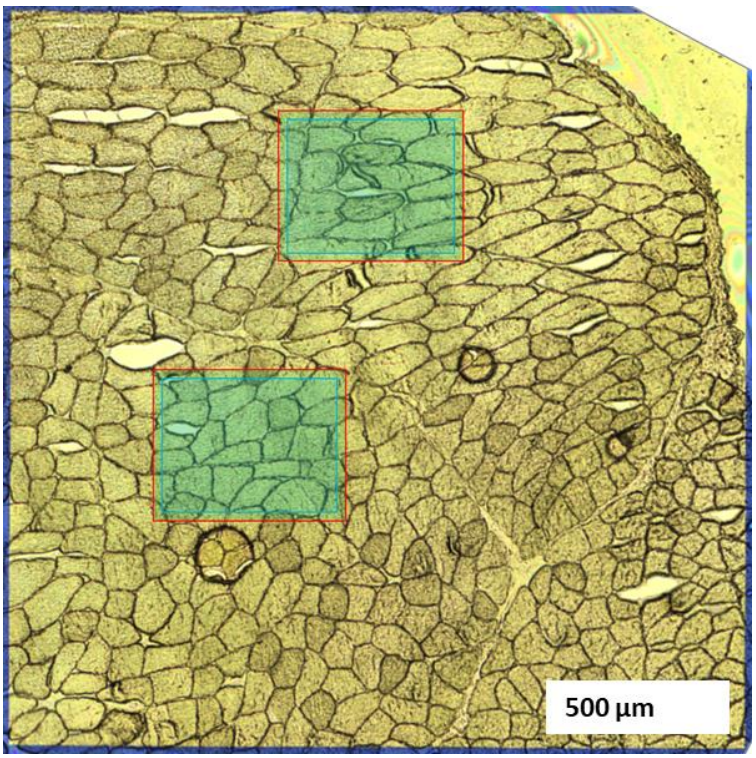

Figure 19. Optical microscopy image of an exemplary M9 sample measured during the radiation damage experiment. The area measured by SR-XRF is marked in blue and the area measured by FTIR microspectroscopy in red rectangle.

5.2.2.4. FTIR Data processing

For each measured sample from which spectra have been extracted, the Outliers function using the Isolation Forest method was applied to eliminate the 10% most outlier spectra. Spectral analysis for every sample was implemented for the 3800-900 cm^{-1} spectral range. Moreover the spectral range around 2400 cm^{-1} assigned to contribution of atmospheric carbon dioxide was excluded from the analysis. The resulting spectra were normalized using the Standard Normal Variate (SNV) procedure, which consists of subtracting the spectrum from its mean and dividing it by its standard deviation. A linear baseline correction over the entire spectrum was then applied. The Integrate Spectra function was used to determine the net area under the peak. The analysed peaks areas in the obtained IR spectres are shown in the Table 3 and Figure 20.

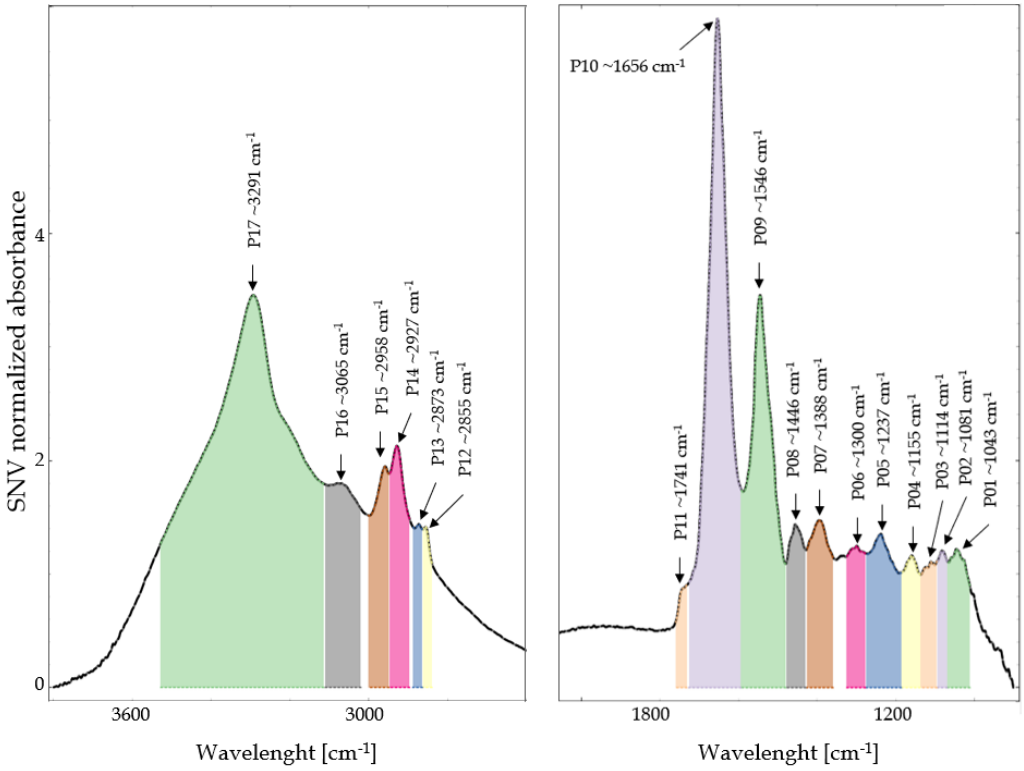

Figure 20. Example spectrum captured for muscle tissue. The spectrum was subjected to SNV normalisation and linear base correction over the entire range. The absorption bands analysed in this work are indicated in the figure.

Table 3. Main absorption bands and their assignments investigated in this thesis; based on [42][43][30].

Peak No.	Wavenumber (cm^{-1})	Assignment	
P01	~1043	nucleic acids	COH deformation
P02	~1081	nucleic acids and phospholipids	PO_2^- symmetric stretching
P03	~1114	nucleic acids	C-O stretching
P04	~1155	phospholipids, cholesterol esters and triglycerides	CO-O-C asymmetric stretching
P05	~1237	nucleic acids	PO_2^- asymmetric stretching
P06	~1300	protein – Amide III	C-OH bending vibration
P07	~1388	fatty acids	COO^- symmetric stretching
P08	~1446	lipids	CH_2 bending
P09	~1546	protein – Amide II	N-H bend, C-N stretching
P10	~1656	protein – Amide I	C=O stretching
P11	~1741	ester	C=O stretching
P12	~2855	lipids	CH_2 symmetric stretching
P13	~2873	lipids	CH_3 symmetric stretching
P14	~2927	lipids	CH_2 asymmetric stretching
P15	~2958	lipids	CH_3 asymmetric stretching
P16	~3065	proteins – Amide B	N-H stretching
P17	~3291	proteins – Amide A	N-H stretching

An analysis of the relationships of the different bands to each other was also carried out. All analysed parameters are presented in the Table 4.

Table 4. Analysed parameters of the relations between the designated bands.

Relationship of bands (cm^{-1})	Indication
~1081/~1656	Distribution of compounds containing PO^{2-} group in relation to proteins - Amide I
~1237/~1656	Protein/DNA content
~1388/~1656	Distribution of COO^{-} group-containing compounds in relation to proteins - Amide I
~1546/~1656	Structural changes of proteins (Amide II to Amide I)
~1741/~1656	Distribution of esters (C=O bond) in relation to proteins - Amide I
(~2855 + ~2873 + ~2927 + ~2958) /~1656	Lipid to protein ratio - Amide I
~1741 / (~2855 + ~2873 + ~2927 + ~2958)	Ester to lipids ratio
~2927/~2958	Degree of lipid saturation

Statistical analyses such as the Kruskal-Wallis test and multivariate discriminant analysis were carried out using QUASAR and Statistica software.

5.3. Statistical analysis

The final result of the conducted experiments should be the acquisition of meaningful information on the chemical or molecular composition of the studied material. The source of this information is the final result of the analysis of samples taken and prepared in the right way. Inappropriate handling at any stage carries the possibility of misinformation. It is therefore necessary to ensure the representativeness of the sample, the stability of its composition and also the appropriate choice of statistical methods used in the analysis.

The purpose of the statistical analyses performed in the present study was to determine the observable changes in the qualitative characteristics (changes in elemental and biomolecular composition) of human muscle samples affected by pathological changes through neurodegenerative diseases compared to reference tissues. The pre-processed data obtained in the SR-XRF and FTIR experiments were checked using the Shapiro-Wilk test to determine agreement with a normal distribution. Based on the results, it was concluded that for most cases the data did not reveal a normal distribution. Further statistical analysis was therefore based on nonparametric tests. For analysis with small data numbers and no way to check the normality of the distribution, nonparametric statistics were also used. Spearman's correlation coefficient was used to examine possible correlations between individual elements or biomolecules analysed in the samples. The Kruskal-Wallis test was used to verify the statistical significance of differences in the content of elements and biomolecules. Multivariate discriminant analysis was carried out to check which specific factor most influences the variation in the samples. For each statistical test, a p-value less than or equal to 0.05 implied statistical significance.

5.3.1. Spearman's correlation coefficient

Spearman's correlation coefficient was used to describe the strengths of correlation of two attributes when:

- the attributes are measurable, and the study population is small in number,
- there are outlier observations,
- the attributes are qualitative, but there is a possibility of ranking them.

Study n individuals, described by two attributes, can be ordered by the value of each attribute separately. The individuals in each ordering are assigned with a number that corresponds to their place in the given ordering (1, …, n). The number of each measurement is called a rank. This procedure can be carried out for measurable variables that do not have a normal distribution. This change of specific values to their corresponding ranks also nullifies the impact of outlier scores. Spearman's correlation

coefficient assumes values in the range $-1 < r_S < 1$. The closer the value of the coefficient is to the number 1 (or -1), the stronger the studied relationship is.

Spearman's rank correlation coefficient is calculated from the formula:

$$r_S = 1 - \frac{6 \sum_{i=1}^{n} d_i^2}{n(n^2-1)} \quad (2)$$

where d_i is the difference between the ranks of the corresponding feature attributes [37], [44], [45].

In order to verify the presence of correlations between the studied elements in SR-XRF measurements, a correlation analysis was performed by establishing Spearman rank correlation coefficients. The obtained correlation coefficients were considered statistically significant when the p-value was < 0.05.

The value of the correlation coefficient determines the strength of the relationship was conducted based on Guilford's interpretation of the magnitude of significant correlations:

- ≤ 0.2 lack of relationship,
- $0.2 - 0.4$ - a clear but low linear relationship,
- $0.4 - 0.7$ - moderate linear dependence,
- $0.7 - 0.9$ - significant linear dependence,
- ≥ 0.9 - extraordinarily strong linear dependence.

5.3.2. Kruskal-Wallis test

The Kruskal-Wallis test is the nonparametric equivalent of single-factor analysis of variance, which compares the distribution of a variable in more than 2 populations. With the help of this test, it is possible to evaluate whether n independent samples come from the population with the same median – this is the null hypothesis. This test does not require a number of assumptions such as the distribution of variables close to a normal distribution, equality of groups or equality of variances within groups. The only requirements for the test are the measurability of the dependent variable on

at least an ordinal scale and the independence of the observations analysed in the groups. Since a significant test result indicates that there are, or not, statistically significant differences between the analysed groups, in order to check between which groups there are differences, multiple comparisons - post-hoc tests - must be carried out.

A Kruskal-Wallis test was carried out to examine if statistically significant differences exist between the elements or biomolecules in different groups of samples. To eliminate outliers in a SR-XRF experiments a two-sided Tukey test was performed, with the outlier replaced by the average value calculated for each element. The result of the Kruskal-Wallis test was considered statistically significant when the p-value for the results was below 0.05. Post hoc tests were carried out to see which groups showed the differences. Again, the result was considered statistically significant when the p-value was > 0.05. The results of the tests were presented graphically with superimposed information of statistical significance between all, as well as individual groups on boxplots [44], [46].

5.3.3. Multivariate discriminant analysis

Discriminant analysis was used to decide which variables distinguish - discriminate - between two or more groups. The analysis searches for rules of conduct to assign multidimensional objects to one of many populations with known parameters with the minimum possible classification mistakes. The main idea is to resolve whether groups differ due to some variable, and then use this variable to predict the group belongings of cases. In fact, there are several variables that are tested for their best contribution to discriminating groups. Thus, it is a statistical technique to study differences between two or more groups by analysing several variables simultaneously. The variables used to discriminate between groups are called discriminating variables. It can be distinguished two stages in this analysis: the learning stage - where is find classification rules based on the variables, and the classification stage - where is classify objects based on the class characteristics found. In order to convince of the correctness of the model created, it is rather necessary to use other data for classification than those that form the discriminant functions. So,

when the examination group is large, it gives the opportunity to randomly create two subsets - one to derive the function, the other to test the classification.

Discriminant analysis is sensitive to outlier points. They artificially increase the variance and the mean value, which violates the assumption of homogeneity of variance.

Multivariate discriminant analysis (MDA) is a statistical method that aims to evaluate how individual characteristics, or variables, affect the separation of examined samples into groups predetermined by histopathological diagnosis. It also allows to evaluate the effectiveness of the separation, by comparing the division with the prespecified diagnosis. This technique identifies the variables that are contributing most to the division of groups. If a variable's contribution is not significant, as determined by the partial Wilks' Lambda value as well as the values of the parameter p-value, it can be omitted from the final model [38], [47].

6. Measurement results

6.1. Content and distribution of elements on fibres and endomysium

The first part of the study (Diamond SR-XRF experiment) involved qualitative determination of the elemental composition and elemental spatial distribution of muscle fibres, both those affected by lesions and those defined as a reference group. The study was focused on regions where atrophic and hypertrophic fibres are visible. In contrast, in case of the samples from the reference group the attention was paid to check whether the fibres were of comparable size and did or did not originate from a single fascia. The areas for measurement were first selected under a microscope using a stained sample, and then identified on a sample dedicated for spectroscopic measurements applied to silicon nitride windows.

The distribution of elements in the fibres visible on the element intensity maps (Figure 21) indicates their heterogeneity. Elements such as Cl, K or S are distributed closer to the outer parts of the fibres, while P, Ca or Fe (despite visible hot-spots) are located in the entire cell volume. Br and Cu are distributed throughout the entire surface of the tissue, with no apparent distinction between structures. The distribution of zinc may suggest ongoing changes in the cell, despite the sample being diagnosed to the reference group. The lack of homogeneity of the elemental distribution in the measured areas affected the statistical analysis carried out, and for this reason only fibre areas that were measured completely during the experiment were taken into account in the analyses.

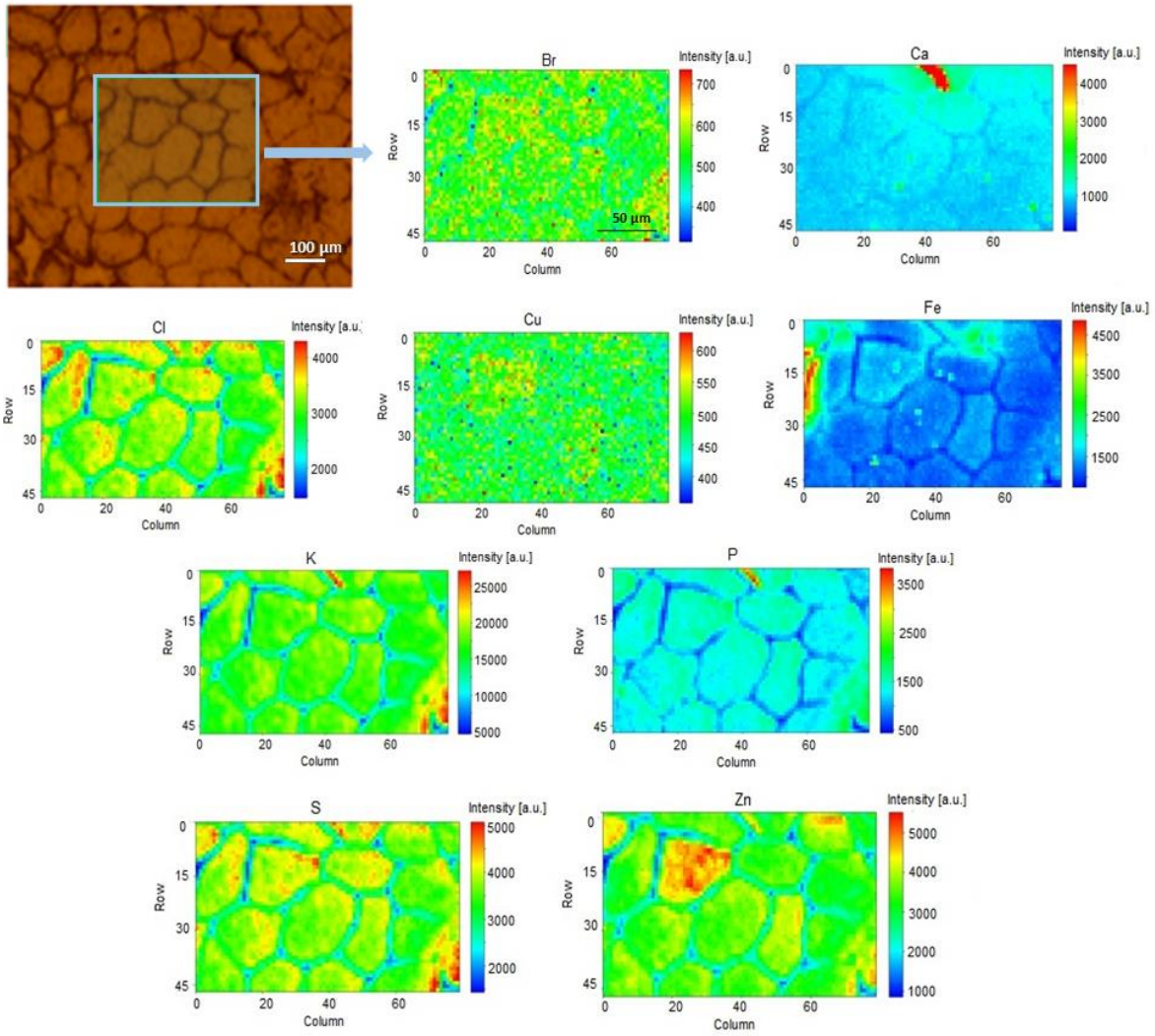

Figure 21. Maps of elemental distributions for a sample R6 of the reference group. The areas shown show intensities that have not been normalised to the Compton peak.

An example spectrum acquired for one of the samples is shown in Figure 22.

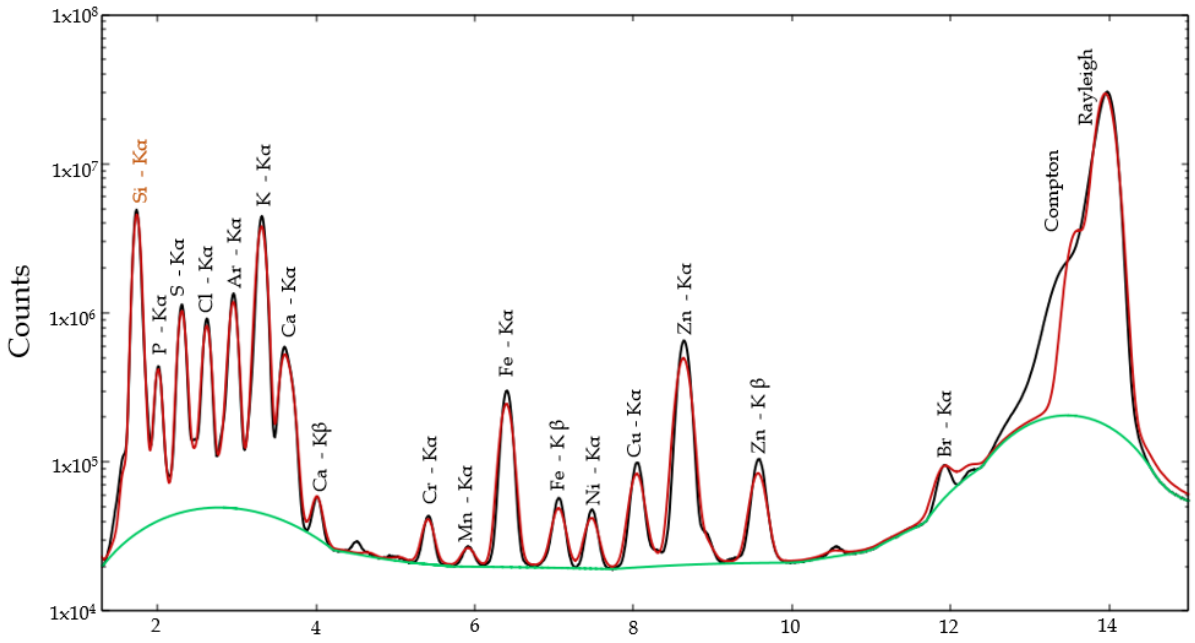

Figure 22. The spectrum of characteristic X-ray radiation of a selected fibre from the sample R6 from reference group from measurements at the I18 beamline at the DIAMOND Light Source. Measurement geometry 45/45° with energy 13.95 keV, beam size 5x5 μm², measurement time 4 s per pixel. The black line shows the spectrum obtained from the measurements, while the red line shows the fit obtained using the PyMCA programme.

In the case of Kruskal-Wallis test, for all the elements at least one group showed significantly statistical differences. For or all groups (D, M and R), elements such as P, K, Ca and Fe were considered statistically significant in fibres differentiation. However, for the Myopathy - Reference pair, elements such as S, Cl, Cr, Mn, Cu, Zn and Br were considered statistically insignificant. The results of the comparisons between the groups are shown in Figure 23.

For all the analysed elements, it can be seen that the values of normalized intensities of characteristic radiation are lower for cases that come from the dystrophic group. It is worth emphasizing here that dystrophies are diseases that are inheritable. Thus, low levels of the studied elements among fibres assigned to dystrophic groups may emphasize deviations from biomechanical processes involved in construction as well as tissue conditioning.

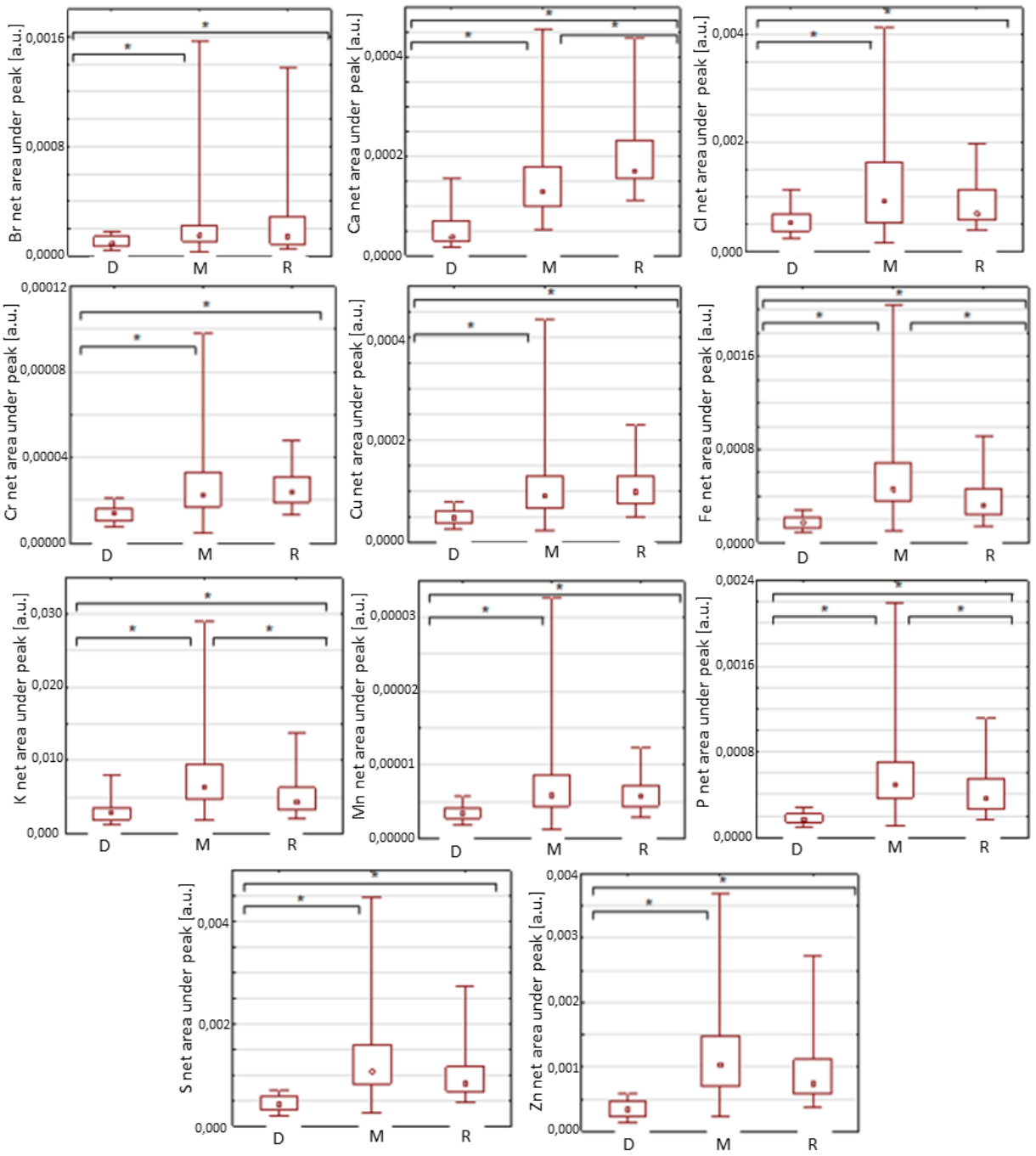

Figure 23. Comparison of the statistical significance of differences in the content of the analysed elements in muscle fibres between the test groups (median, ±0.25-0.75% percentile and min-max values). Abbreviations: *- statistically significant difference ($p < 0.05$) determined by Kruskal-Wallis test; D - dystrophy group (n=17); M - myopathy group (n=64); R - reference group (n=54).

For the correlation analysis, a large part of the analysed elements showed an extraordinarily strong linear relationship, for which the correlation coefficient reached a value above 0.9. Correlation coefficients for all pairs of elements assumed positive

values, which may indicate an overlap of elevated elemental content. Relationships for pairs such as P and S, P and Fe, P and Zn, S and Fe, S and Zn, Mn and Cr, Cr and Cu, and Cu and Mn appeared to be the strongest and assumed values above 0.95 (Figure 24).

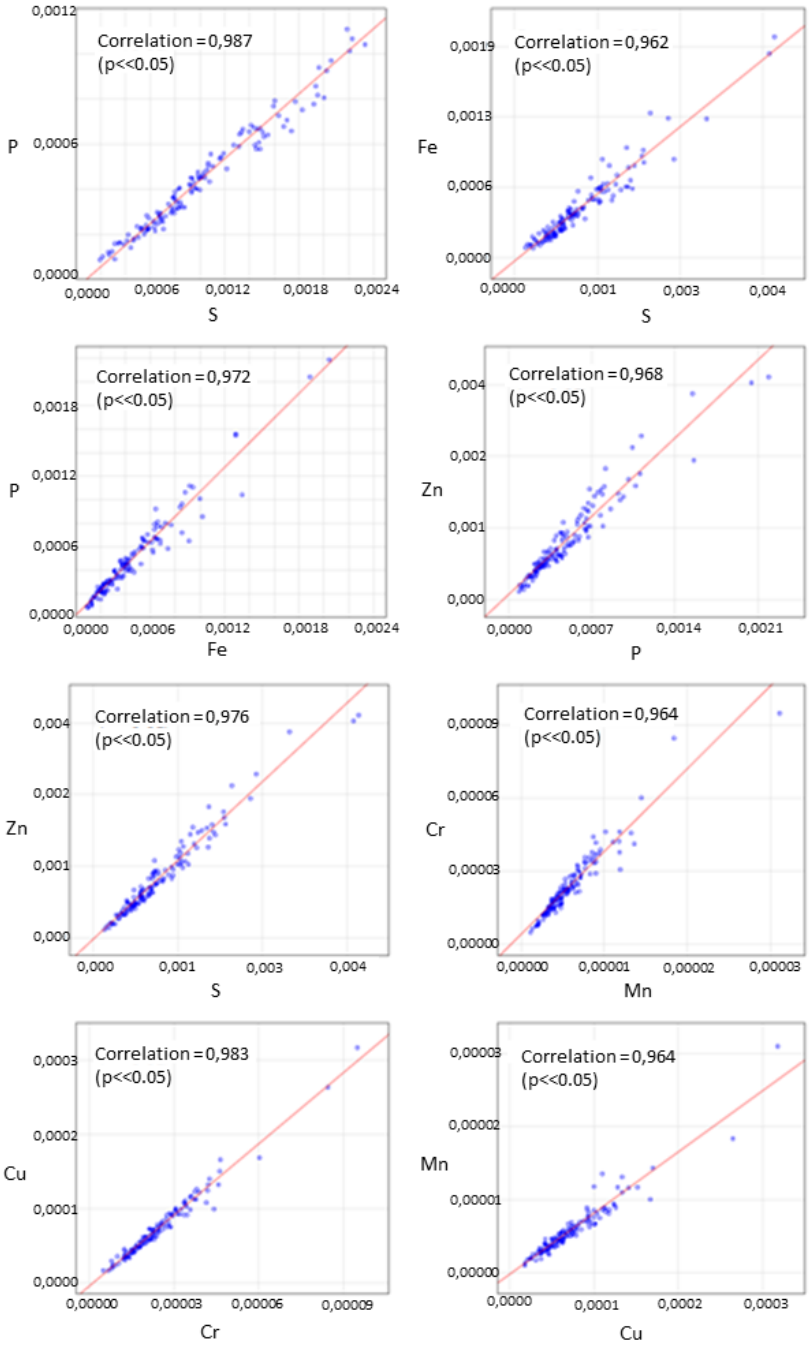

Figure 24. Correlation diagrams for the elements of the strongest relationships for fibres (Spearman's correlation coefficient > 0.95). The axes show the value of the net area under the peak of a given element normalised to the value obtained for the Compton peak.

To determine which of the analysed elements have the greatest impact on differentiation, a multivariate discriminate analysis was carried out. 70% of randomly selected fibres were used to create the model for both cases. Based on the values obtained for the partial Wilks lambda – Table 5, it was found that elements such as Ca, K, Cr and P had the greatest influence on differentiation, while the elements S, Mn, Fe, Zn and Br were outside the model.

Table 5. Partial Wilks' lambda value for muscle fibre analysis.

Element	**Ca**	**K**	**P**	**Cu**	**Cl**	**Cr**
Partial Wilks' lambda	0.536	0.696	0.754	0.929	0.905	0.536

A discriminant function was also obtained, which are combinations of characteristic X-ray intensities of the elements.

$$D1 = 6.564\,P - 1.314\,Cl - 1.895\,K + 2.229\,Ca - 2.001\,Cr - 2.063\,Cu \quad (20)$$

$$D2 = 1.012\,P - 0.310\,Cl + 1.491\,K - 0.798\,Ca - 1.474\,Cr - 0.406\,Cu \quad (21)$$

Elements such as P and Ca have the greatest impact on the first function, while the second function is affected by K and Cr. The graphical representation of the distribution of fibre cases in the space of discriminant functions is illustrated in Figure 25.

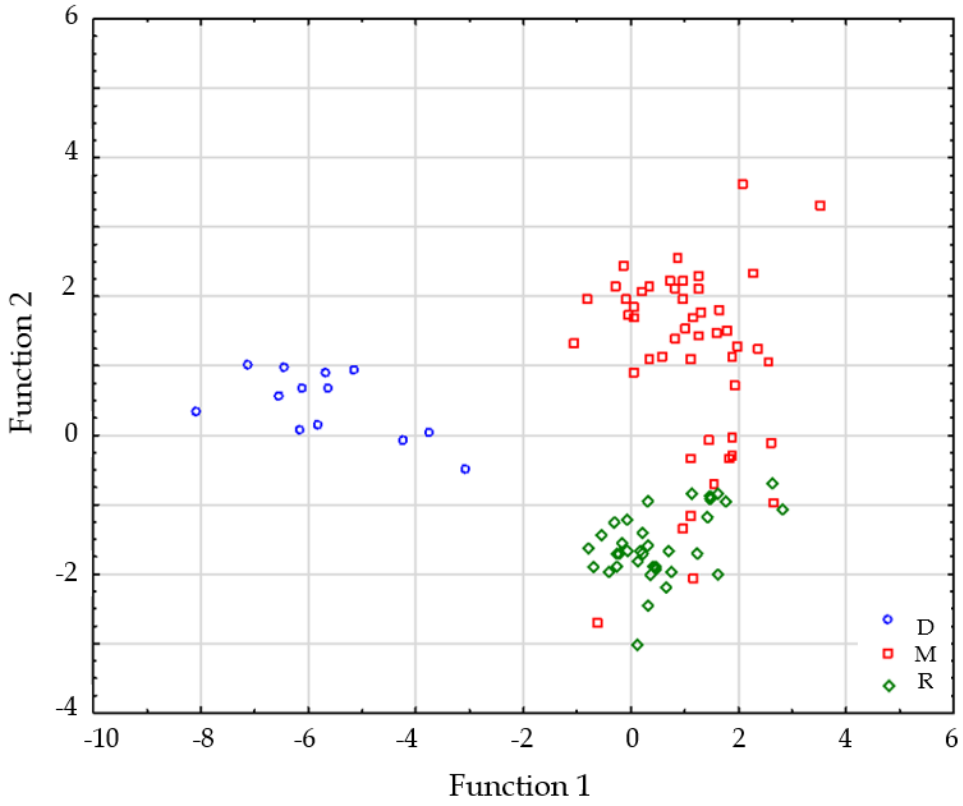

Figure 25. Graphical representation of configurations of discriminant function divided into groups represented by points in the discriminant variable system for muscle fibres analysis.

In order to check the validity of the created models, a reverse analysis was carried out using the data that was applied to build both models. In the case of the fibre analysis, 93% of the cases were classified as consistent with the diagnosis (Table 6).

Table 6. Classification matrix for matching fibres using multivariate discriminant analysis for 70% randomly selected fibres. Abbreviations: D - dystrophy group; M - myopathy group; R - reference group.

	Group	**%**	**Assignment**			**Total**
			D	M	R	
Diagnosis	D	100%	13	0	0	13
	M	88%	0	43	6	49
	R	97%	0	1	37	38
	Total	93%	13	44	43	100

Differences in assignment relative to diagnosis are shown by six fibres diagnosed as myopathy and assigned by the model to the reference group, and one fibre diagnosed as unaffected by disease and classified by the model as myopathy. For the dystrophy group, all fibres were assigned to their category by the model, which may indicate the severity of the disease and changes in the structure of the analysed cells, which may be reflected in differences in elemental composition. The fibre from the sample from the reference group and allocated by the model to the "myopathy" group came from a sample for which the rest of the analysed fibres were unambiguously classified into their diagnostic group. As for the six fibres from the sample diagnosed as myopathy and added to the reference group by the model, four of these fibres came from the sample in which the other analysed cells were assigned to their category. The other two, however, came from a specimen in which they were the only fibres analysed. This may be indicative of the initial processes of disease.

Table 7. Classification matrix for matching fibres using multivariate discriminant analysis for 30% randomly selected fibre, which did not participate in the creation of the model. Abbreviations: D - dystrophy group; M - myopathy group; R - reference group.

	Group	**%**	**Assignment**			**Total**
			D	M	R	
Diagnosis	D	100%	4	0	0	4
	M	87%	0	13	2	15
	R	100%	0	0	16	16
	Total	94%	4	13	18	35

To test the validity, an inverse analysis was conducted using 30% random cases that were not considered during model creation (Table 7). The results obtained were also contrasted with the original diagnoses. The model achieved 94% correctness for assigning cases according to their diagnosis, with 100% for dystrophy and the reference group. For myopathy, it was 87% verifiability, as the two fibres according to the created model demonstrate the characteristics of the reference group. These are

fibres from the same sample, which cells were also assigned as a reference during model creation.

The SR-XRF method was also used to measure the elemental content of the connective tissue located between the fibres - the endomysium (DESY experiment). Measured areas of the endomysium were assigned to appropriate groups - dystrophy, myopathy and a reference group based on diagnosis. In the case of an area where more than one fibre was measured, the connective tissue was divided into fragments corresponding to the contact between each fibre. The Figure 26 shows an example of the areas for each group (D, M and R), together with an overlay of the microscopic area, measured during the experiment. The Figure 27 presents the summation spectrum obtained during the measurements for the sample.

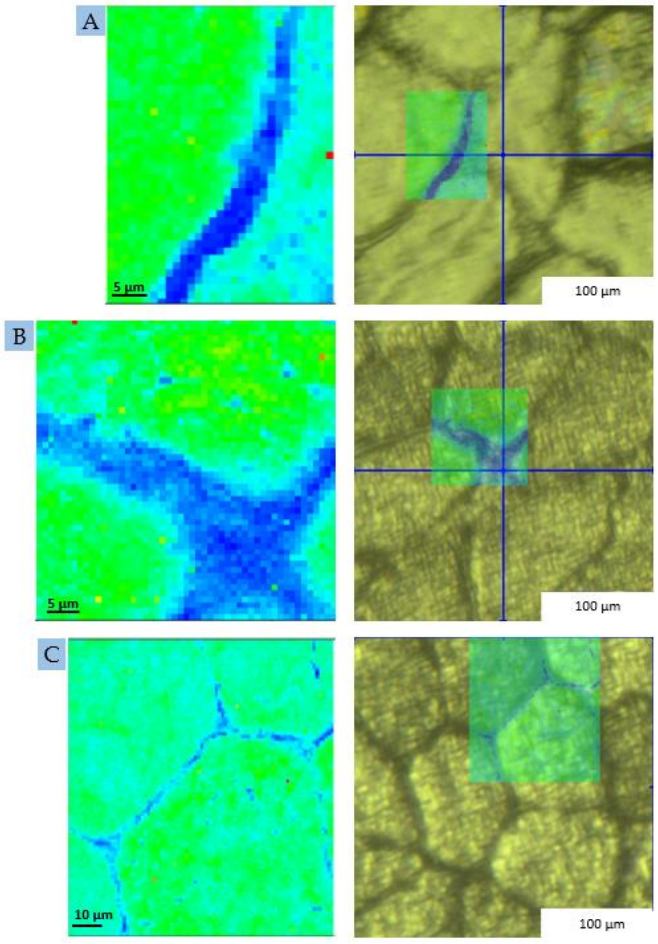

Figure 26. Elemental distribution maps with their overlap on the microscope image of the measured areas in the experiment performed on the P06 measurement line at the DESY synchrotron. A - area from sample D6, B - area from sample M3, C - area from sample R2.

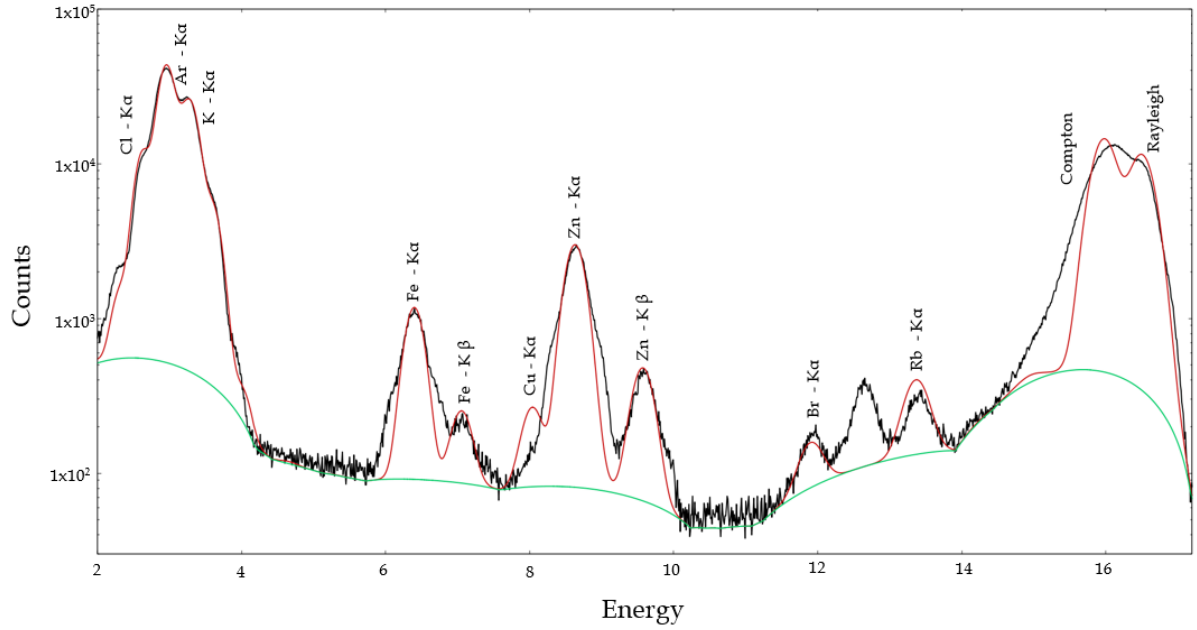

Figure 27. The spectrum of characteristic X-ray radiation of a selected fibre from the sample D1 from dystrophy group from measurements at the P06 beamline at PETRA III facility of the Deutsches Elektronen-Synchrotron DESY. Measurement geometry 90°/1° with energy 16.5 keV, beam size 300x300 nm² with step scan 1µm, measurement time 4 s per pixel. The black line shows the spectrum obtained from the measurements, while the red line shows the fit obtained using the PyMCA programme.

Comparative analysis carried out with the Kruskal-Wallis test showed that elements such as Fe, Cu, Br and Rb at least one of the groups showed statistically significant differences. In contrast, post-hoc tests showed that a statistically significant difference exists only for the Myopathy - reference pair for the element Br. The results of the tests are presented graphically using boxplots in Figure 28. For all the elements studied, it can be seen that the reference group shows a higher value of normalized radiation intensity in comparison with the other groups.

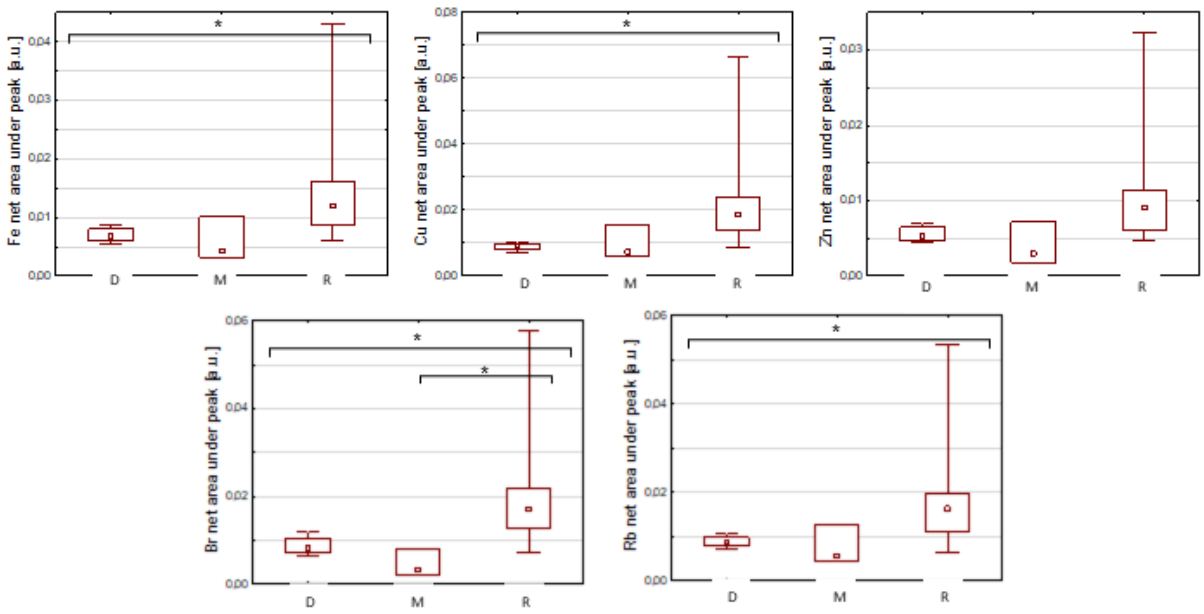

Figure 28. Comparison of the statistical significance of differences in the content of the analysed elements in endomysium between the test groups (median, ±0.25-0.75% percentile and min-max values). Abbreviations: *- statistically significant difference ($p < 0.05$) determined by Kruskal-Wallis test; D - dystrophy group (n=4); M - myopathy group (n=3); R - reference group (n=8).

Correlation analysis showed that all the studied elements have an extraordinarily strong correlation (correlation coefficient > 0.9) (Figure 29). All coefficients were found to be positive.

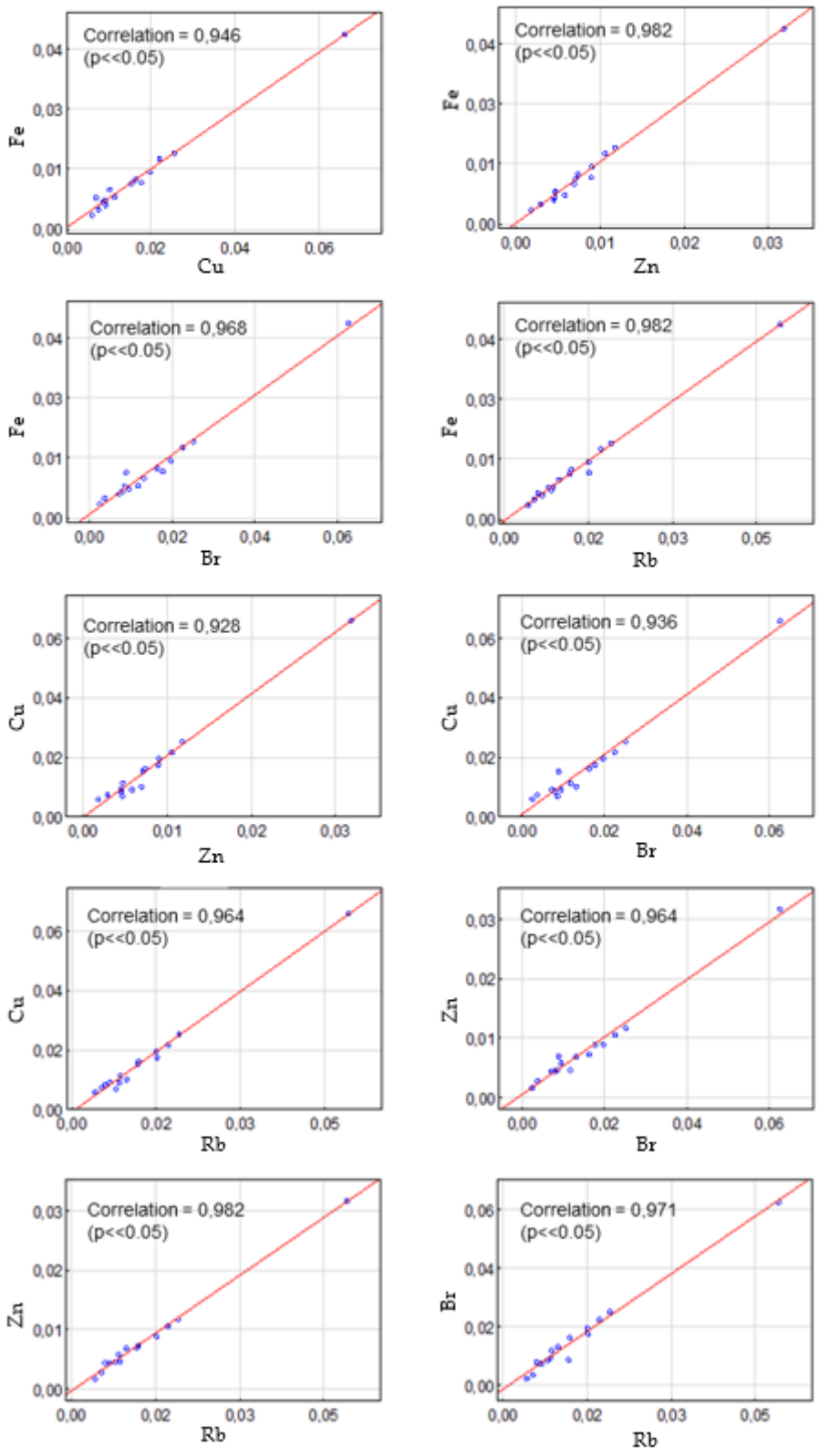

Figure 29. Correlation diagrams for the elements with the strongest relations for endomysium - correlation coefficient > 0.95. The axes show the value of the net area under the peak of a given element normalised to the value obtained for the Compton peak.

MDA analysis showed that the only element that impact the differentiation is Br (Partial Wilks' lambda = 0.21). Other elements were included in the model, but were not statistically significant due to the high value of the p-value ($p>0.05$). Because the data quantity is limited, all cases were considered when creating the model.

A discriminant function:

$$D1 = -6.131\,Fe - 4.749\,Cu + 5.308\,Zn + 13.85\,Br - 8.104\,Rb \quad (22)$$

$$D2 = -1.164\,Fe + 9.516\,Cu - 12.043\,Zn + 2.796\,Br + 1.195\,Rb \quad (23)$$

The functions are shown graphically in Figure 30.

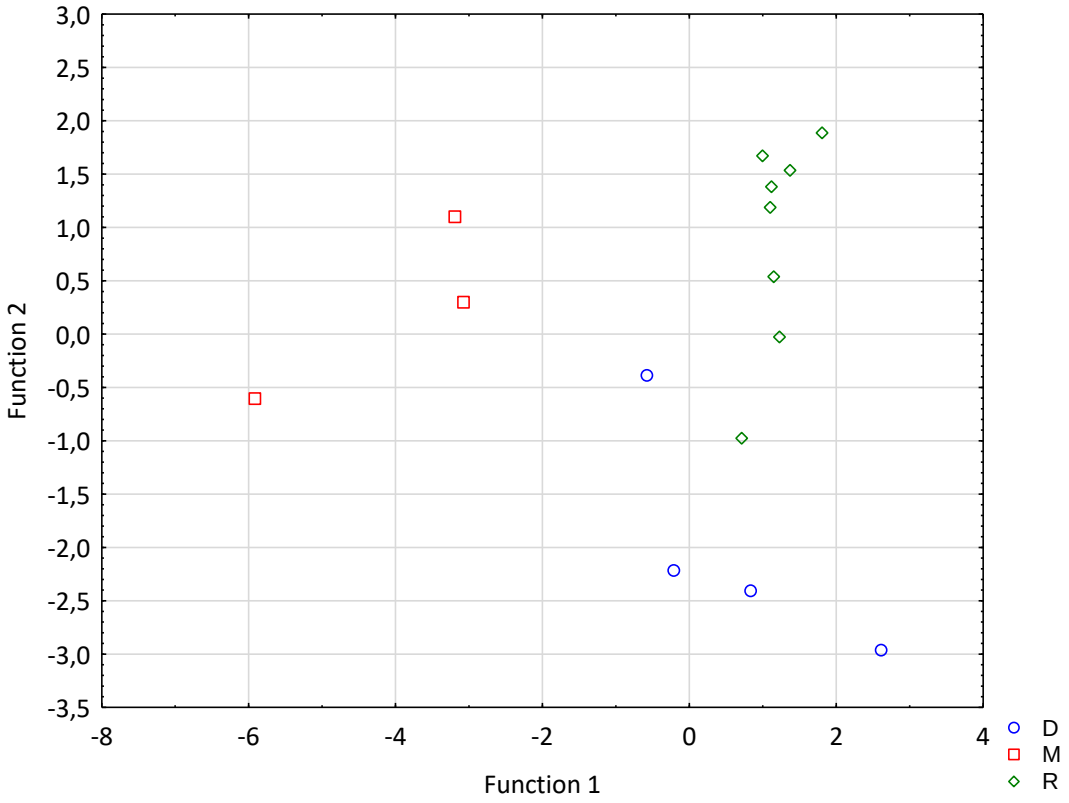

Figure 30. Graphical representation of configurations of discriminant function divided into groups represented by points in the discriminant variable system for endomysium analysis.

Reverse analysis was done to confirm the model (Table 8). The model showed 87% correctness when adding the studied cases to the previously diagnosed groups. It showed 100% efficiency to adding the endomysium associated to the myopathic group to this particular diagnosis.

Table 8. Classification matrix for matching fibres using multivariate discriminant analysis. Abbreviations: D - dystrophy group; M - myopathy group; R - reference group.

	Group	%	Assignment			Total
			D	M	R	
Diagnosis	D	75%	3	0	1	4
	M	100%	0	3	0	3
	R	87.5%	1	0	7	8
	Total	87%	4	3	8	15

Endomysium from one sample was qualified as the reference group with 60% probability, despite the diagnosis that indicated pathological changes. Histopathological examination clearly indicated changes indicative of dystrophy, including increased endomysium in the tissue, replacement of muscle tissue with adipose tissue, and numerous atrophic fibres. The reason for the obtained result may come from the examination of a small area of tissue, where the changes may be at their initials stages. Also, one endomysium previously diagnosed as the reference group was assigned by the model to the dystrophy group with a probability of 67%. The result of the diagnostic test determined that there are changes in the muscle tissue at the ultrastructural degree, but they are not distinct and cannot be unambiguously classified as pathological changes.

6.2. Biomolecular content of fibres

In order to conduct studies to verify possibly occurring changes in the content of biomolecules a whole membranes with tissue on them were measured (Nicolet iN10 experiment). Statistical analysis was carried out for all extracted spectra from randomly selected areas of the sample of established size. Figure 31 shows the IR spectra for each analysed group, indicating the ranges in which they occur and their mean. The Figure 32 presents microscopic images of the samples showing the total measured areas from each of the groups analysed - D, M and R, together with distribution maps for selected bands and bands ratio obtained with OMNIC software.

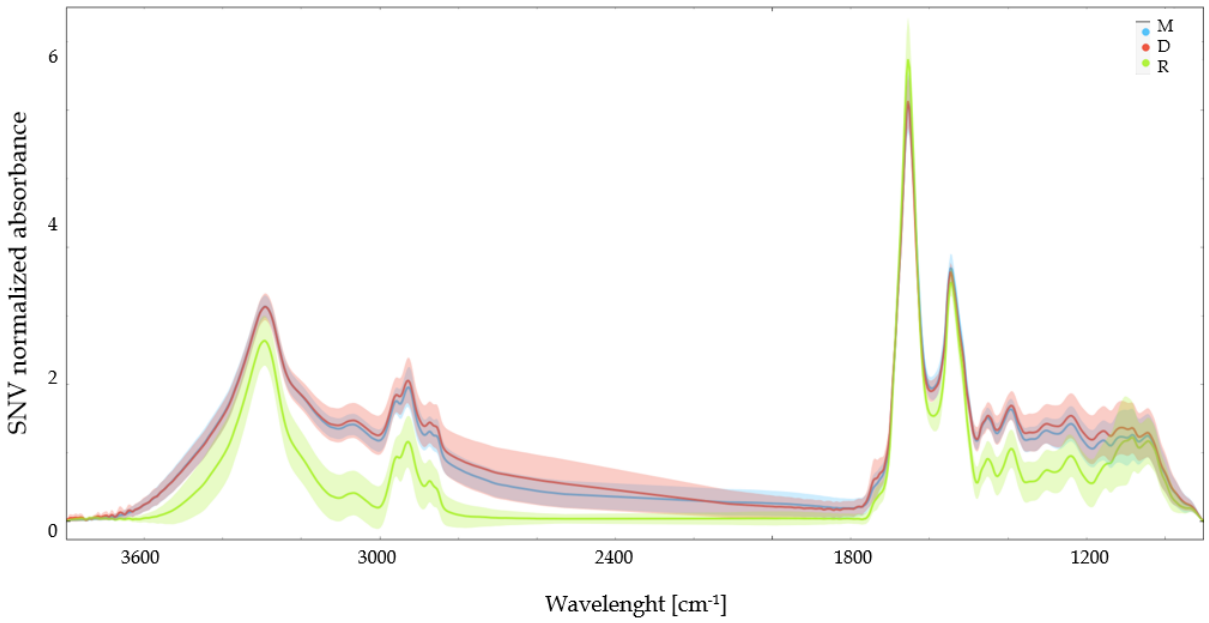

Figure 31. The image shows the spectra obtained for all samples analysed in the experiment with indication of the ranges in which they occur (light green - reference group, light red - dystrophy group, light blue - myopathy group) with indication of the mean spectrum (green - reference group, red - dystrophy group, blue - myopathy group).

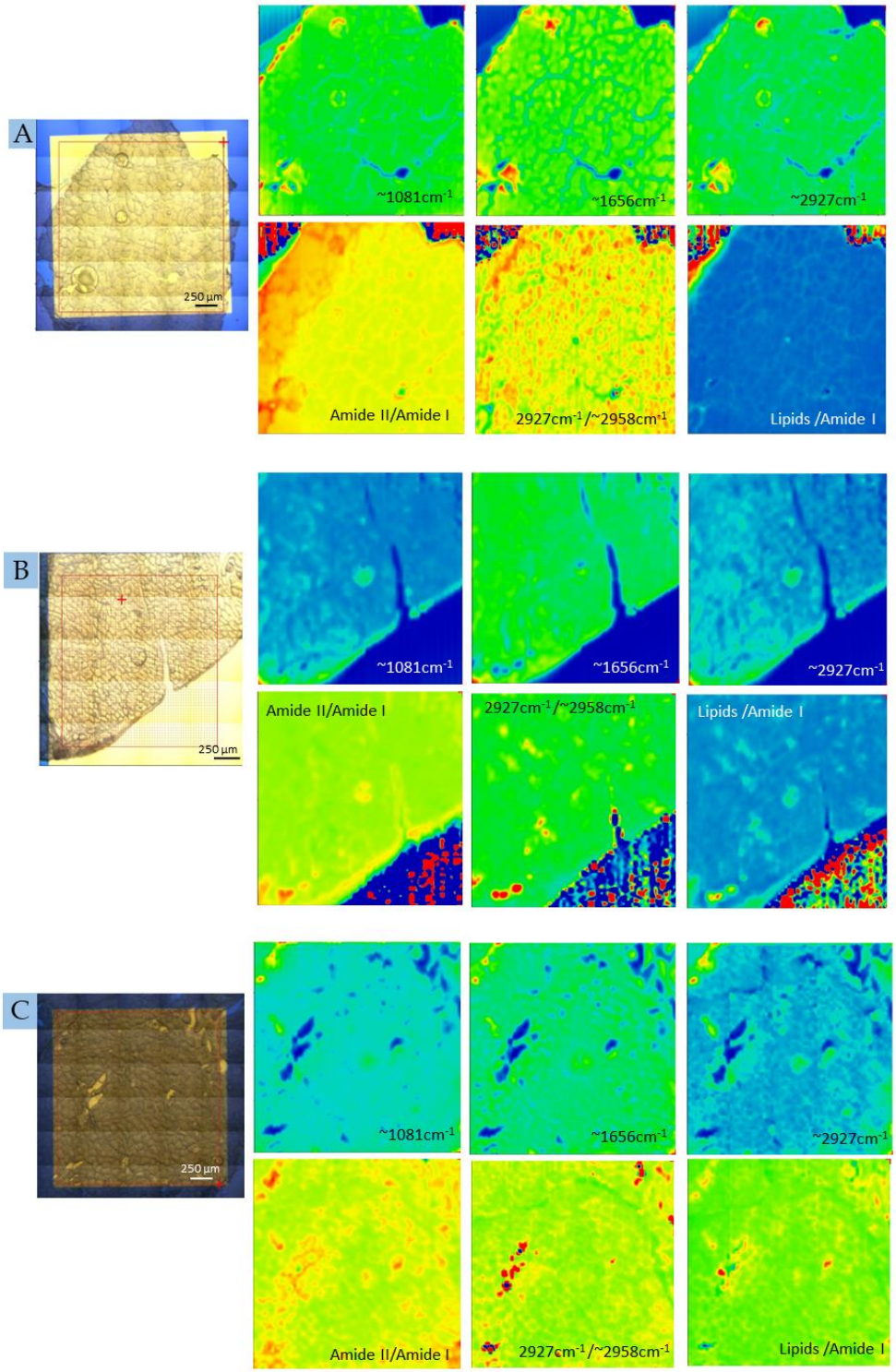

Figure 32. Microscopic image of the measured areas together with maps of the distribution of bands characteristic for the phosphate group (~1081cm-1), Amide I (~1656cm-1) and lipids (~2927cm-1) for A - dystrophy group D7 sample, B - myopathy group M6 sample and reference group R6 sample, respectively.

To check whether there are statistically significant differences in the analysed factors, the Kruskal-Wallis test was performed. For all three groups (D, M and R), all factors at least one group showed statistically significant differences. However, post-hoc tests showed that for the Dystrophy - Myopathy pair, factor P02 (~1081 cm^{-1} - PO^{2-} symmetric stretching) were considered statistically insignificant. A graphical representation of the test results is shown in Figure 33 for fingerprint bands and P07 (~1388 cm^{-1}) band in Figure 34 for protein bands and ester band and in Figure 35 for lipids bands.

For all the net values under the peak associated with lipids and proteins, a trend can be seen in which clearly lower values are observed for the samples diagnosed as the Reference Group. These changes are especially noticeable for factor P04 - cholesterol-related (~ 1155 cm^{-1}), P06 – related to Amide III (~ 1300 cm^{-1}), P07 (~ 1388 cm^{-1}), P08 - CH2 fatty bond (~ 1446 cm^{-1}), P09 - related to Amid II (~ 1546 cm^{-1}), P12 (~ 2855 cm^{-1}), P13 (~ 2873 cm^{-1}), P14 (~ 2927 cm^{-1}) and P15 (~ 2958 cm^{-1}) - related to symmetric and asymmetric CH_2 and CH_3 bonds, as well as P16 (~ 3065 cm^{-1}) and P17 (~ 3291 cm^{-1}) - related to Amides A and B. The most noticeable changes related to the characteristic bands for nucleic acids can be observed for factor P05 (~ 1237 cm^{-1}) - associated with symmetric band of PO^{2-}.

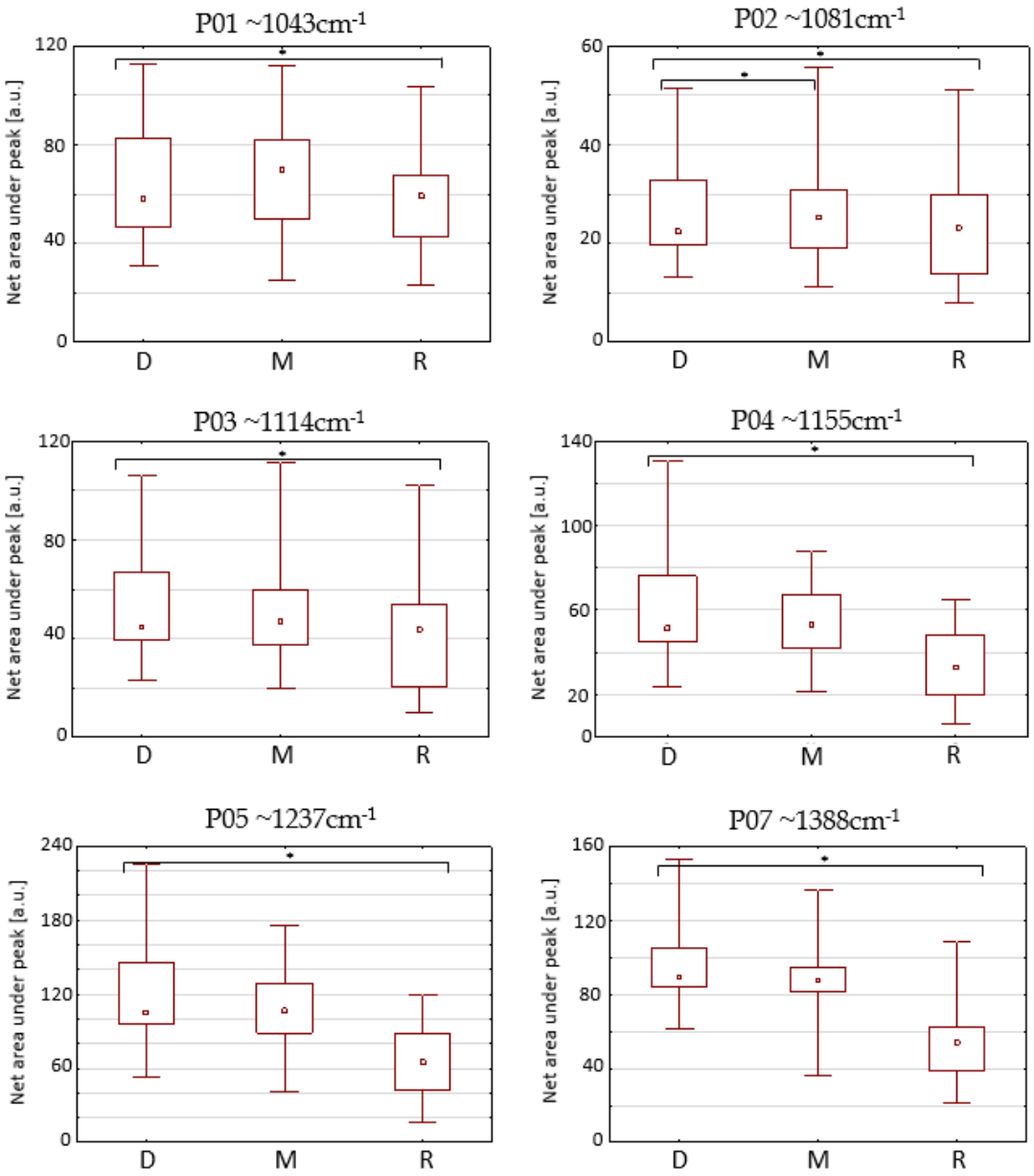

Figure 33. Comparison of the statistical significance of differences in the content of the analysed biomolecules for measurement area (fingerprint bands - P01, P02, P03, P04, P05 and band P07) in muscle tissues between the test groups (median, ±0.25-0.75% percentile and min-max values). Abbreviations: *- statistically significant difference ($p < 0.05$) determined by Kruskal-Wallis test; D - dystrophy group (n=8); M - myopathy group (n=10); R - reference group (n=5).

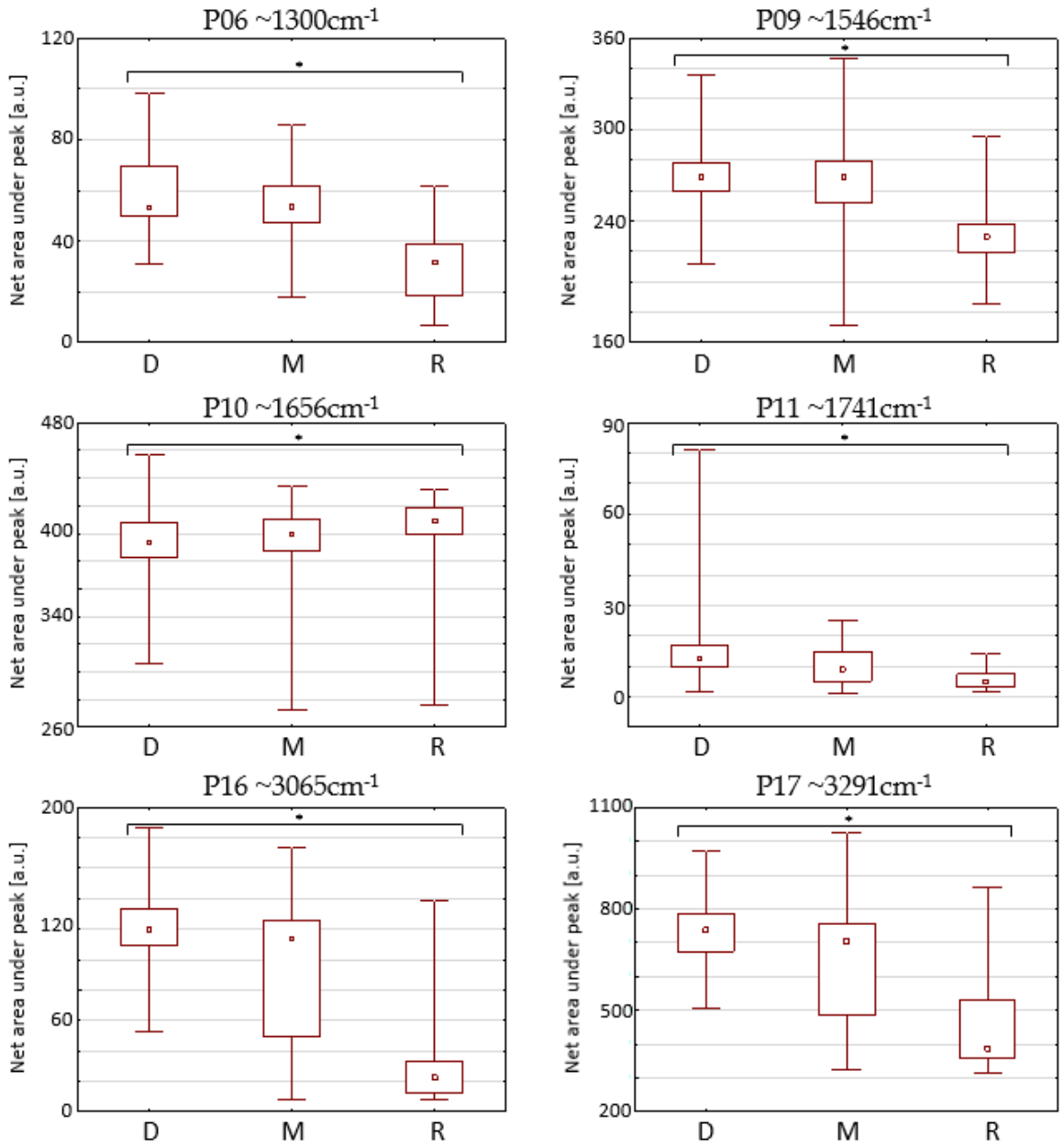

Figure 34. Comparison of the statistical significance of differences in the content of the analysed biomolecules for measurement are (protein bands - P06, P09, P10, P16, P17 and ester band P11) in muscle tissues between the test groups (median, ±0.25-0.75% percentile and min-max values). Abbreviations: *- statistically significant difference ($p < 0.05$) determined by Kruskal-Wallis test; D - dystrophy group (n=8); M - myopathy group (n=10); R - reference group (n=5).

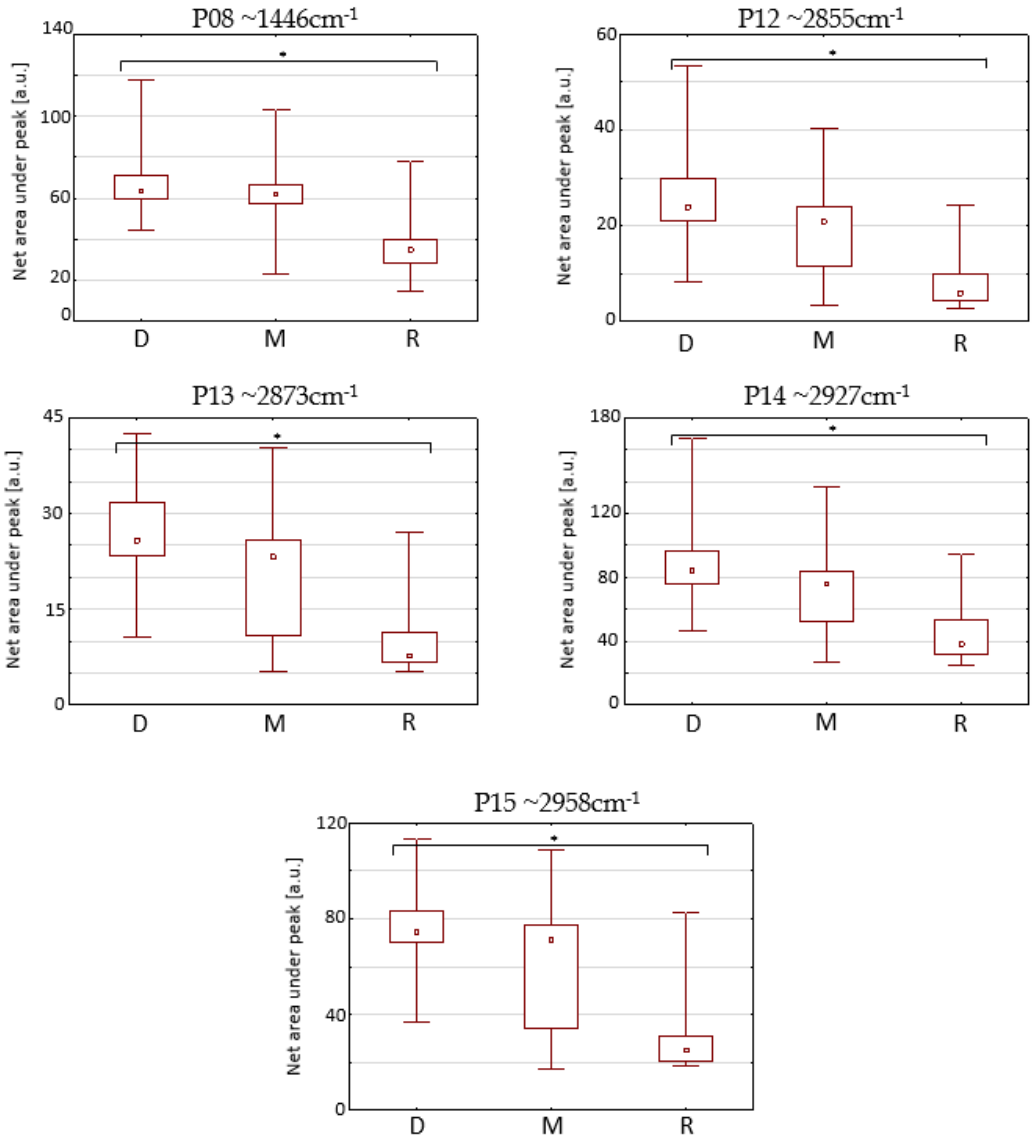

Figure 35. Comparison of the statistical significance of differences in the content of the analysed biomolecules for measurement area (lipids bands - P08, P12, P13, P14, P15) in muscle tissues between the test groups (median, ±0.25-0.75% percentile and min-max values). Abbreviations: *- statistically significant difference ($p < 0.05$) determined by Kruskal-Wallis test; D - dystrophy group (n=8); M - myopathy group (n=10); R - reference group (n=5).

To test whether there was a statistically significant difference between the band ratios, a Kruskal-Wallis test was carried out. The results of the test showed statistically significant differences between all groups, and post-hoc tests showed statistically significant differences between all pairs of groups for all band ratios analysed. A graphical representation of the test results is presented in Figure 36. Visible changes in the difference in ratios can be seen for ~1237 cm^{-1}/~1656 cm^{-1}, ~1388 cm^{-1}/~1656 cm^{-1},

~1546 cm^{-1}/~1656 cm^{-1} and for Lipids/~1565 cm^{-1} where the band ratio is higher for dystrophy, and slightly higher for myopathy compared to the reference group. In contrast, the opposite situation can be seen for ~2927 cm^{-1}/2958 cm^{-1}, where the band ratio is higher for the reference group.

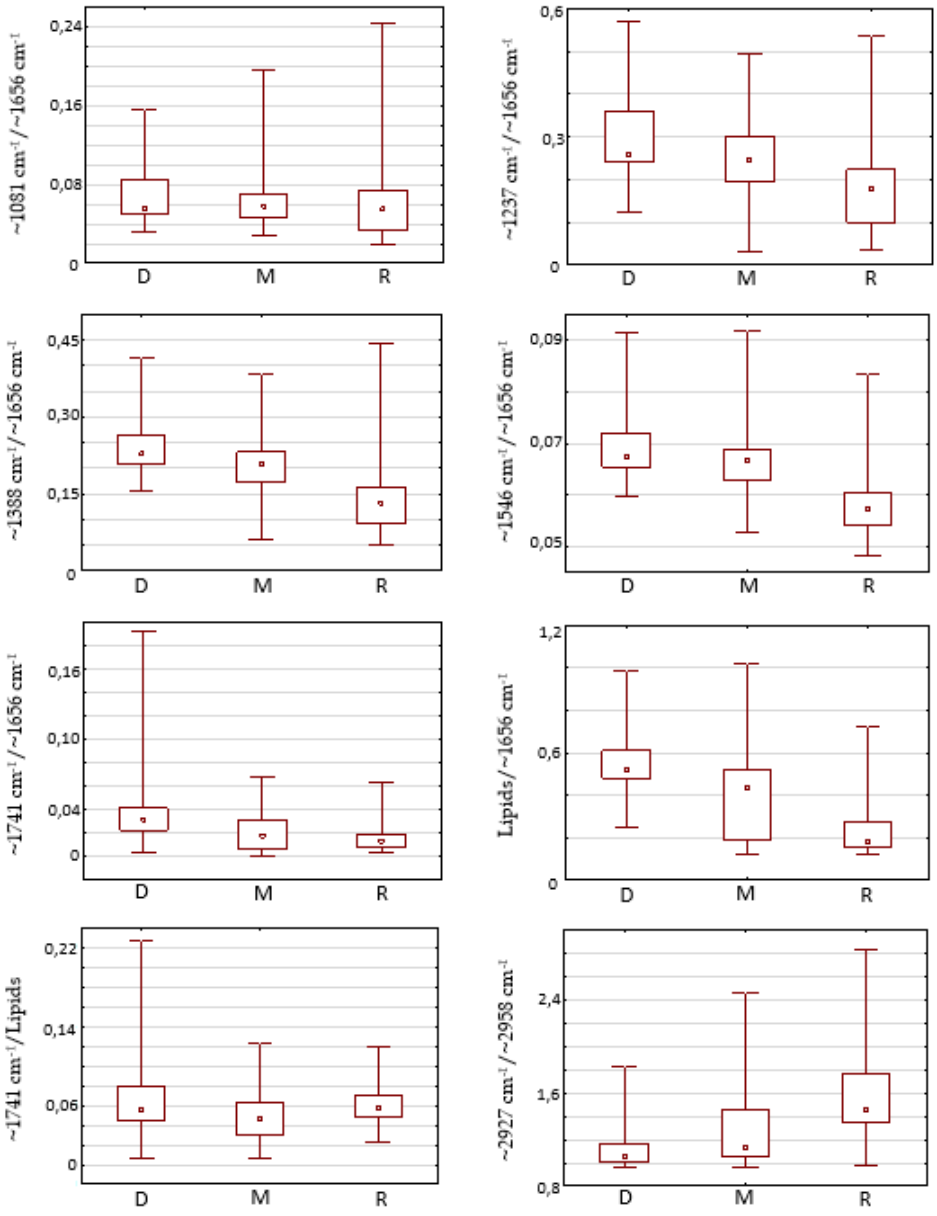

Figure 36. Comparison of the statistical significance of differences in the content of the analysed band ratios for measurement area in muscle tissues between the test groups (median, ±0.25-0.75% percentile and min-max values). Abbreviations: D - dystrophy group (n=8); M - myopathy group (n=10); R - reference group (n=5). The y-axes represent the ratio of the values of the net areas under the peak for a given band.

In order to verify which of the 17 analysed peaks or massifs have the greatest impact on the separation, MDA analysis was performed. Based on the partial Wilks lambda - Table 9, it was found that peaks such as P01 (~1043 cm^{-1}) – related to COH deformation bond, P07 (~1388 cm^{-1}) – related to COO- symmetric stretching bond, P13 (~2873 cm^{-1}) – related to CH_3 symmetric stretching bond, P16 (~3065 cm^{-1}) – related to Amide B, have the greatest effect on separation, while peak P05 (~1237 cm^{-1}) – related to PO^{2-} symmetric stretching bond, was outside the model.

Table 9. Partial Wilks' lambda value for selected areas from the samples.

Peak No.	**Wavenumber (cm^{-1})**	**Partial Wilks' lambda**
P01	~1043	0.903
P02	~1081	0.913
P03	~1114	0.915
P04	~1155	0.927
P06	~1300	0.949
P07	~1388	0.907
P08	~1446	0.973
P09	~1546	0.968
P10	~1656	0.992
P11	~1741	0.994
P12	~2855	0.956
P13	~2873	0.898
P14	~2927	0.943
P15	~2958	0.993
P16	~3065	0.905
P17	~3291	0.994

The discriminant functions obtained as a result of creating the model are presented in the equations below.

$$D1 = 1.115\,P01 - 4.670\,P02 + 3.773\,P03 + 0.534\,P04 - 1.400\,P06 + 1.982\,P07 - 0.567\,P08 - 0.450\,P09 - 0.004\,P10 - 0.252\,P11 + 2.253\,P12 - 3.482\,P13 + 0.006\,P14 + 0.386\,P15 + 1.550\,P16 - 0.289\,P17 \quad (24)$$

$$D2 = 5.583\,P01 - 10.729\,P02 + 9.093\,P03 - 5.576\,P04 + 5.613\,P06 - 6.092\,P07 + 2.229\,P08 + 0.736\,P09 - 0.436\,P10 - 0.058\,P11 + 1.266\,P12 - 6.451\,P13 + 4.545\,P14 - 1.658\,P15 + 1.984\,P16 + 0.199\,P17 \quad (25)$$

The graphical representation of the distribution in the space of discriminant functions is presented in Figure 37.

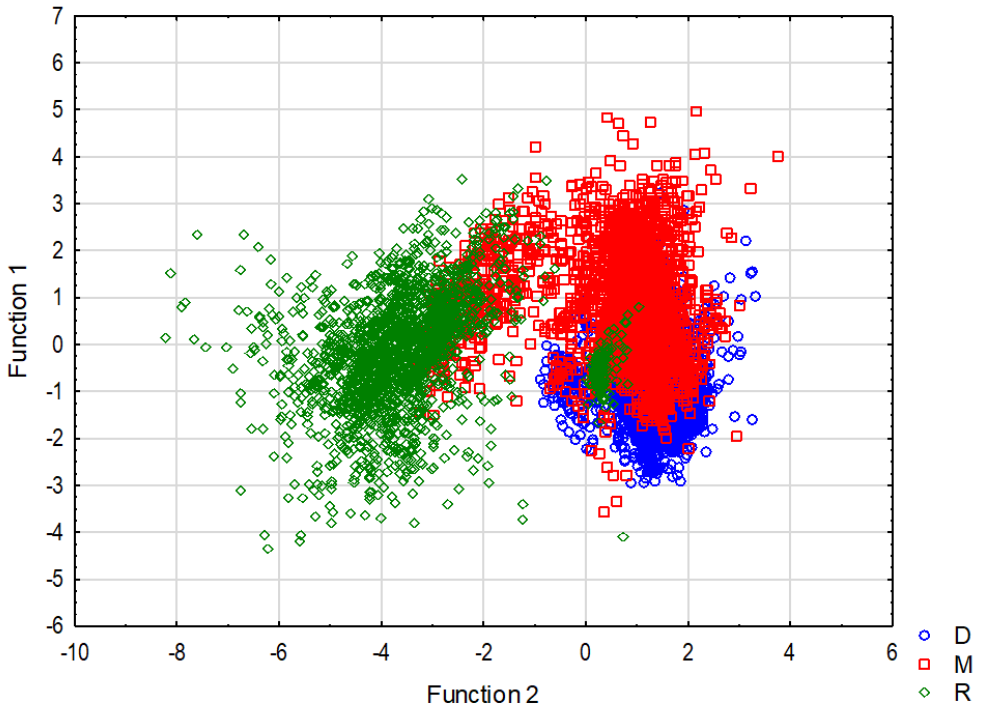

Figure 37. Graphical representation of configurations of discriminant function divided into groups represented by points in the discriminant variable system selected areas from the samples.

To check the validity of the model, the reverse analysis was conducted - Table 10. The model revealed 80% agreement in the distribution of data relative to diagnoses, with the highest 90% for the reference group.

Table 10. Classification matrix for muscle tissues using multivariate discriminant analysis. Abbreviations: D - dystrophy group; M - myopathy group; R - reference group.

	Group	%	Assignment			Total
			D	M	R	
Diagnosis	D	81%	2941	710	0	3651
	M	73%	722	2500	223	3445
	R	90%	151	56	1818	2025
	Total	80%	3814	3266	2041	9121

For the obtained results, it is easy to see discrepancies when matching the samples from the myopathy group to the dystrophy group, and vice versa. This may be due to the fact that both groups have similar symptoms, i.e. atrophy of muscle fibres - a loss of protein, replaced by lipid tissue and hypertrophic fibres - growth protein. An interesting observation is the assignment of data from the myopathy group to the control group. These are mostly data derived from one sample in which the diagnostic description states that the pathological changes are moderately intense. There are also differences in assignment for the reference group sample, which the model assigns as dystrophy and myopathy. It is one sample which showed slight characteristic pathological changes of low intensity during the pathological examination, but it was not possible to clearly identify the cause.

Since Kruskal-Wallis analysis showed significant differences in the biomolecular composition of the areas of sample diagnosed as the reference group and those affected by pathological changes, it was decided to conduct an experiment (SR-FTIR experiment) to study the differences between the connective tissue in the fibres of the different groups.

Figure 38 presents microscopic images of the samples showing measured areas from each of the groups analysed - D, M and R, together with distribution maps for selected bands and bands ratio obtained with OMNIC software. Figure 39 shows the IR spectra for each analysed group, indicating the ranges in which they occur and their mean value.

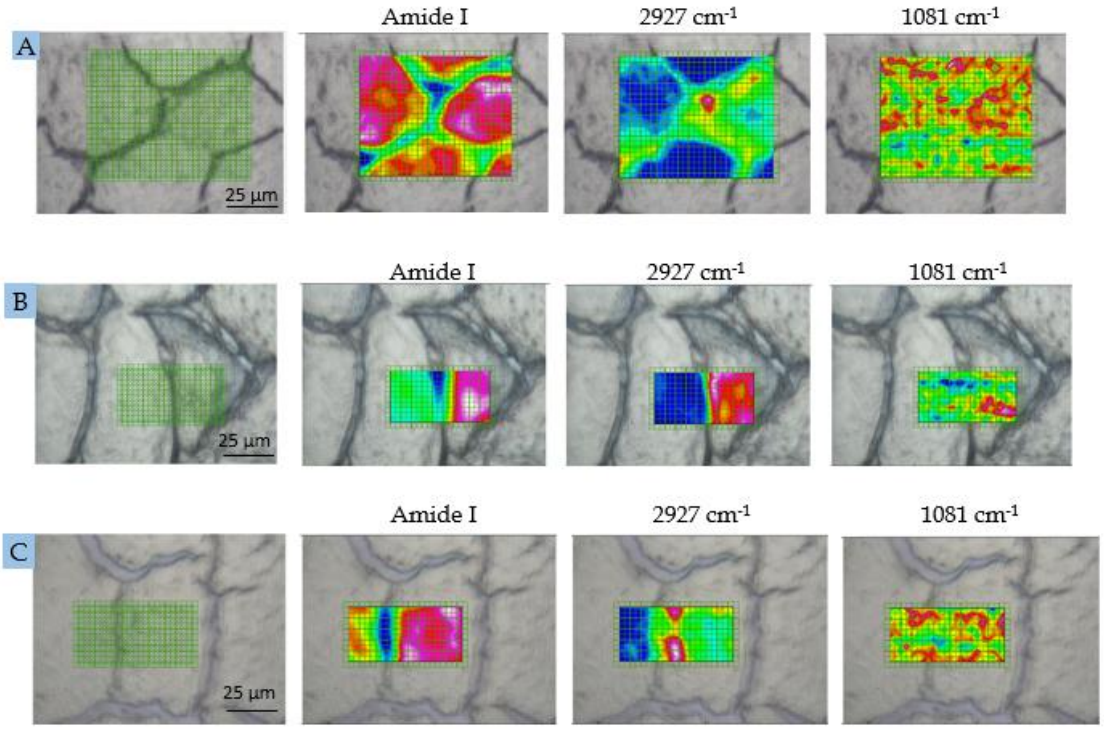

Figure 38. Microscopic image of the measured areas of endomysium together with maps of the distribution of bands characteristic for the phosphate group (~1081cm-1), Amide I (~1656cm-1) and lipids (~2927cm-1) for A - dystrophy group D7 sample, B - myopathy group M6 sample and reference group R6 sample, respectively.

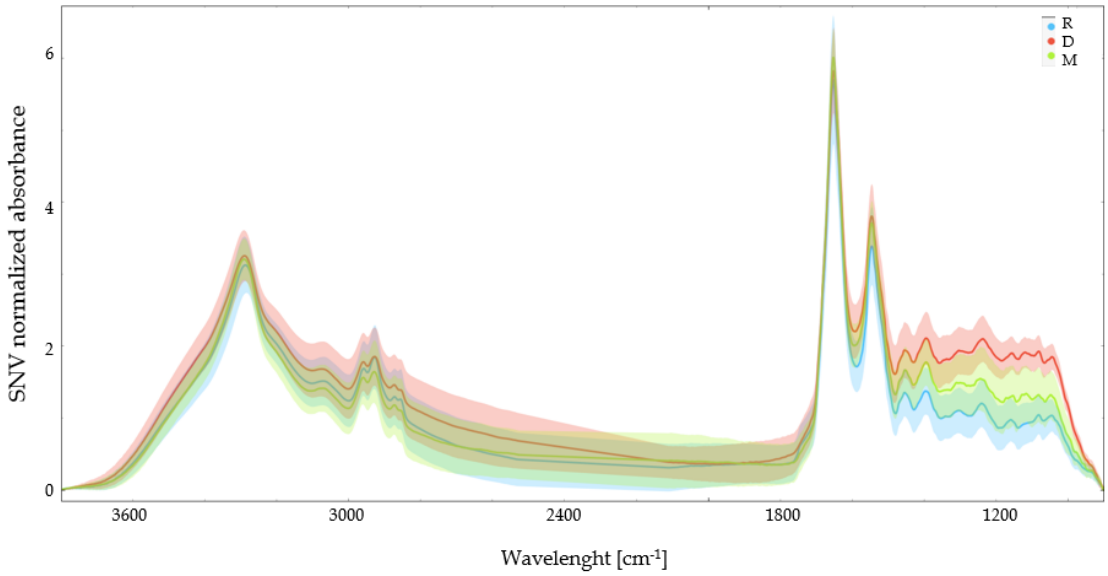

Figure 39. The image shows the spectra obtained for all endomysium analysed in the experiment with indication of the ranges in which they occur (light green - reference group, light red - dystrophy group, light blue - myopathy group) with indication of the mean spectrum (green - reference group, red - dystrophy group, blue - myopathy group).

The Kruskal-Wallis test performed on endomysium showed a significant increase in content for the dystrophy group for peaks such as P02 (~1081 cm^{-1}), P03 (~1114 cm^{-1}), P04 (~1155 cm^{-1}) and P05 (1237 cm^{-1}), for the myopathy group for peak P09 (~1546 cm^{-1}), and an increase for both the myopathy and dystrophy groups for peaks P06 (~1300 cm^{-1}), P07 (~1388 cm^{-1}) and P08 (~1446 cm^{-1}). A slight decrease in content for the dystrophy group was observed for peak P10 (~1656 cm^{-1}). The remaining factors remain at the same level of biomolecule content. A graphical representation of the test results is shown in Figure 40 for fingerprint bands and P07 (~1388 cm^{-1}) band in Figure 41 for protein bands and ester band and in Figure 42 for lipids bands.

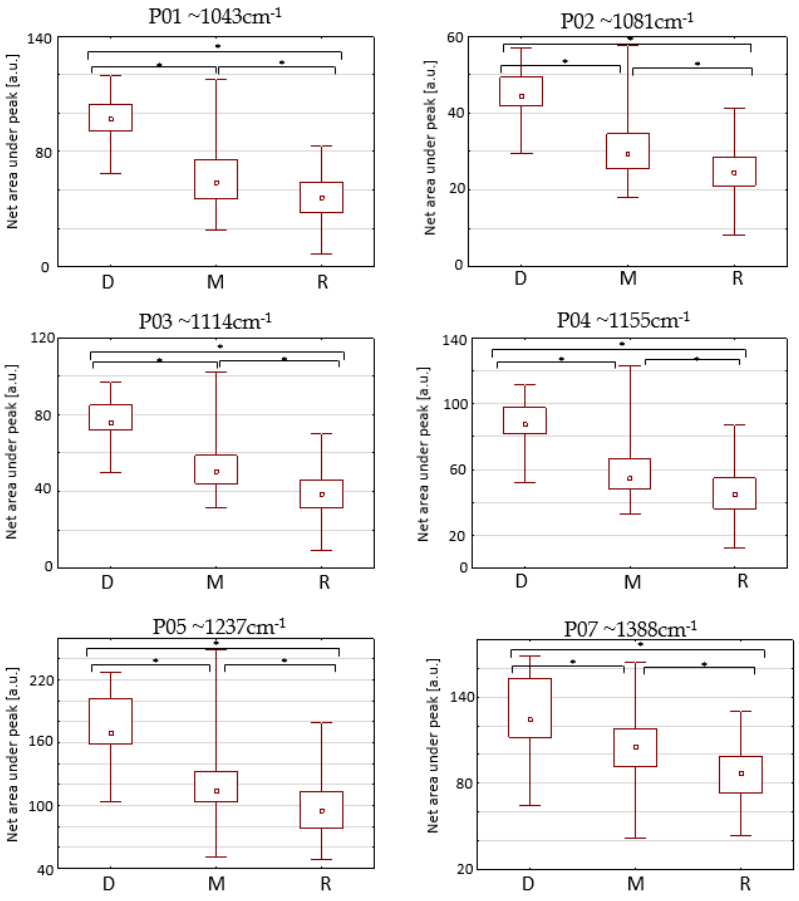

Figure 40. Comparison of the statistical significance of differences in the content of the analysed biomolecules for endomysium (fingerprint bands - P01, P02, P03, P04, P05 and band P07) in muscle tissues between the test groups (median, ±0.25-0.75% percentile and min-max values). Abbreviations: *- statistically significant difference ($p < 0.05$) determined by Kruskal-Wallis test; D - dystrophy group (n=3); M - myopathy group (n=2); R - reference group (n=2).

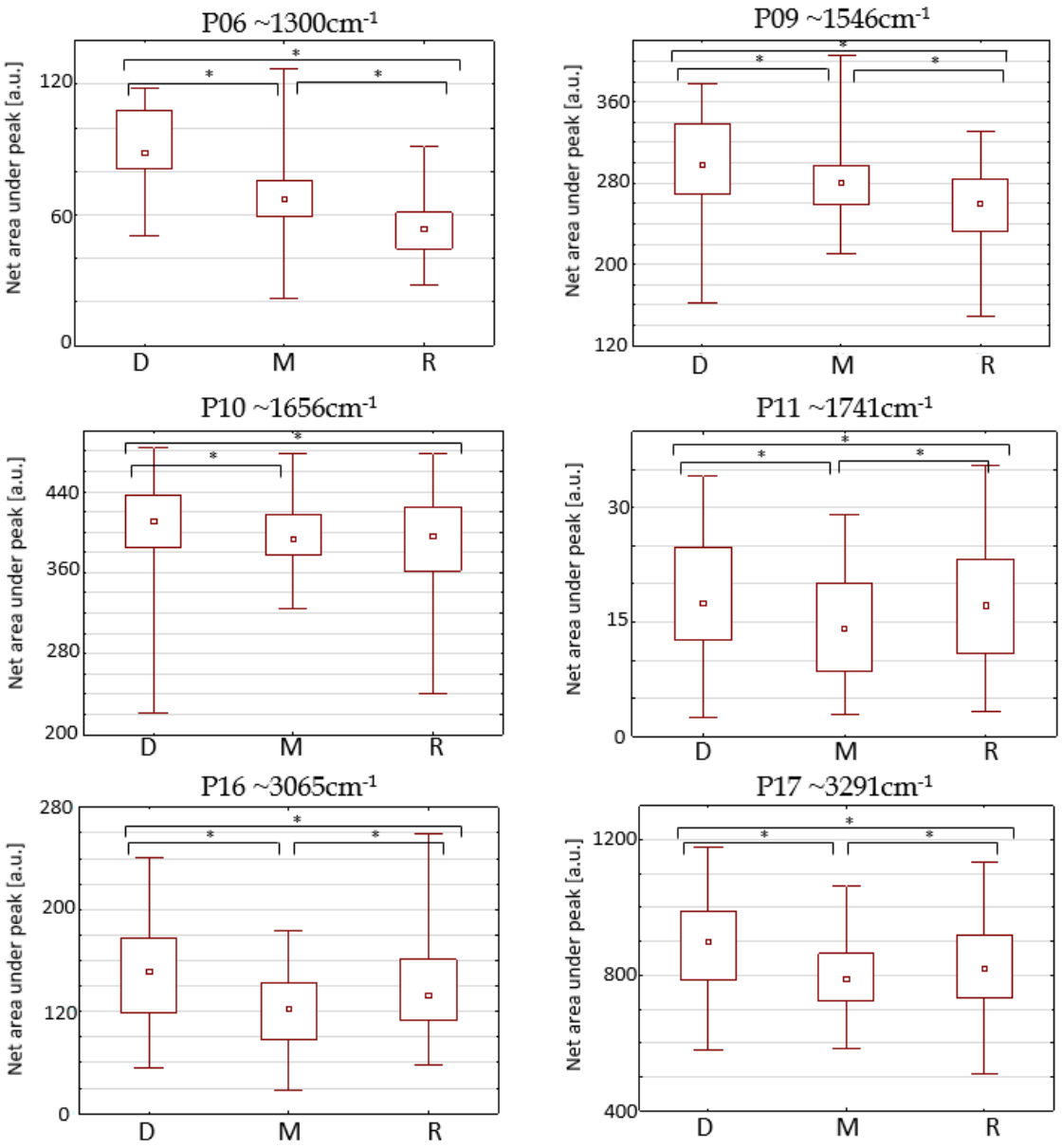

Figure 41. Comparison of the statistical significance of differences in the content of the analysed biomolecules for endomysium (protein bands - P06, P09, P10, P16, P17 and ester band P11) in muscle tissues between the test groups (median, ±0.25-0.75% percentile and min-max values). Abbreviations: *- statistically significant difference ($p < 0.05$) determined by Kruskal-Wallis test; D - dystrophy group (n=3); M - myopathy group (n=2); R - reference group (n=2).

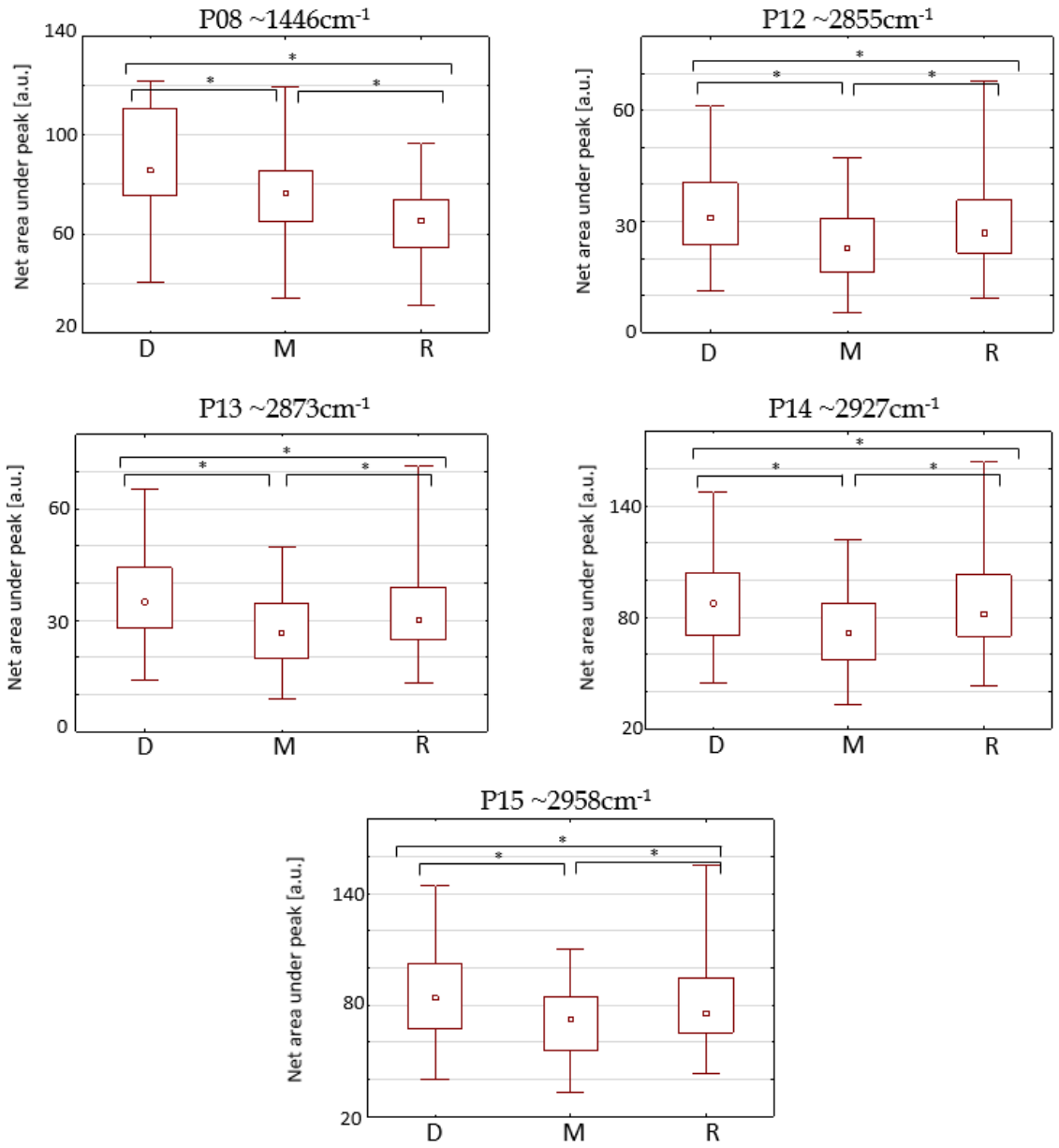

Figure 42. Comparison of the statistical significance of differences in the content of the analysed biomolecules for endomysium (lipids bands - P08, P12, P13, P14, P15) in muscle tissues between the test groups (median, ±0.25-0.75% percentile and min-max values). Abbreviations: *- statistically significant difference ($p < 0.05$) determined by Kruskal-Wallis test; D - dystrophy group (n=3); M - myopathy group (n=2); R - reference group (n=2).

The Kruskal-Wallis test was also conducted to check for statistically significant differences between the band ratios analysed. The results showed no statistically significant differences for the band ratio ~1741 cm^{-1}/Lipids, as well as between the Dystrophy - Myopathy groups for the ratio of bands, responsible for lipid saturation levels (~2927 cm^{-1}/2958 cm^{-1}). The test results are presented graphically in Fig. The

greatest differences in band ratios can be seen for ratios of ~1081 cm^{-1}/1656 cm^{-1}, ~1237 cm^{-1}/~1656 cm^{-1}, ~1388 cm^{-1}/~1565 cm^{-1} and ~1546 cm^{-1}/1656 cm^{-1}, for which lower values for the reference group can clearly be seen.

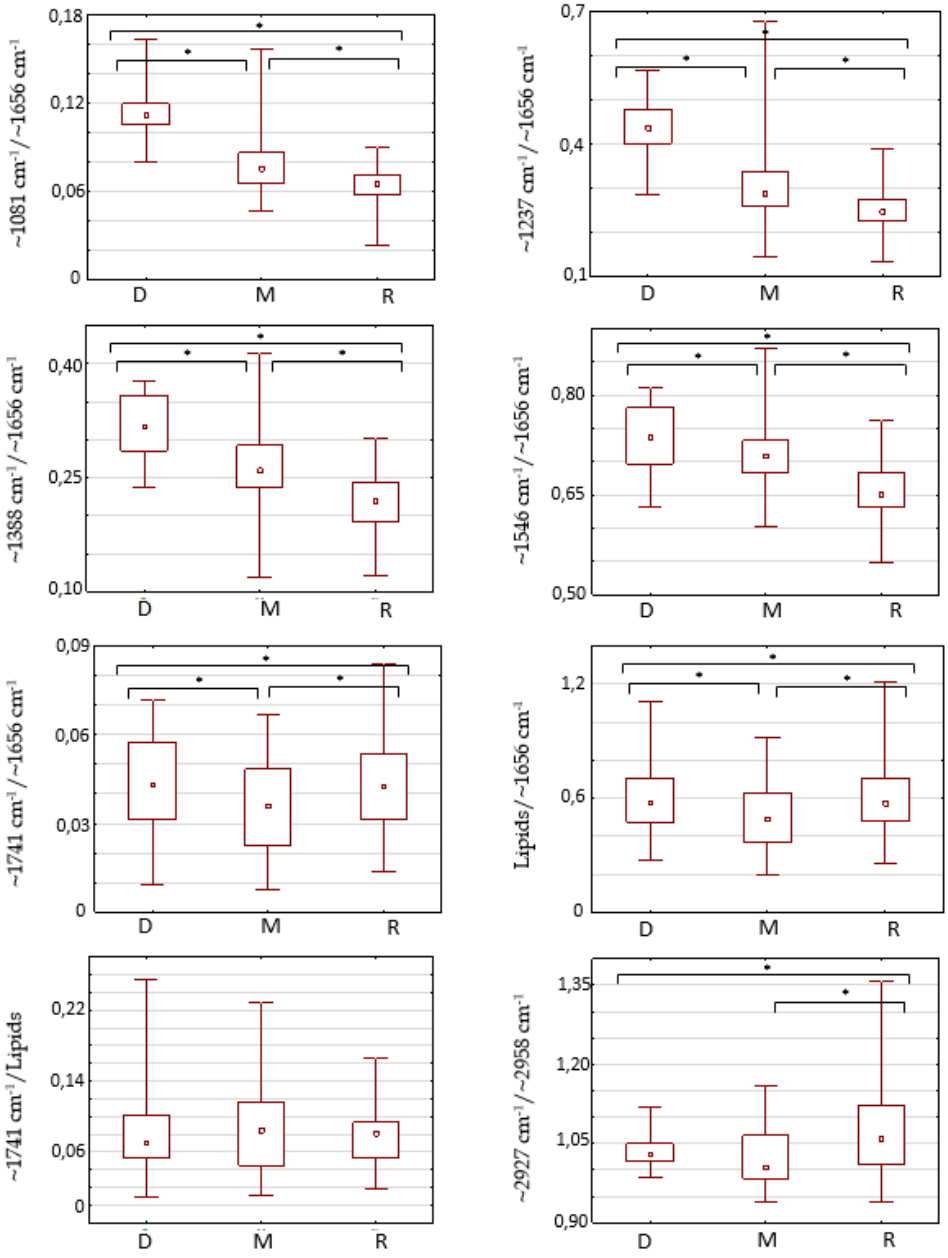

Figure 43. Comparison of the statistical significance of differences in the content of the analysed band ratios for endomysium in muscle tissues between the test groups (median, ±0.25-0.75% percentile and min-max values). Abbreviations: *- statistically significant difference ($p < 0.05$) determined by Kruskal-Wallis test; D - dystrophy group (n=3); M - myopathy group (n=2); R - reference group (n=2). The y-axes represent the ratio of the values of the net areas under the peak for a given band.

An MDA analysis was carried out to verify which of the 17 factors has the greatest impact on the separation of connective tissue. Based on the results obtained for the partial Wilks lambda -

Table 11, peaks such as P01 (~1043 cm), P07 (~1388 cm^{-1}), P10 (~1656 cm^{-1}) and P14 (~2927 cm^{-1}) were found to have the greatest impact on distribution. Peak 13 (~2873 cm^{-1}) was not taken into account during the model development.

Table 11. Partial Wilks' lambda value for biomolecular endomysium analysis.

Peak No.	Wavenumber (cm^{-1})	Partial Wilks' lambda
P01	~1043	0.823
P02	~1081	0.866
P03	~1114	0.924
P04	~1155	0.966
P05	~1237	0.931
P06	~1300	0.883
P07	~1388	0.727
P08	~1446	0.965
P09	~1546	0.959
P10	~1656	0.809
P11	~1741	0.858
P12	~2855	0.898
P14	~2927	0.709
P15	~2958	0.964
P16	~3065	0.976
P17	~3291	0.913

The discriminant functions created in the model are presented in the equations below.

$$D1 = -2.922\,P01 + 0.344\,P02 + 2.102\,P03 - 1.685\,P04 + 3.621\,P05 - 4.167\,P06 + 4.932\,P07 - 1.600\,P08 - 0.747\,P09 + 1.213\,P10 - 0.370\,P11 + 2.517\,P12 - 3.962\,P14 - 0.074\,P15 + 0.307\,P16 + 0.692\,P17 \quad (26)$$

$$D2 = 4.186\,P01 - 7.468\,P02 + 6.402\,P03 - 2.125\,P04 - 0.104\,P05 + 1.345\,P06 - 0.476\,P07 - 0.017\,P08 - 0.288\,P09 + 0.968\,P10 - 0.732\,P11 - 0.824\,P12 - 0.203\,P14 - 1.503\,P15 + 0.789\,P16 + 0.898\,P17 \quad (27)$$

The graphical representation of the distribution in the space of discriminant functions is presented in Figure 44.

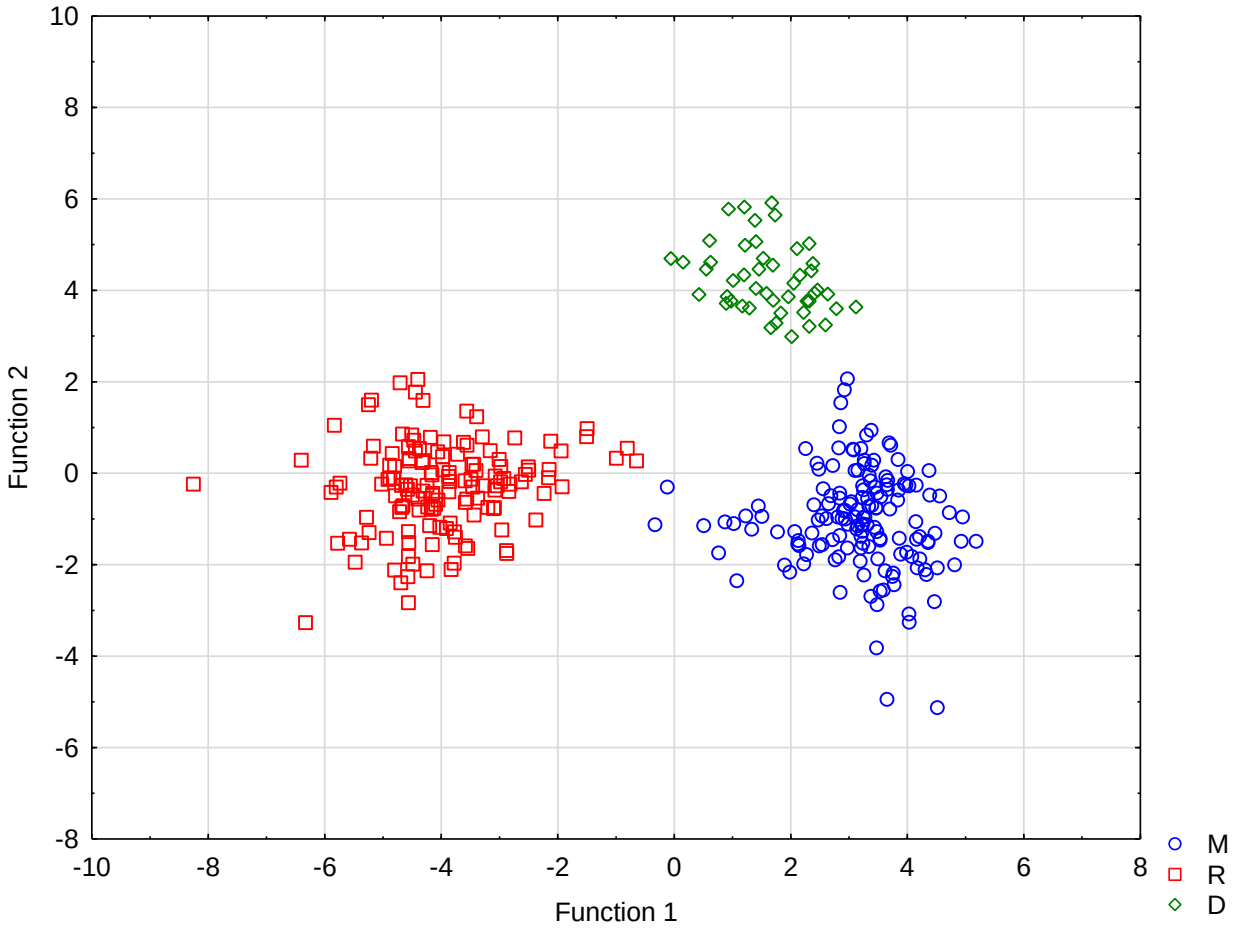

Figure 44. Graphical representation of configurations of discriminant function divided into groups represented by points in the discriminant variable system for biomolecular endomysium analysis.

A reverse analysis was performed to verify the validity of the model - Table 12. The model demonstrated 99.7% correctness in relation to the diagnoses.

Table 12. Classification matrix for muscle tissues using multivariate discriminant analysis. Abbreviations: D - dystrophy group; M - myopathy group; R - reference group.

	Group	%	Assignment			Total
			D	M	R	
Diagnosis	D	100%	47	0	0	47
	M	99%	1	151	0	152
	R	100%	0	0	141	141
	Total	99.7%	48	151	141	340

FTIR measurements were also carried out in order to check whether there are differences in the biomolecular composition in the samples before and after the measurement with the SR-XRF method, causing possible radiation damage.

To check whether there are statistically significant differences between the two study groups - before the measurements with the SR-XRF method (B) and after the measurements with the SR-XRF method (A) (the mean spectra are shown on the Figure 45), the U Mann-Whitney test was performed (Nicolet 8700 experiment). A graphical representation of the test results is shown in Figure 46 for fingerprint bands and P07 (~1388 cm^{-1}) band in Figure 47 for protein bands and ester band and in Figure 48 for lipids bands. The analysis showed that for all factors tested for both groups, the results were statistically significant.

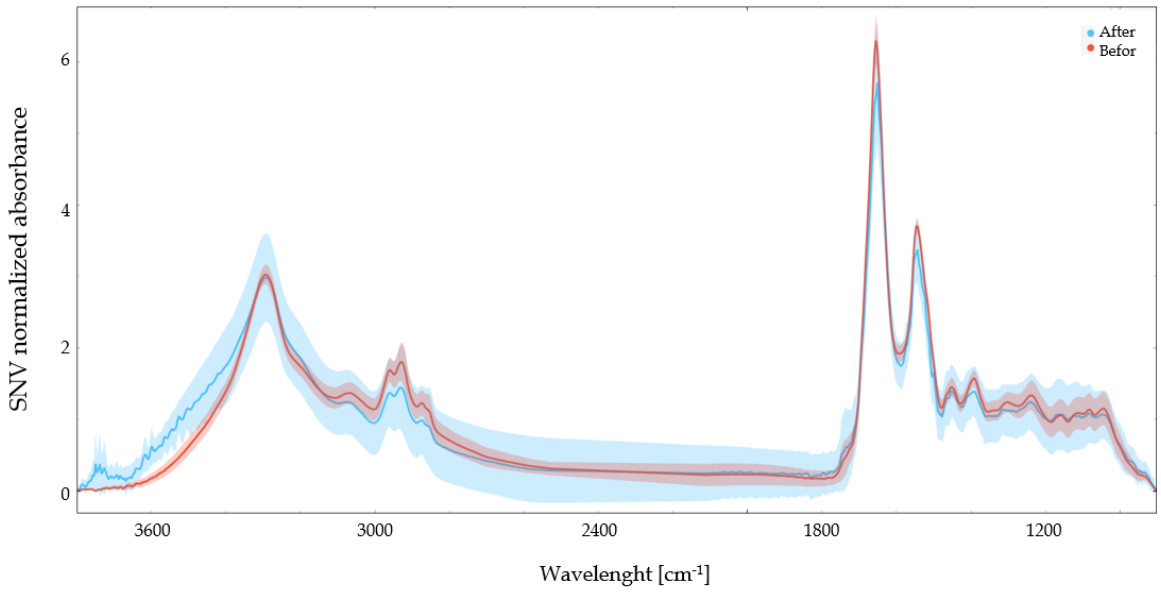

Figure 45. The image shows the spectra obtained for all samples analysed in the experiment with indication of the ranges in which they occur (light red – samples area measured before SR-XRF experiment, light blue - samples area measured after SR-XRF experiment) with indication of the mean spectrum (red – samples area measured before SR-XRF experiment, blue - samples area measured after SR-XRF experiment).

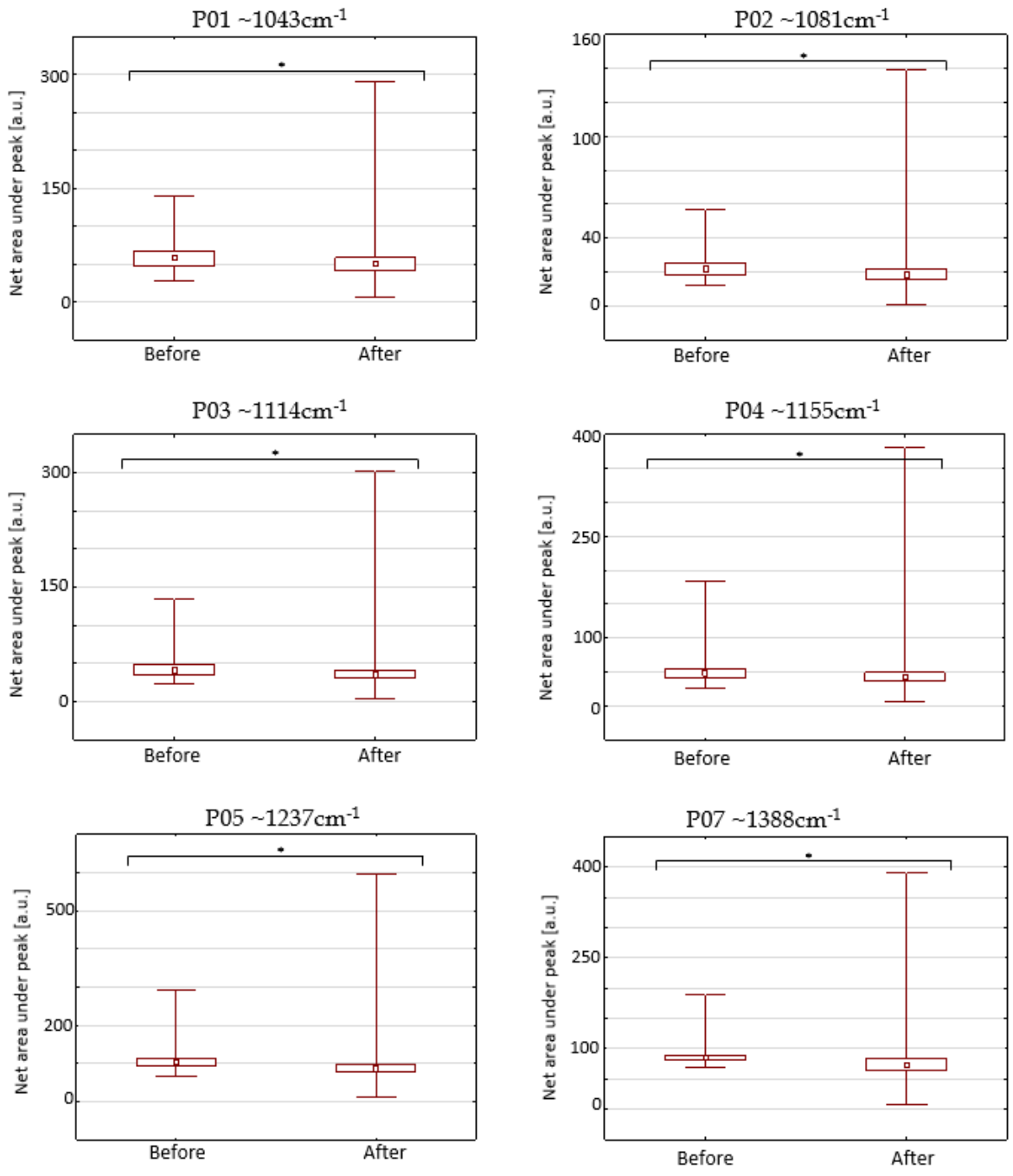

Figure 46. Comparison of the statistical significance of differences in the content of the analysed biomolecules in a comparative analysis of areas that may have been exposed to radiation damage (fingerprint bands - P01, P02, P03, P04, P05 and band P07) in muscle tissues between the test groups (median, ±0.25-0.75% percentile and min-max values). Abbreviations: *- statistically significant difference ($p < 0.05$) determined by Kruskal-Wallis test; D - dystrophy group (n=1); M - myopathy group (n=2); R - reference group (n=2).

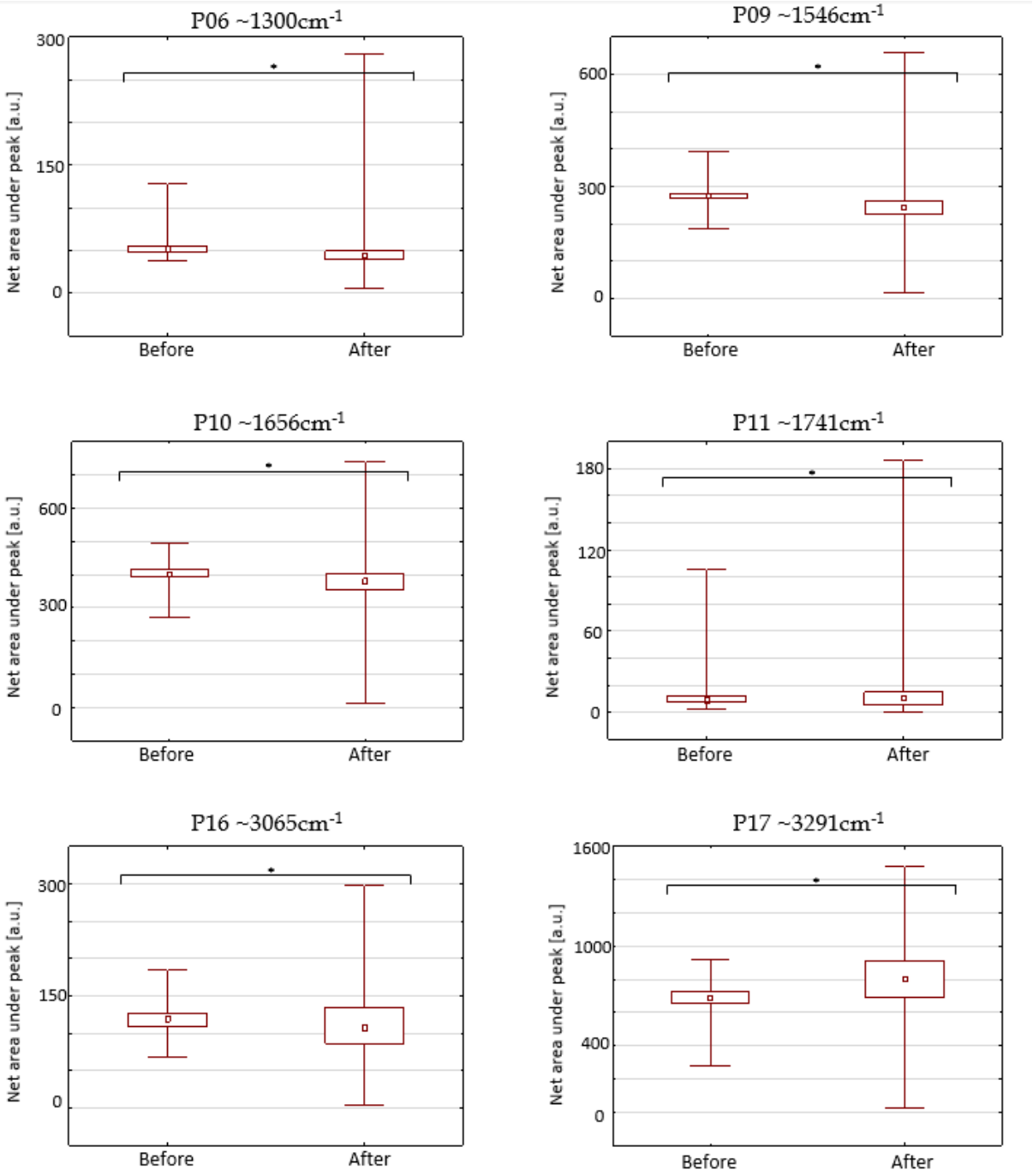

Figure 47. Comparison of the statistical significance of differences in the content of the analysed biomolecules in a comparative analysis of areas that may have been exposed to radiation damage (protein bands - P06, P09, P10, P16, P17 and ester band P11) in muscle tissues between the test groups (median, ±0.25-0.75% percentile and min-max values). Abbreviations: *- statistically significant difference ($p < 0.05$) determined by Kruskal-Wallis test; D - dystrophy group (n=1); M - myopathy group (n=2); R - reference group (n=2).

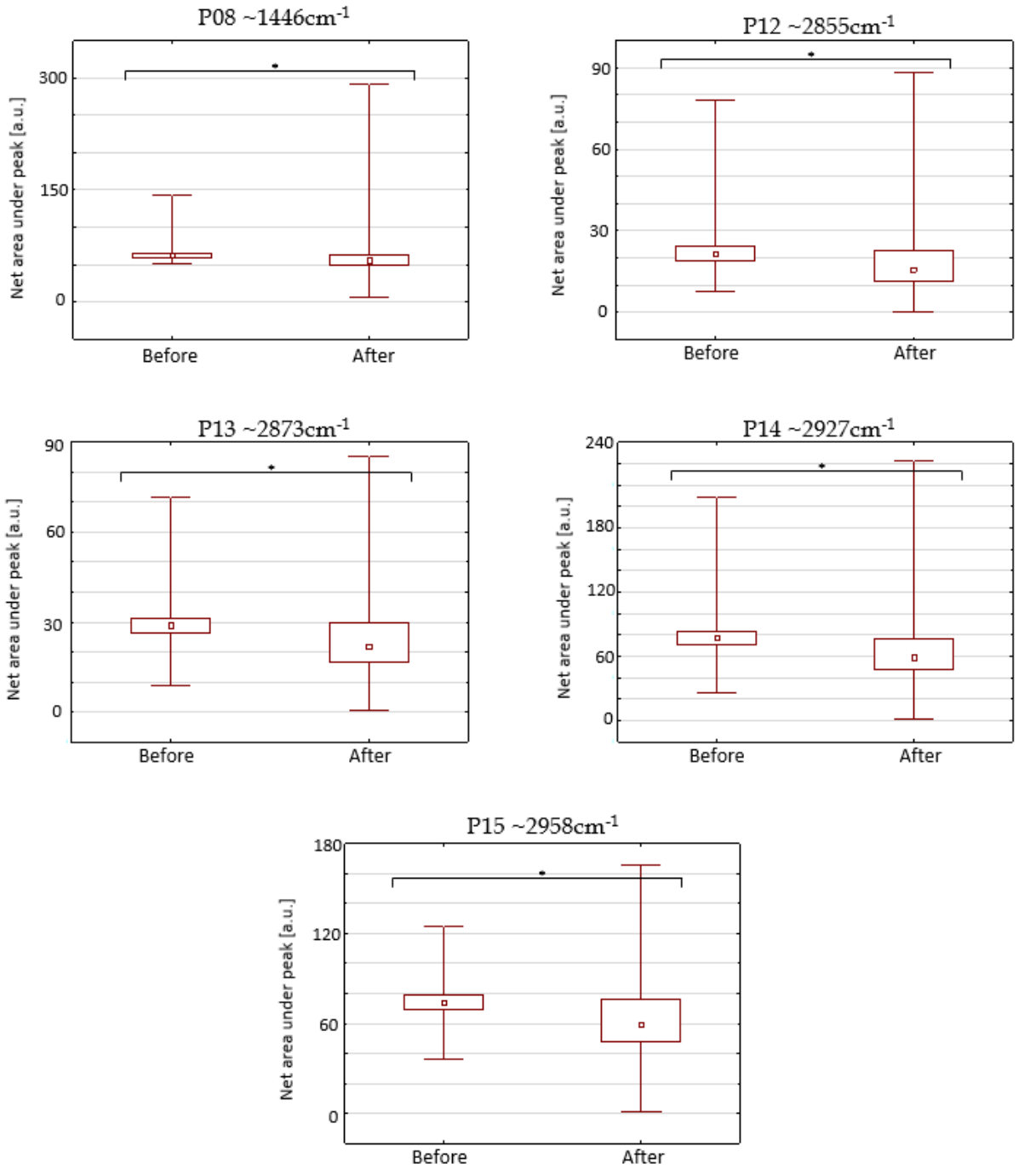

Figure 48. Comparison of the statistical significance of differences in the content of the analysed biomolecules in a comparative analysis of areas that may have been exposed to radiation damage (lipids bands - P08, P12, P13, P14, P15) in muscle tissues between the test groups (median, ±0.25-0.75% percentile and min-max values). Abbreviations: *- statistically significant difference ($p < 0.05$) determined by Kruskal-Wallis test; D - dystrophy group (n=1); M - myopathy group (n=2); R - reference group (n=2).

In order to check whether, despite possible radiation damage, samples are still differentiated into diagnosable groups, the MDA analysis was performed. Based on the obtained values of the partial Wilk's lambda presented in the Table 13, it was found that the factors P13 (~2973 cm^{-1}) – related to CH_3 symmetric stretching bond and P15 (~2958 cm^{-1}) - related to CH_3 asymmetric stretching bond, have the greatest influence on the separation. All 17 peaks participated in the creation of the model.

Table 13. Partial Wilks' lambda value for comparative analysis of bands from areas possibly affected by radiation damage with bands from areas prior to SR-XRF measurements.

Peak No.	**Wavenumber (cm^{-1})**	Partial Wilks' lambda
P01	~1043	0.998
P02	~1081	0.978
P03	~1114	0.676
P04	~1155	0.660
P05	~1237	0.780
P06	~1300	0.798
P07	~1388	0.824
P08	~1446	0.808
P09	~1546	0.934
P10	~1656	0.914
P11	~1741	0.897
P12	~2855	0.644
P13	~2873	0.282
P14	~2927	0.862
P15	~2958	0.508
P16	~3065	0.931
P17	~3291	0.671

The first two discriminant functions obtained are presented below, as they explain 92% of the discriminant power of the analysis performed.

$$D1 = 0.090\,P01 - 0.330\,P02 + 0.946\,P03 - 1.167\,P04 + 1.886\,P05 - 2.362\,P06 + 3.191\,P07 - 2.367\,P08 + 0.686\,P09 - 0.524\,P10 - 0.083\,P11 + 7.808\,P12 - 13.639\,P13 - 0.025\,P14 + 7.005\,P15 + 1.137\,P16 - 1.746\,P17 \quad (28)$$

$$D2 = 0.224\,P01 + 2.270\,P02 - 7.419\,P03 + 7.016\,P04 - 2.522\,P05 + 1.413\,P06 - 1.885\,P07 + 0.748\,P08 - 0.495\,P09 + 0.698\,P10 + 0.509\,P11 + 1.364\,P12 - 1.504\,P13 - 0.428\,P14 + 0.605\,P15 + 0.865\,P16 - 0.837\,P17 \quad (29)$$

These functions are shown in graphics in Figure 49.

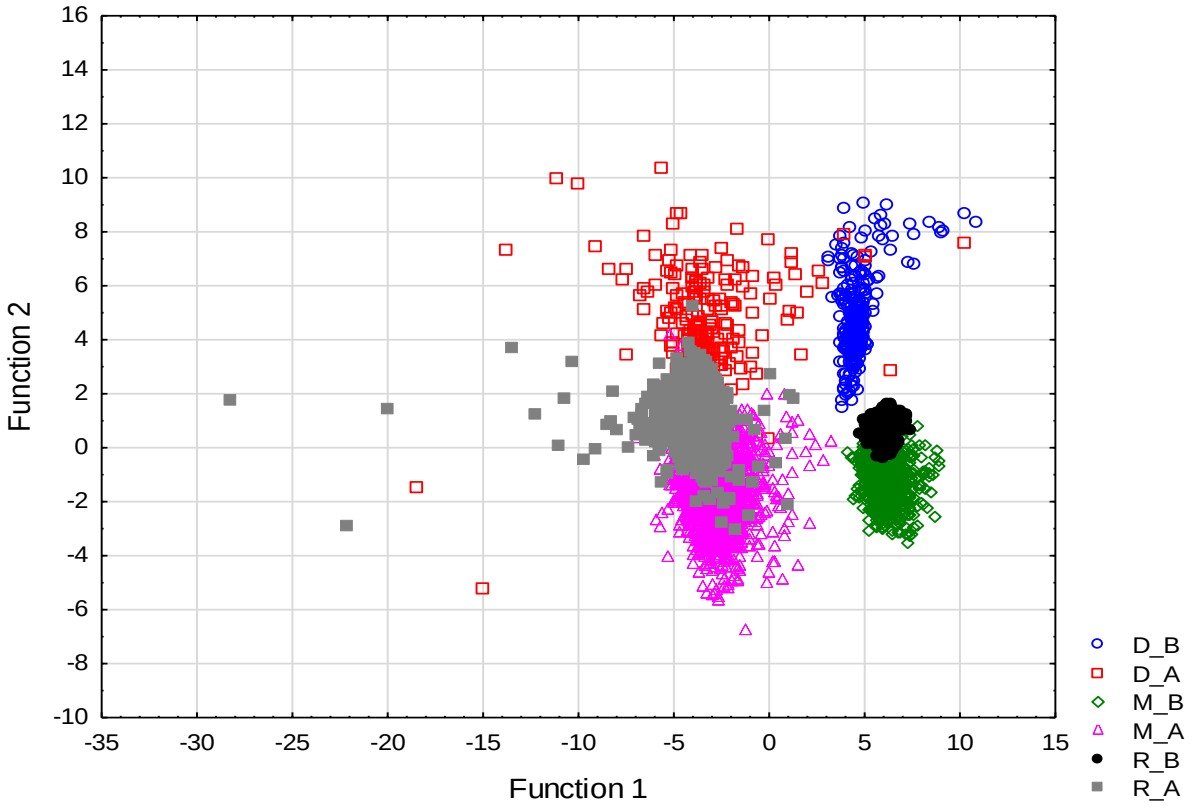

Figure 49. Graphical representation of configurations of discriminant function divided into groups represented by points in the discriminant variable system for comparative analysis of bands from areas possibly affected by radiation damage with bands from areas prior to SR-XRF measurements. Abbreviations: D_B - dystrophy group measured before the SR-XRF; D_A - dystrophy group measured after the SR-XRF; M_B - myopathy group measured before the SR-XRF; M_A - myopathy group measured after the SR-XRF; R_B - reference group measured before the SR-XRF; R_A - reference group measured after the SR-XRF.

To verify the correctness of the proposed model, a reverse analysis was performed to check the differences between the model and the diagnosis, and to assign the samples to the groups before and after measurements using the SR-XRF method. The model was found to be 96.5% correct - Table 14.

Table 14. Classification matrix for matching fibres using multivariate discriminant analysis for comparative analysis of bands from areas possibly affected by radiation damage with bands from areas prior to SR-XRF measurements. Abbreviations: D_B - dystrophy group measured before the SR-XRF; D_A - dystrophy group measured after the SR-XRF; M_B - myopathy group measured before the SR-XRF; M_A - myopathy group measured after the SR-XRF; R_B - reference group measured before the SR-XRF; R_A - reference group measured after the SR-XRF.

	Group	**%**	**Assignment**						**Total**
			D_B	D_A	M_B	M_A	R_B	R_A	
Diagnosis	D_B	95%	260	0	1	0	14	0	275
	D_A	89%	5	353	1	16	0	21	396
	M_B	97%	0	0	1571	0	44	0	1615
	M_A	95%	6	1	3	2893	1	133	3037
	R_B	99%	0	0	8	0	1182	0	1190
	R_A	97%	0	2	0	49	1	1950	2002
	Total	96.5%	271	356	1584	2958	1242	2104	8515

Slight differences in separating samples between groups before and after may be result from the size of the measured areas. The measurements were made with different models of spectrometers, with their different settings - the aperture for the before measurements was 150 x 150 μm^2, while for the after measurements was 20 x 20 μm^2. The measurements were carried out using Thermo Scientific Nicolet iN10 spectrometer for before group and using Thermo Scientific Nicolet 8700 for after group. Differences may also result from the severity of the development of pathological changes in the fibre, while the tissues assigned as the reference group were still suspected of pathological changes that may be present in them at an early stage of development.

7. Discussion

In the present study, five experiments were carried out: two using the X-ray Fluorescence method, in which elemental changes in the composition of muscle fibres and endomysium - the connective tissue surrounding the fibres - were studied, and three using the Infrared Spectrometry method, in which the objective of the study was to investigate differences in the biomolecular composition of muscle tissue diagnosed as a reference group and tissues classified as affected by pathological changes, as well as the possibility of differences between tissues measured before and after the XRF method.

Elemental studies

The use of the XRF method made it possible to analyse elements characteristic of biological samples such as Cl, P, K, S, Ca as well as trace elements Fe, Zn, Mn, Cu, Cr or Br. In each experiment, it was possible to distinguish three groups into which samples were classified on the basis of previous pathomorphological diagnosis: the Dystrophy group, the Myopathy group and the Reference group.

The results of the discriminant analysis obtained for fibres, showed that elements such as Ca, K, Cr and P have the greatest role in distinguishing between fibres diagnosed as a reference group and those classified as fibres affected by pathological changes. Calcium and phosphorus are elements of very versatile biological importance and one of the macro-elements. Both elements are involved in the construction of cell membranes. Calcium is involved in the conduction of neural impulses as well as in the mechanism of muscle contraction, while phosphorus is part of the structure of some proteins due to phosphate residues [48]. Changes in calcium ion content also send a signal to myoblasts for maintenance of their state, proliferation or differentiation into functional muscle cells [49]. Potassium plays an important role in the proper functioning of the muscular system, as well as an entire nervous system. Its deficiency leads, among other things, to muscle related ailments such as cramps and different form of paralysis. Chromium is part of the so-called glucose tolerance factor (GTF), which is responsible for normal glucose metabolism and sensitizes cells to insulin -

enhancing its action. Its deficiency, therefore, can lead to abnormal, insufficient nutrition of cells, including muscle cells.

For three of the aforementioned elements (Ca, Cr and P), a lower value for net area under the peak was observed for fibres diagnosed as affected by disease, based on the Kruskal-Wallis test in this research. What is interesting, for potassium, the value was higher for fibres assigned to the myopathy group. This may be due to the fact that dystrophies are typically conditions with more or less prolong course. In contrary in group of "myopathies" many of them are inflammatory nature which obviously take some more dynamic course.

For the other measured elements (S, Cl, Mn, Fe, Cu, Zn, Br), the value of the net area under the peak was higher than or equal to the reference group for fibres assigned to the myopathy group, and lower for dystrophies. Sulphur in cells is involved in the release of energy from proteins. It causes increased production of immunoglobins, thus participating in immune processes. Its deficiency impedes the absorption of some minerals [50]. Sulphur amino acids (methionine and cysteine) are involved in the synthesis of carnitine and creatine, as well as being precursors of coenzyme A. All of these substances are necessary for the production of ATP, which in the cell is, among other things, a source of energy [51]. Proper chloride levels in the body affect neuromuscular excitability. It is necessary for active protein transport and glucose metabolism. Excessive amounts of bromine in the body cause hyperpolarization of the neuronal membrane and abnormal conduction of impulses [52]. This element is also an essential cofactor during the sulfilimine formation reaction, a modification essential for tissue development found in collagen - the main component of intramuscular connective tissue [52]. Manganese is an element that activates enzymes involved in the production of energy and proteins involved in the regeneration of connective tissue. Manganese plays an important role in the metabolism of carbohydrates, proteins, lipids including cholesterol. Iron participates in the transport and storage of oxygen in tissues. It enters into the composition of haemoproteins including myoglobin, which is responsible for supplying oxygen to muscles for energy production [53]. As reported by Ikeda et al. [54] excess iron in muscle cells can lead to fibre atrophy, as it catalyses

the formation of highly toxic radicals in the Fenton reaction. Copper is the component of an enzyme (SOD Cu/Na) that protects cell membranes from free radicals. In addition, it participates in the formation of connective tissue [55]. Zinc maintains the stability and proper functioning of the cell membrane. It is also involved in skeletal muscle regeneration and synthesis. Zinc is involved in many metabolic pathways through its binding to proteins - ensuring their stability, and to enzymes - regulating their activity. By participating in metabolic and transcriptomic pathways, it prevents inflammation and oxidative stress. Zinc is also involved in regulating the initiation of autophagy - a system of protein degradation. It has been shown to play an important role in myogenesis - the process of formation and differentiation of muscle cells (myocytes) [56]. [57][58][59][60]

In the case of endomysium analysis, for all elements analysed, the value of net area under the peak was higher for fibres assigned to the reference group, relative to both groups into which fibres affected by disease changes were classified. Based on the results obtained for fiber analysis, there is no tendency to increase the content of the elements in the connective tissue for samples assigned to the groups of myopathies and dystrophies. This means that the elements whose net peak area value for dystrophy and myopathy is lower as compared to the reference group are actively metabolized and removed from the muscle tissue.

Biomolecular studies

The studies using infrared radiation tested whether the presence of particular bands or masses characteristic of biological samples affects the differentiation of tissues between those affected by pathological changes and those that served as reference. Discriminant analysis showed that bonds such as ~1043 cm^{-1} (nucleic acids, COH deformation bond), ~1388 cm^{-1} (lipids, COO symmetric stretching), ~2873 cm^{-1} (proteins, CH_3 symmetric stretching), ~3065 cm^{-1} (Amide B, N-H stretching) show the greatest influence on the differentiation of fibres between the diagnosed groups. On the other hand, the Kruskal-Wallis test showed that the largest differences in the value of the net area under the peaks, are present in the group of protein and fat bonds. Which can be tentatively explained by the presence of hypertrophic fibres in the tissues

affected by the lesions - a greater amount of proteins, the building material of the fibres, as well as the appearance of the fatty tissue in areas where muscle atrophy has occurred. However, no reduction or increase in the content of nucleic acids was observed in the samples affected by pathological changes - no reduction in the net area under the peak compared to the reference group for P01 (~1043 cm^{-1}), P02 (~1081 cm^{-1}) and P03 (~1114 cm^{-1}). This could reflect the process of "disappearance" of the sarcoplasm and its biomolecular constituents with relative preservation of nuclear material in pathology of muscle. Of note, the most severe level of muscle fibres atrophy takes form of a cluster of "naked" nuclei, as if devoid of sarcoplasm. No major difference was also observed for bands such as the ester bond (~1740 cm^{-1}) and Amide I (~1656 cm^{-1}).

For the biomolecular composition of the endomysium, a change in the value of the net area under the peak can be observed for the bands responsible for nucleic acids (~1043 cm^{-1}, ~1081 cm^{-1}, ~1114 cm^{-1} and ~1273 cm^{-1}). This may be due to the appearance of adipose tissue in the midst of connective tissue as a result of the disappearance of atrophic fibres - a noticeable "naked" nucleus effect. A significant increase in the net area under the peak was also observed for the ~1388 cm^{-1} band responsible for fatty acids - an increase in adipose tissue following fibre atrophy. No noticeable changes were observed for the CH_2 (~2855 cm^{-1} and ~2927 cm^{-1}) and CH_3 (~2873 cm^{-1} and ~2958 cm^{-1}) symmetrical and asymmetrical bands for the dystrophy group compared to the reference group, while a slight decrease was observed for the myopathy group compared to the two other groups. Slight changes were also observed for the bands responsible for proteins.

The last of the conducted experiments was to check whether XRF measurements affect the structure and biomolecular content of the samples, through the possible generation of radiation damage. For this purpose, the previously performed global measurements of muscle tissues made before XRF measurements were used, and subsequent FTIR measurements were made at exactly the same locations. Analysis of the received net values of area under the peak for individual bonds or their masses by U Mann-Whitney test - only two groups were compared: before and after XRF

measurements - showed no significant differences in the obtained values. However, for only one factor - P11 (1741 cm^{-1}), this analysis showed no statistically significant differences. Discriminant analysis showed that the bands ~2873 cm^{-1} and ~2958 cm^{-1} responsible for symmetric and asymmetric CH_3 binding, respectively, had the greatest effect on tissue differentiation. The energy used during the XRF experiment was quite high (~14 keV), high enough that only a small part of it could be deposited in the sample. All previously visible peaks and masses, were still clearly visible on the obtained measurement spectrum [61].

Elemental as well as molecular analysis showed differences in their composition between the fibres involved in the pathological changes and those classified as a reference group on the basis of medical diagnosis. Spectroscopy can be a very useful and valuable approach in the diagnosis of myopathic diseases, specifically for the detection of relatively small pathological changes. The use of spectroscopic methods can therefore be a complementary method to histopathological examination, especially in cases where the presence of pathological changes in muscle fibres cannot be visually discerned.

8. Conclusions

To reiterate the most important findings:

- Based on the elemental composition measurements carried out using the SR-XRF method, the following elements were found to be present: Cl, K, P, S, Ca, Fe, Zn, Mn, Cu, Cr and Br.

- The results of the discriminant analysis obtained for fibres, showed that elements such as P, K, Ca and Cr have the greatest role in distinguishing between fibres diagnosed as a reference group and those classified as fibres affected by pathological changes.

- For all elements analysed net area under the peak was lowest for the dystrophy group compared to the myopathy group and the reference group.

- For measurements of the elemental composition of endomysium using the SR-XRF method, it was possible to determine elements such as: Fe, Cu, Zn, Br and Rb.

- Since, the value of net area under the peak for all analysed elements for the dystrophy and myopathy groups is much lower compared to the reference group, this may indicate that these elements are metabolised and removed from the muscle tissue affected by the pathological processes.

- For measurements of the biomolecular composition using FTIR, it can be seen that the value of net area under the analysed peak was highest for the dystrophy group compared to the other two groups. A higher protein content can be observed in hypertrophic fibres, while atrophic fibres show a conversion of muscle tissue into fat tissue.

- Slight differences were observed in the changes in the net area under the peak for bands corresponding to nucleic acids. This may indicate that structures such as cell nuclei do not decompose during disease processes.

- For the study of the biomolecular composition of the endomysium, the largest changes in the net area under the peak were observed for the bands responsible for nucleic acids and the ~1388 cm^{-1} band responsible for fatty acids.

- A synchrotron radiation X-ray beam with an energy of ~14 keV does not significantly alter the biomolecular structure of the tissue.

This elemental and biomolecular analysis of muscle biopsy seems to have potential as a useful adjunct to the histopathological assessment.

9. References

[1] K. Spodaryk, *Patologia narządu ruchu*. Warszawa: Wydawnictwo Lekarskie PZWL, 2002.

[2] E. M. McNally and P. Pytel, "Muscle diseases: The muscular dystrophies," *Annu Rev Pathol*, vol. 2, pp. 87–109, 2007, doi: 10.1146/annurev.pathol.2.010506.091936.

[3] M. Tabebordbar, E. T. Wang, and A. J. Wagers, "Skeletal muscle degenerative diseases and strategies for therapeutic muscle repair," *Annual Review of Pathology: Mechanisms of Disease*, vol. 8, pp. 441–475, 2013, doi: 10.1146/annurev-pathol-011811-132450.

[4] I. Janssen, S. B. Heymsfield, Z. M. Wang, and R. Ross, "Skeletal muscle mass and distribution in 468 men and women aged 18-88 yr," *J Appl Physiol*, vol. 89, no. 1, pp. 81–88, 2000, doi: 10.1152/jappl.2000.89.1.81.

[5] P. M. Wróbel *et al.*, "Combined micro-XRF and TXRF methodology for quantitative elemental imaging of tissue samples," *Talanta*, vol. 162, pp. 654–659, 2017, doi: 10.1016/j.talanta.2016.10.043.

[6] G. R. Pereira, H. S. Rocha, C. Calza, M. J. Anjos, C. A. Pérez, and R. T. Lopes, "Biological tissues analysis by XRF microtomography," *Applied Radiation and Isotopes*, vol. 68, no. 4–5, pp. 704–708, 2010, doi: 10.1016/j.apradiso.2009.12.015.

[7] J. Dudala *et al.*, "Biomolecular characterization of adrenal gland tumors by means of SR-FTIR," *Analyst*, vol. 140, no. 7, pp. 2101–2106, 2015, doi: 10.1039/c4an01891e.

[8] G. Monnier, E. Frahm, B. Luo, and K. Missal, "Developing FTIR Microspectroscopy for the Analysis of Animal-Tissue Residues on Stone Tools," *J Archaeol Method Theory*, vol. 25, no. 1, pp. 1–44, 2018, doi: 10.1007/s10816-017-9325-3.

[9] O. Bozkurt, M. Severcan, and F. Severcan, "Diabetes induces compositional, structural and functional alterations on rat skeletal soleus muscle revealed by FTIR spectroscopy: A comparative study with EDL muscle," *Analyst*, vol. 135, no. 12, pp. 3110–3119, 2010, doi: 10.1039/c0an00542h.

[10] A. Kohler, D. Bertrand, H. Martens, K. Hannesson, C. Kirschner, and R. Ofstad, "Multivariate image analysis of a set of FTIR microspectroscopy images of aged bovine muscle tissue combining image and design information," *Anal Bioanal Chem*, vol. 389, no. 4, pp. 1143–1153, 2007, doi: 10.1007/s00216-007-1414-9.

[11] D. P. Jerônimo *et al.*, "Detection of creatine in rat muscle by FTIR spectroscopy," *Ann Biomed Eng*, vol. 40, no. 9, pp. 2069–2077, 2012, doi: 10.1007/s10439-012-0549-9.

[12] N. Simsek Ozek, I. B. Bal, Y. Sara, R. Onur, and F. Severcan, "Structural and functional characterization of simvastatin-induced myotoxicity in different skeletal muscles," *Biochim Biophys Acta Gen Subj*, vol. 1840, no. 1, pp. 406–415, 2014, doi: 10.1016/j.bbagen.2013.09.010.

[13] T. T. Yang *et al.*, "Histopathology mapping of biochemical changes in myocardial infarction by Fourier transform infrared spectral imaging," vol. 207, pp. 34–39, 2011, doi: 10.1016/j.forsciint.2010.12.005.

[14] W. R. Frontera and J. Ochala, "Skeletal Muscle: A Brief Review of Structure and Function," *Behav Genet*, vol. 45, no. 2, pp. 183–195, 2015, doi: 10.1007/s00223-014-9915-y.

[15] F. M. Trovato, R. Imbesi, N. Conway, and P. Castrogiovanni, "Morphological and functional aspects of human skeletal muscle," *J Funct Morphol Kinesiol*, vol. 1, no. 3, pp. 289–302, 2016, doi: 10.3390/jfmk1030289.

[16] T. Chichocki, J. A. Litwin, and J. Mirecka, *Kompendium Histologii. Podręcznik dla studentów nauk medycznych i przyrodniczych.* Wydawnistwo Uniwersytetu Jagiellońskiego, 2016.

[17] J. Stachura and W. Domagała, *Patologia znaczy słowo o chorobie. Tom II.* Kraków: Polska Akademia Umiejętności. Wydział Lekarski, 2009.

[18] R. E. van Grieken and A. A. Markowicz, *Handbook of X-Ray Spectrometry: Methods and Techniques*, no. 1. New York: Marcel Dekker, Inc., 2002. doi: 10.1002/xrs.1300230110.

[19] O. Klein and Y. Nishina, "Über die Streuung von Strahlung durch freie Elektronen nach der neuen relativistischen Quantendynamik von Dirac," *Zeitschrift für Physik*, vol. 52, p. 853868, 1929.

[20] B. Dziunikowski, *Zastosowanie izotopów promieniotwórczych cz.I*. Kraków: Wydawnictwo AGH, 1995.

[21] M. Szczerbowska-Boruchowska, "Sample thickness considerations for quantitative X-ray fluorescence analysis of the soft and skeletal tissues of the human body - theoretical evaluation and experimental validation," *X-Ray Spectrometry*, vol. 41, no. 5, pp. 328–337, 2012, doi: 10.1002/xrs.2407.

[22] A. D. Surówka, "Development of analytical approaches for molecular and fully quantitative elemental micro-imaging of brain tissue with X-ray and infrared radiation," *Doctoral thesis*, 2016.

[23] B. Beckhoff, B. Kanngießer, N. Langhoff, R. Wedell, and H. Wolff, *Handbook of practical X-ray Fluorescence Analysis*. Berlin: Springer, 2006.

[24] B. Stuart, *Infrared Spectroscopy: Fundamentals and Applications*. John Wiley & Sons Ltd, 2004.

[25] B. C. Smith, *Fundamentals of Fourier Transform Infrared Sepctroscopy*. CRC Press, 2011.

[26] A. Hrynkiewicz and E. Rokita, *Fizyczne metody badań w biologii, medycynie i ochronie środowiska*. Warszawa: Wydawnictwo Naukowe PWN, 2013.

[27] P. J. Larkin, *IR and Raman Spectroscopy: Principles and Spectral Interpretation*. Elsevier, 2011.

[28] K. Malek, Ed., *Vibrational Spectroscopy: From theory to practice*. Kraków: Wydawnictwo Naukowe PWN, 2016.

[29] Z. Kęcki, *Podstawy spektroskopii molekularnej*. Warszawa: Wydawnictwo Naukowe PWN, 2013.

[30] M. B. Editor, *Optical Spectroscopy and Computational Methods in Biology and Medicine*. Krakow, 2014.

[31] A. D. Surowka, P. Wrobel, M. M. Marzec, D. Adamek, and M. Szczerbowska-Boruchowska, "Novel approaches for correction against the soft matrix effects in the quantitative elemental imaging of human substantia nigra tissue using synchrotron X-ray fluorescence," *Spectrochim Acta Part B At Spectrosc*, vol. 123, pp. 47–58, Sep. 2016, doi: 10.1016/j.sab.2016.07.014.

[32] J. F. W. Mosselmans *et al.*, "I18 - The microfocus spectroscopy beamline at the Diamond Light Source," *J Synchrotron Radiat*, vol. 16, no. 6, pp. 818–824, 2009, doi: 10.1107/S0909049509032282.

[33] C. G. Schroer *et al.*, "Hard x-ray nanoprobe of beamline P06 at PETRA III," *AIP Conf Proc*, vol. 1741, no. July 2016, 2016, doi: 10.1063/1.4952830.

[34] V. A. Solé, E. Papillon, M. Cotte, P. Walter, and J. Susini, "A multiplatform code for the analysis of energy-dispersive X-ray fluorescence spectra," *Spectrochim Acta Part B At Spectrosc*, vol. 62, no. 1, pp. 63–68, 2007, doi: 10.1016/j.sab.2006.12.002.

[35] J. Yousefi, "Image binarization using otsu thresholding algorithm," *Ontario, Canada: University of Guelph*, no. May, 2011.

[36] A. D. Surowka, P. Wrobel, D. Adamek, E. Radwanska, and M. Szczerbowska-Boruchowska, "Synchrotron radiation based X-ray fluorescence shows changes in the elemental composition of the human substantia nigra in aged brains," *Metallomics*, vol. 7, no. 11, pp. 1522–1531, 2015, doi: 10.1039/c5mt00154d.

[37] A. Stanisz, *Przystępny kurs statystyki z zastosowaniem STATISTICA PL na przykładach z medycyny. Tom 1. Statystyki podstawowe.* Kraków: StatSoft Polska Sp. z o.o., 2006.

[38] A. Stanisz, *Przystępny kurs statystyki z zastosowaniem STATISTICA PL na przykładach z medycyny. Tom 3. Analizy wielowymiarowe.* Kraków: StatSoft Polska Sp. z o.o., 2007.

[39] M. Toplak, S. T. Read, C. Sandt, and F. Borondics, "Quasar: Easy machine learning for biospectroscopy," *Cells*, vol. 10, no. 9, Sep. 2021, doi: 10.3390/cells10092300.

[40] M. Toplak *et al.*, "Infrared Orange: Connecting Hyperspectral Data with Machine Learning," *Synchrotron Radiat News*, vol. 30, no. 4, pp. 40–45, Jul. 2017, doi: 10.1080/08940886.2017.1338424.

[41] G. Cinque, M. D. Frogley, K. Wehbe, T. N. Q. Nguyen, A. Fitzpatrick, and C. S. Kelley, "Synchrotron-Based Infrared Spectral Imaging at the MIRIAM Beamline of Diamond Light Source," *Synchrotron Radiat News*, vol. 30, no. 4, pp. 11–16, 2017, doi: 10.1080/08940886.2017.1338416.

[42] A. C. S. Talari, M. A. G. Martinez, Z. Movasaghi, S. Rehman, and I. U. Rehman, "Advances in Fourier transform infrared (FTIR) spectroscopy of biological tissues," *Appl Spectrosc Rev*, vol. 52, no. 5, pp. 456–506, 2017, doi: 10.1080/05704928.2016.1230863.

[43] D. P. Jerônimo *et al.*, "Detection of creatine in rat muscle by FTIR spectroscopy," *Ann Biomed Eng*, vol. 40, no. 9, pp. 2069–2077, 2012, doi: 10.1007/s10439-012-0549-9.

[44] M. F. Triola, *Elementary Statistics*, Tenth. Pearson Education, Inc., 2006.

[45] S. Ostasiewicz, Z. Rusnak, and U. Siedlecka, *Statystyka. Elementy teorii i zadania.* Wrocław: Wydawnictwo Akademii Ekonomicznej im. Oskara Langego we Wrocławiu, 2003.

[46] R. Lyman Ott and M. Longnecker, "An Introduction to Statistical Methods & Data Analysis," 2016.

[47] T. Górecki, *Podstawy statystyki z przykładami w R*. Legionowo: Wydawnictwo BTC, 2011.

[48] W. Grünberg *et al.*, "Phosphorus content of muscle tissue and muscle function in dairy cows fed a phosphorus-deficient diet during the transition period," pp. 4072–4093, 2019, doi: 10.3168/jds.2018-15727.

[49] M. K. Tu, J. B. Levin, A. M. Hamilton, and L. N. Borodinsky, "Calcium signaling in skeletal muscle development, maintenance and regeneration," *Cell Calcium*, vol. 59, no. 2–3. Churchill Livingstone, pp. 91–97, Mar. 01, 2016. doi: 10.1016/j.ceca.2016.02.005.

[50] S. Hewlings and D. Kalman, "Sulfur and Human Health," no. September, pp. 5–12, 2019.

[51] I. Papet *et al.*, "Sulfur amino acids and skeletal muscle," in *Nutrition and Skeletal Muscle*, Elsevier, 2018, pp. 335–363. doi: 10.1016/B978-0-12-810422-4.00020-8.

[52] A. S. Mccall, C. F. Cummings, G. Bhave, R. Vanacore, and A. Page-mccaw, "Bromine Is an Essential Trace Element for Assembly of Collagen IV Scaffolds in Tissue Development and Architecture," *Cell*, vol. 157, no. 6, pp. 1380–1392, 2014, doi: 10.1016/j.cell.2014.05.009.

[53] M. Halon-golabek, A. Borkowska, A. Herman-antosiewicz, and L. J. Martin, "Iron Metabolism of the Skeletal Muscle and Neurodegeneration," vol. 13, no. March, pp. 1–15, 2019, doi: 10.3389/fnins.2019.00165.

[54] Y. Ikeda *et al.*, "Iron-induced skeletal muscle atrophy involves an Akt-forkhead box O3-E3 ubiquitin ligase-dependent pathway," *Journal of Trace Elements in Medicine and Biology*, vol. 35, pp. 66–76, 2016, doi: 10.1016/j.jtemb.2016.01.011.

[55] D. J. Waggoner, T. B. Bartnikas, and J. D. Gitlin, "The Role of Copper in Neurodegenerative Disease," *Neurobiology Disease*, vol. 6, pp. 221–230, 1999, doi: 10.1007/s12035-022-02847-x.

[56] J. D. Hernández-Camacho, C. Vicente-García, D. S. Parsons, and I. Navas-Enamorado, "Zinc at the crossroads of exercise and proteostasis," *Redox Biology*, vol. 35. Elsevier B.V., Aug. 01, 2020. doi: 10.1016/j.redox.2020.101529.

[57] W. Opoka, B. Muszyńska, A. Rutkowska, M. Schlegel-Zawadzka, and M. Płonka, *Właściwości fizykochemiczne i biologiczne wybranych pierwiastków*. 2015.

[58] M. A. Zoroddu, J. Aaseth, G. Crisponi, S. Medici, M. Peana, and V. M. Nurchi, "The essential metals for humans: a brief overview," *J Inorg Biochem*, vol. 195, no. November 2018, pp. 120–129, 2019, doi: 10.1016/j.jinorgbio.2019.03.013.

[59] N. N. Greenwood and A. Earnshaw, "Chemistry of the Elements Second Edition," p. 1635, 1997.

[60] W. Mertz, "The essential trace elements," *Science (1979)*, vol. 213, no. 4514, pp. 1332–1338, 1981, doi: 10.1126/science.7022654.

[61] A. D. Surowka *et al.*, "Soft X-ray induced radiation damage in thin freezedried brain samples studied by FTIR microscopy," *J Synchrotron Radiat*, vol. 27, pp. 1218–1226, 2020, doi: 10.1107/S1600577520010103.

10. Index of Figures and Tables